

INVESTIGATION ON WAVEFRONT SENSING FOR PROPAGATION CHARACTERISTICS OF TURBULENCE IMPACTED LIGHT BEAMS

A Thesis submitted

In partial fulfillment for the Degree of

Doctor of Philosophy

by

PRAMOD PANCHAL



**DEPARTMENT OF PHYSICS
INDIAN INSTITUTE OF SPACE SCIENCE AND
TECHNOLOGY
Thiruvananthapuram
SEPTEMBER, 2021**

CERTIFICATE

This is to certify that the thesis entitled **Investigation on wavefront sensing for propagation characteristics of turbulence impacted light beams** submitted by **Pramod Panchal** to the Indian Institute of Space Science and Technology, Thiruvananthapuram, in partial fulfillment for the award of the degree of **Doctor of Philosophy** is a *bona fide* record of research work carried out by him under my/our supervision. The contents of this thesis, in full or in parts, have not been submitted to any other Institution or University for the award of any degree or diploma.

Prof. C. S. Narayanamurthy

Supervisor

Department of Physics

Thiruvananthapuram

September,
2021

Signature of HOD with seal

DECLARATION

I declare that this thesis entitled **Investigation on wavefront sensing for propagation characteristics of turbulence impacted light beams** submitted in partial fulfillment of the degree of **Doctor of Philosophy** is a record of original work carried out by me under the supervision of **Prof. C. S. Narayanamurthy**, and has not formed the basis for the award of any other degree or diploma, in this or any other Institution or University. In keeping with the ethical practice in reporting scientific information, due acknowledgements have been made wherever the findings of others have been cited.

PRAMOD PANCHAL
(SC15D026)

Thiruvananthapuram-695547

September, 2021

ACKNOWLEDGMENTS

I would like to take this opportunity to thank IIST for giving me facilities to grow and bloom as a research scholar. I express my heartfelt gratitude to my supervisor Prof. C. S. Narayanamurthy whose invaluable guidance and mentoring provided me the zest for the research.

I extend my sincere thanks to Dr. D. N. Naik for his valuable suggestions, encouragement and support. The discussion with him on fine details of experiments, outreach activities or correlating research with life helped me a lot to stand through tough times.

Sincere thanks to my doctoral committee members, Prof. Joby Joseph, Prof. S Muruges, Prof. Deepak Mishra and Prof. Rakesh Kumar Singh for timely evaluating my research progress and providing valuable feedback.

I feel immense pleasure to thank my friends Preetam, Darshika, Surya, Yogesh, Shashank, Praveen and Shalabh for their wonderful company, delights and incredible moral support during the entire course of this work. You guys were very quick and blatant to give me valuable inputs to enhance my research.

My want to appreciate my colleagues Dr. Vinu R. V., Ms. Athira T. S and Mrs. Lekshmi S. R. for support and keeping healthy work environment in the laboratory. I would like to thank Mrs. Sahela and Mrs. Rekshma for involving experiments. I thank to Lab staff Mrs. Remya Pradeep, Mrs. Surasreelekshmi, Mrs. Laksmi Devan for support and help in getting required components for experiments.

I feel ecstatic to have my partner Laxmi who constantly supported and motivated me. Whenever I had grinded time and going down she was there like a pillar to upkeep and encourage me. I want to thank my childhood friends Sunil, Pankaj, Mayank, Deepak, Herdev and Bhavna who were there to support me morally throughout this journey.

I owe this thesis to my parents and family members for their constant moral support, affection, love and blessings from the very first day of my journey of life.

ABSTRACT

The effects of atmospheric turbulence on light beams and the turbulence induced higher order aberrations plays an important role for free space optical communication. In this thesis, the immunity of higher order Gaussian beams in maintaining its integrity during its propagation through atmospheric turbulence is experimentally investigated. The propagation analysis of laser Gaussian beam passing twice through a dynamic atmospheric turbulent mimicking Pseudo Random Phase Plate (PRPP) is carried out using variance matrix method. The characteristics like twist, symplectic Eigen values, asymmetry parameters, scintillation and beam wander are calculated for Gaussian and standard Laguerre Gaussian beams through rotating PRPP.

Further wavefront detection using a common path vectorial shearing interferometer based wavefront sensor has been carried out. Copies of input shearing beam is obtained using cascaded sagnac interferometer. The proof of principle of Vectorial shearing interferometer based wavefront sensor is carried out. Wavefront variation introduced due to change in position of collimating lens has been calculated and verified with simulated results. A comparative study on SHWFS and Vectorial interferometric wavefront sensor has been done.

For simulating the wavefront sensing using a natural light source or an artificially induced guide star, the proposed interferometer based wavefront sensor is tested with low coherent light source with finite spatial extent. The designs for maintaining the interference within temporal coherence domain and reviving the spatial coherence using diffraction effects ensured the sensing of wavefront. Wavefront of turbulent impacted (PRPP) low coherent wave has been detected using vectorial shearing interferometer based wavefront sensor.

TABLE OF CONTENTS

CERTIFICATE

DECLARATION

ACKNOWLEDGEMENTS

ABSTRACT

LIST OF FIGURES

LIST OF TABLES

ABBREVIATIONS

NOTATIONS

1. Introduction	1
1.1 Atmospheric Turbulence	1
1.2 Wavefront sensors	2
1.2.1 Shack-Hartmann Sensor	4
1.2.1 Interferometric Wavefront Sensor	5
1.3 Analysis of wavefront from phase gradients	6
1.3.1 Variance matrix	6
1.3.1 Zernike polynomials.....	7
1.4 Minimizing the effect of turbulence	8
1.4.1 Higher order Gaussian beams as light source	8
1.4.1 Adaptive optics	11
1.5 Scope of the thesis	12
1.6 Thesis Outline	12
 2. Propagation analysis of double passage Gaussian and single passage topologically charged vortex laser beam using variance matrix	 14
2.1 Introduction.....	14
2.2 Beam propagation characterization using Variance matrix	15
2.2.1 Variance Matrix	19
2.2.2 Characteristics of Variance matrix	26

2.3 Computation of Physically Significant Parameters from Variance matrix	28
2.3.1 Symplectic Eigen values	28
2.3.2 Twist Parameter	30
2.3.3 Aymmetry Parameter	30
2.4 Experimental results and discussion	31
2.4.1 Twist Parameter	34
2.4.2 Symplectic Eigen values	36
2.4.3 Aymmetry Parameter	39
2.5 Observation.....	41
 3. Insensitiveness of higher order topologically charged LG beams to dynamic turbulence impact	43
3.1 Introduction.....	43
3.2 Experimental procedure and theory	44
3.2.1 Propagation characteristics of LG beams through a dynamic turbulence...	44
3.2.2 Scintillations due to dynamic turbulent impact	44
3.2.3 Beam wandering due to dynamic turbulent impact along x and y directions	48
3.2.4 Intensity and Zernike polynomials measurements for turbulent impacted Laser Gaussian and topologically charged beams	52
3.3 Observation.....	57
 4. Vectorial shearing cascaded Sagnac interferometric wavefront sensor	59
4.1 Introduction	59
4.2 Principle of Vectorial Shearing wavefront sensor	60
4.3 Experimental Procedure	64
4.4 Results and Analysis	66
4.5 Summary	73

5. Vectorial shearing cascaded Sagnac interferometric wavefront sensor	74
5.1 Introduction	74
5.2 Experimental comparison of VSI and SHWFS	76
5.2.1 Measurement of curvature	77
5.2.2 Measurement of turbulence affected wavefront	80
5.3 Merits of cascaded Sagnac vectorial shearing interferometer	82
5.4 Limitation of cascaded Sagnac VSI	84
5.5 Summary	84
6. Wavefront sensing using low-coherent sources through spatial coherence revival	85
6.1 Introduction	85
6.2 Principle behind low coherence wavefront sensing	87
6.3 Experimental Results and discussion	95
6.3.1 Validation of the scheme sensing quadratic wavefronts	95
6.3.2 Sensing of wavefront distortion by atmospheric turbulence simulator	100
6.4 Discussion	101
6.5 Summary	102
Conclusion and Future scope	104
REFERENCES	107
Appendix A Pseudo Random Phase Plate	116
Appendix B Shack-Hartmann Wavefront Sensor	119
Appendix C Derivation of copies generated by VSI	122
Appendix D Derivation of copies generated by grating	127
List of Publications	131

LIST OF FIGURES

1.1 Amplitude and phase distribution of LG ₀₁ beam	11
2.1 The experimental set-up for double pass laser Gaussian beam	31
2.2 The conceptual arrangement of experimental geometry	32
2.3 The experimental set-up for single pass laser vortex beam	32
2.4 (a) Vortex geometry of phase plate	33
2.4 (b) Charge map of phase plate manufactured by RPC Photonics	33
2.5 Twist values for different beams and double passage Gaussian beams	35
2.6 The plot of κ_1 and κ_2 for different beams and double passage Gaussian beam	38
2.7 The plot of V_{as} for different charge beams and double passage Gaussian beam	40
3.1 Experimental set-up	44
3.2 Scintillation index for Gaussian and topologically charged beams at different distance	47
3.3 (a) one micro lens of lens let array	49
3.3 (b) Spot diagram for plane reference beam	49
3.3 (c) Spot diagram for aberrated beam.....	49
3.4 (a) Beam wander in x-direction.....	51
3.4 (b) Beam wander in y-direction	51
3.5 Amplitude and phase distribution of LG01 beam	52
3.6 Experimental set-up for SLM generated LG beam passing through PRPP .	53
3.7 The recorded intensities and Zernike coefficients for different Gaussian charged beam	54
3.8 The recorded intensities and Zernike coefficients for different LG beams. .	57
4.1 Conceptual diagrams for common-path Vectorial shearing wavefront sensor	61
4.2 Generation of four copies of the wavefront using two Sagnac interferometers kept in series	65
4.3 Wavefront sensing using Vectorial shearing interferometer.	66
4.4 (a) Vectorial sheared fringe pattern.....	67
4.4 (b) Fourier transform of fringe pattern	67

4.5 (a) Gradient along X-direction	68
4.5 (b) Gradient along Y-direction	68
4.5 (c) Reconstructed Wavefront	68
4.6 The horizontal line profile ($y=0$) of reconstructed wavefront at different positions of collimating lens along z-direction with step size of 0.5mm.	70
4.7 The wavefront deviations when collimating lens moves in forward and backward direction.	72
5.1 Shift in centroid from lens of SHWFS	74
5.2 (a) Lateral shearing beams and (b) radially shearing beams	75
5.3 Three beam shearing along x and y directions	75
5.4 Experimental set-up for wavefront sensing using SHWFS and cascaded sagnac VSI	76
5.5 (a) Intensity recorded using SHWFS, (b) Gradient along x-direction, and (c) Gradient along y-direction.....	78
5.6 (a) Recorded interferogram using VSI, (b) gradient along x direction and (c) gradient along y direction	79
5.7 reconstructed wavefront for SHWFS data at different position of collimating lens L.	79
5.8 reconstructed wavefront for cascaded sagnac data at different position of collimating lens L.....	80
5.9 Image on sensor of SHWFS with plane wave (Without PRPP) as input, (b) image on sensor of SHWFS after inserting PRPP.....	81
5.10 The reconstructed wavefront results for SHWFS data after inserting PRPP.	81
5.11 The reconstructed wavefront results for cascaded Sagnac VSI data after inserting PRPP.....	82
5.12 When different modes are input to a lens.....	84
6.1 Conceptual diagram for common-path VSI	88
6.2 (a) Spectra of LED source	91
6.2 (b) Residual of intensity plot after curve fitting of LED spectra.....	91
6.2 (c) Fall of contrast for the spatial carrier fringes along y direction as explained by equation 6.14	91
6.2 (d)The intensity variation along the y direction after normalizing with the intensity distribution of the interfering beams.	91
6.3 The diffraction effect in spatial coherence function, introduced by hard aperture, measured at the interferogram plane	94

6.4 Wavefront sensing using vectorial shearing interferometer	95
6.5 (a) Interferogram	97
6.5 (b) Fourier transform of fringe pattern	97
6.5 (c) Wrapped phase gradient along y-direction	97
6.5 (d) Wrapped phase gradient along x-direction.	97
6.6 (a) Unwrapped phase gradient along x-direction	98
6.6 (b) Unwrapped phase gradient along y-direction	98
6.6 (c) Reconstructed phase	98
6.7 Recorded interferogram, line profile and 3D plot of reconstructed phase at different position of collimation lens.	99
6.8 Wavefront sensing of aberrated wavefront by PRPP using vectorial shearing interferometer.	100
6.9 Interferograms at different position of PRPP and corresponding reconstructed Wavefronts	101
A.1 Diagram of static Pseudo random phase plate	116
A.2 Diagram of Near-Index-Match concept	117
B.1 Plane wavefront incident on lenslet array and its spot diagram (b) Aberrated wavefront incident to micro lenslet array and its spot diagram.....	119
B.2 Centroid shift for Single Lens	120
C.1 Conceptual diagram for common-path VSI	122
D.1 Conceptual diagram for Grating based wavefront sensor	127

LIST OF TABLES

4.1 PV and RMS values of calculated wavefront at different position of collimating lens L	72
---	----

ABBREVIATIONS

SHWFS	Shack-Hartmann Wavefront Sensor
LG	Laguerre Gaussian
PRPP	Pseudo Random Phase Plate
CCD	Charge Coupled Device
SLM	Spatial Light Modulator
He-Ne	Helium Neon
L	Lens
M	Mirror
SF	Spatial Filter
LED	Light Emitting Diode
PV	Peak to Valley
RMS	Root Mean Square
BS	Beam Splitter

NOTATIONS

r_0	Fried's Coherence Length
ϕ	Phase
S_p	Symplectic Group
V	Variance Matrix
τ	Twist Parameter
κ	Symplectic Eigen Value
V_δ	Difference between two Variance Matrices
V_{as}	Asymmetry parameter
f	Focal Length
λ	Wavelength
ν	Frequency

Chapter 1

Introduction

1.1 Atmospheric Turbulence

In general, the earth's atmosphere is considered to be locally homogeneous medium. However, its properties change considerably due to temperature, humidity, pressure, wind velocities, etc. [1-3]. The atmospheric turbulence is caused due to naturally occurring variations in temperature (less than 1°) causing small changes in atmospheric density which ultimately results in changes in refractive index. The magnitude of atmospheric refractive index fluctuations depends on the air density and temperature variations and in true sense, the optical effects of turbulence decrease with increase in altitude. Though this change in refractive index is of the order of 10^{-6} it can accumulate and cause cumulative effect in the index profile of the atmosphere resulting in random fluctuations of phase of a beam passing through it. The atmospheric turbulence can be classified into Kolmogorov type and non-Kolmogorov type turbulent medium and Kolmogorov, in his theory, proposed that the structure of atmosphere is homogenous and isotropic for large Reynolds numbers with the inertial sub-range defined by the eddy size bounded by the inner scale l_0 and the outer scale L_0 respectively. This (Kolmogorov) model assumes that the atmosphere is comprised of small eddies that interact and exchange energy [2].

There are many ways in which one can tap the possibilities brought forth by such a mundane thing like turbulence. Researchers have recently demonstrated the possibility of using the random phase acquired by a light field on propagation through atmospheric turbulence for cryptographic purposes [4-6]. Using phase fluctuations of a light field that has propagated through a turbulent atmosphere the random-key generation was demonstrated [4]. It was shown that the phase acquired by a light field

on propagation through atmospheric turbulence like conditions can be used by two remote observers to distil a shared random key [5-6].

Wavefront of a light beam is defined as deviation of its phase from a reference sphere [1]. It changes while propagating through atmospheric turbulence. In an actual sense, the wavefront of a propagating light beam is the two-dimensional map of its phase at the aperture or a plane normal to the propagation. Due to the changes in refractive index profile of the atmosphere, the light beam passing through experiences wandering, scintillation effect and spreading. This can compromise the information carrying capacity of photons in free space optical communication.

The atmospheric turbulence induced phase fluctuations affects the image quality of distant objects in deep space whenever viewed from ground based telescopes [1]. In general, atmospheric turbulence can impact lower order aberrations like piston (uniform shift in wavefront), tilt of wavefront, defocus, astigmatism and higher order aberrations like coma, spherical aberration and trefoil [1, 3]. Apart from piston which is a uniform shift in wavefront, tilt and focus normally affect the image quality or propagation of a wavefront. The cumulative effects of these lower order aberrations can cause high spatial frequency beam spreading, low spatial frequency beam wandering, and intensity variations(also known as scintillation) resulting in blurring or twinkling of stars[7-8]. The beam wandering is produced by the turbulent eddies in atmosphere with the sizes of the order of $(\lambda L)^{1/2}$ where L is the propagation length.

1.2 Wavefront sensors

A wavefront is an important parameter in the propagation of light and can be used to characterize optical surfaces, align optical assemblies or help to improve the performance of optical systems. Wavefront sensor is a device which measures the optical wavefront (phase) and its aberration [1]. Phase is important information in optical testing, optical communication and adaptive optics systems to do required phase correction.

Phase detection can be done by transporting phase information in intensity using diffraction, refraction or interference [9-12]. The format of the information often drives the ability to use it in an optimal manner. Two basic types of wavefront information are used i.e. zonal and modal. When the wavefront is expressed in terms of the optical path difference over a small spatial area, the wavefront sensing is said to be zonal. When wavefront is expressed in terms of coefficients of the modes of a polynomial expressed over entire pupil then the wavefront is said to be modal [1].

It is possible to reconstruct the wavefront of the entire field from the measurements of tilt in smaller regions. Wavefront division using various techniques like sub-apertures division and the Hartmann test is most common [9-10]. By fitting a continuous curve to local tilted planes, a two-dimensional surface is generated [13]. This information is necessary for the correction of a wavefront at the sub-aperture region. The decision to use a modal, zonal, or combination of sensing methods depends on its application. If the lower-order aberrations like tilt and defocus is dominating then modal analysis is used. For example, optical testing can be done in a small range of parameters. The optics under test is well-characterized through previous examinations. In mass production, optics has only a few aberrations to be checked each time, since some high-order components may not be important for the application. If higher order aberrations are present, then a zonal approach should be used [1]. The adaptive optics techniques are required to correct the wavefront affected by atmospheric turbulence. The aberrations present are of higher order. Adaptive optics wavefront sensing requires highly precision detector for wide range of wavelength [1].

Wavefront sensing can be done directly from recorded intensity. Many researchers have approached the problem, direct evaluation of Fraunhofer diffraction pattern [14-17] and multiple intensity patterns to extract the phase [18-19] by using phase retrieval techniques [20-22..]. J. R. Fienup in 1982 reviewed and compared a number of phase retrieval techniques. In this technique, intensity of the diffraction pattern is recorded, then with initial guess of the phase and using iterative algorithms phase information can be converged. The retrieval of the complex object information can be

directly done from the object autocorrelation using edge point referencing [23]. In these types of technique iterative algorithms are required which takes time to process. There may be possibility of not converging the phase information [24]. Some of important wavefront sensors are described in following sections.

1.2.1 Shack-Hartmann Sensor

The Shack-Hartmann wavefront sensor measures the wavefront gradients in two perpendicular directions over an array of sub-apertures (lenslet array) inside the telescopic pupil. Shack-Hartmann sensor is one basic techniques which convert wavefront slope into a change in illumination that can be measured photo electrically. Shack-Hartmann sensor consists of an array of lenslets of same focal length in which each one is focused into a photon sensor. The aberration can be found out from the local tilt of the wavefront across each lens from the position of the focal spot of the sensor. By measuring all the tilts from a sample of an array of lenslets, the whole wavefront can be approximated [25-26]. For each lenslet, the amount of spot displacement in two orthogonal directions is directly proportional to the slope of the wavefront at each lenslet that indicates the average phase tilt over the aperture. By assembling all these local flat tilted wavefronts, the input wavefront can be reconstructed and thus can be compared with the diffracted spots of a reference input beam. Indeed, Shack-Hartmann measures the 1st order derivative of the input wavefront [1].

Shack-Hartmann sensors have reached a high degree of sophistication. Binary optics enables the lenslet array to be fabricated with high precision and stability. The photon sensor used is a CCD array with high quantum efficiency and mechanical stability. It has high optical efficiency and has the ability to work with either pulsed or continuous reference sources [25-26]. It is completely achromatic as the slopes do not depend on the wavelength, it can also work on extended sources. However the resolution of a Shack-Hartmann wavefront sensor is equal to the sub-aperture size. If the atmospheric turbulence is high, more the higher order aberrations will be present.

Hence, phase variation smaller than the one micro lens will not be able to resolve. Its inflexibility with respect to wavefront tilt sensitivity and the inability to change the dynamic range during operation forms the drawbacks of the sensor [27].

1.2.2 Interferometric Wavefront Sensor

The relative phase of an optical wave can be measured by interfering it with another optical wave as a reference. In wavefront detection, the self-referencing interferometers (SRI) are considered to be good choices as separate reference optical field is not required. The information measured using such interferometers is the phase gradient. There are various self-referencing interferometers like lateral, radial and rotational shear interferometers are used to measure the phase gradient. This phase gradients information is used to realize the complete 2-D wavefront by various iterative algorithms [28]. The radial, rotational and lateral shearing interferometer gives phase gradient information along one coordinate i.e. radial, azimuthal and along lateral direction [29-31]. The reconstruction from the gradient data, especially for wavefronts lacking symmetry in Cartesian/polar coordinates, gradients along both orthogonal coordinates (x and y or radial and azimuthal) need to be measured [32].

To overcome the problem of reconstruction of 2D wavefront reconstruction, researchers have proposed a three wave interferometer based wavefront sensor [33-38]. It is an extension of the 1-D lateral shearing. In this type of wavefront sensor, input beam is sheared along two directions depending upon integration method used. To make it a single shot technique, three copies of input beam are made using reflection, diffraction [33-39]. Interferometers are very sensitive to vibrations so they are good to use in laboratory conditions like optical shop testing not for outdoor conditions. Another problem with interferometer is input beam should have enough coherence to get good contrast fringes. It has been shown that the wavefront can be sensed in the case of extreme UV low brightness source by suitably modulating the light source intensity distribution using Multi Incoherent Source Talbot Interferometer (MISTI) [40]

1.3 Analysis of wavefront from phase gradients

1.3.1 Variance matrix

One of the important wave propagation analyses is using variance matrix approach based on Wigner distribution [41-46]. This is because, the Wigner distributions can give faithful representation of quantum mechanics and so, a similar approach is possible in classical optics [42]. Later, Schempp [47] and Bastiaans [48-49] used Fourier transform of Wigner distribution function for signal processing design and first order optics. Simon and Mukunda based on phase space method synthesized ray and wave approach in to one using symmetrical structure existed between Wigner distribution function and quantum mechanics in many of their works [42-46]. Main advantage of their techniques is the formulation of symplectic invariants called as quality parameters which led to optical uncertainty principle. These invariant quality parameters have been studied extensively by the same authors for different class of beams [44-46]. The variance matrix (V) can capture the changes in wave-field characteristics upon its passage through a turbulent medium at the level of second moments [50-51]. The Variance matrix can be easily estimated with the available data for intensity and wave-field centroid position extracted from a Shack-Hartmann-Wavefront-Sensor (SHWFS) [52-57]. This does not involve any inbuilt wavefront reconstruction algorithm as is generally the case with SHWFS [58-64]. The Variance matrix estimation is the universal and repeatable, given the wave-field of same kind. In addition to this, the Variance matrix can also give certain other quantities of physical significance such as the Twist, the Symplectic Eigenvalues [50-51] and a distance measure between two Variance matrices. The Twist parameter measures the overall beam twist or rotation along the propagation direction and the Symplectic Eigen values are direct indicators of the presence of higher-order modes in a laser wave-field. The distance measure between two Variance matrices can be used as an effective tool towards checking the wave-field's symmetry in the 'x' and 'y'

directions and at the same time can compare the asymmetry between two Variance matrices calculated for the same wave-field in two different situations. Further the uncertainty principle, which puts a restriction on the Variance matrices that are physically possible, can be effectively used for the purpose of discarding the invalid data. This can act as a check on the experimental estimations of Variance matrices.

1.3.2 Zernike polynomials

Wavefront reconstruction is a standard mathematical process and is based on mathematical functions called Zernike polynomials [1, 65]. The Zernike polynomials are a sequence of polynomials that are orthogonal on the unit disk. The prediction of Zernike coefficients is very critical because they provide not only the overall performance but also provide insight into significant aberration coefficients of the wave front. These Zernike coefficients will thus become very useful tool in providing the scope for estimating actual performance and also correcting/optimizing the system performance. The Zernike polynomials have the advantage that, they represent balanced aberrations. Because of their orthogonality across a circular aperture, the Zernike polynomial coefficients are independent of each other. Each coefficient represents the standard deviation of the corresponding Zernike term (with exception of the piston term), and the variance of the aberration is equal to the sum of squares of Zernike the coefficients. However Zernike polynomials are not good for applying to fields with phase singularities.

Zernike polynomials are normally expressed in polar coordinates (ρ, θ) where $0 \leq \rho \leq 1, 0 \leq \theta \leq 2\pi$.

Each Zernike term consists of three components

$$z_n^m = [\text{Normalization factor}] * [\text{Radial polynomial}] * [\text{Azimuthal term}]$$

- 1) **Normalization factor:** Normalization factor for scaling different Zernike modes to unit variance is multiplied with the corresponding orthogonal polynomial which defines the Orthonormal Zernike circle polynomial.

- 2) **Radially dependent polynomial:** It describes the deviation of the wave front portion from zero mean.
- 3) **Azimuthal term:** Zernike term with $\cos(m\theta)$ and $\sin(m\theta)$ represents symmetric and asymmetric polynomial varying as $\cos(m\theta)$ and $\sin(m\theta)$ respectively.

Polar Representation: The polar representation of Zernike polynomial can be expressed as:

$$\begin{aligned}
 Z_n^m(\rho, \theta) &= N_n^m R_n^{|m|}(\rho) \cos(m\theta) \quad \text{for } m > 0, 0 \leq \rho \leq 1, 0 \leq \theta \leq 2\pi \\
 &= N_n^m R_n^{|m|}(\rho) \sin(m\theta) \quad \text{for } m < 0, 0 \leq \rho \leq 1, 0 \leq \theta \leq 2\pi \\
 &= N_n^m R_n^{|m|}(\rho) \quad \text{for } m = 0, 0 \leq \rho \leq 1
 \end{aligned} \tag{1.1}$$

Where

- n, m are positive integers and $n - m \geq 0$ and even.
- N_n^m is the normalization factor.

$$N_n^m = \sqrt{\frac{2(n+1)}{1+\delta_{m0}}} \delta_{m0} = 1 \quad \text{for } m = 0, \quad \delta_{m0} = 0 \quad \text{for } m \neq 0$$

1.4 Minimizing the effect of turbulence

1.4.1 Higher order Gaussian beams as light source

The topologically charged beams or standard Laguerre Gaussian (LG) beams have their characteristic physical properties such as barrel/dough-nut shaped intensity distribution, helical wavefront, centre phase singularity, ability to carry spin and orbital angular momentum and spatial propagation invariance [66-68]. The influence of atmospheric turbulence on beam quality is mainly restricted to Laser Gaussian beams however the optical vortex beams that possess an intensity null along their

propagation axis known as singular phase do not have such limitations. This is because there has been flurry of research works in propagation characteristics of Gaussian and topologically charged beams through atmospheric turbulence [69-78]. In one of their papers, Greg Gbur and Robert K Tyson showed the robustness of such topologically charged vortex beams when they propagate through weak and strong turbulence using multiple phase screen simulations [69]. This result showed that such vortex beams can be used for free space optical communications as they are insensitive to atmospheric turbulence. One of the major disturbances in free space optical communications is the scintillation effect due to atmospheric turbulence. Xiang long Liu et al showed that Gaussian Shell model vortex beams have less effect due to scintillation compared to Gaussian Shell model beams when they propagate through atmospheric turbulence [77]. They can be used as optical pipes, optical tweezers and optical spanners due to their rotational symmetry along propagation axis and intrinsic orbital angular momentum of \hbar per photon. Hence it is a powerful tool in the manipulation and control of microscopic particles. The most significant character of this beam is central vortex and partial coherence which enables to resist the effects of atmospheric turbulence. Standard LG beam of different orders can be generated using a spatial light modulator which acts as a reconfigurable diffractive optical element [77]. The circularly symmetric LG laser modes form an orthonormal complete basis set of solutions for paraxial light beams. The standard LG modes are characterized by two parameters, n and l that represent radial and azimuthal indices where l indicates orbital angular momentum of the beam. The standard LG beams describe a set of propagation modes where the equation for the radial electric field is proportional to the product of a Gaussian and an associated Laguerre polynomial $L(nl)$. The complex amplitude of Laguerre-Gaussian beam is as follows [77];

$$LG_m(r, \phi, z) = \sqrt{\frac{2n!}{\pi(n+|l|)!}} \frac{1}{w_z} \left(\frac{\sqrt{2}r}{w_z} \right)^{|l|} L_n^{|l|} \left(\frac{2r^2}{w_z^2} \right) \times \exp \left[-\frac{r^2}{w_z^2} + i \left(l\phi + \frac{kr^2}{2R_z} - ((2n+|l|)+1)\phi_g \right) \right]$$

(1.2)

Where (r, ϕ, z) are cylindrical-polar coordinates, k is the wavenumber, w_z is the beam width, R_z is the radius of curvature of the wavefront, ϕ_g is the Gouy phase and $L_n^{|l|}$ is the generalized Laguerre polynomial function.

$$w_z = w_0 \sqrt{1 + \left(\frac{z}{z_0}\right)^2}$$

where, z_0 is known as the Rayleigh range and w_0 is the waist radius.

$$R_z = z \left[1 + \left(\frac{z_0}{z}\right)^2 \right]$$

$$\phi_g = \tan^{-1} \left(\frac{z}{z_0} \right)$$

$$w_0 = \sqrt{\frac{\lambda z_0}{\pi}}$$

The lowest order standard Laguerre-Gaussian beam ($l=n=0$) is again the Gaussian beam. When $|l|$ is greater than zero, the electric field has an azimuthal phase change of $2\pi l$ which results in a phase singularity in the field and a node for the intensity at the centre of the beam. l in the phase factor $l\phi$ indicates the scaling for the phase variation as a function of the azimuthal angle ϕ [77].

The intensity of the standard Laguerre-Gaussian beam is a function of r and z , so that it is circularly symmetric. For $l \neq 0$, the beam has zero intensity at its centre ($r=0$) and an annular intensity pattern. The phase $\Phi(r, \phi, z)$ has the same dependence on r and z as does the Gaussian beam, except that the Gouy phase that is greater by a factor of $(l+2m+1)$ and there is an additional term proportional to the azimuthal angle ϕ . Because of the linear dependence of the phase on the azimuthal angle ϕ (for $l \neq 0$),

the wavefront assumes a helical form as the wave travels in the z direction. Beams with such spiral phase are of interest since they carry orbital angular momentum that can impart torque to the system under illumination.

LG beams are natural Eigen modes of optical systems whose optical surfaces are spherical and whose symmetry is cylindrical. The amplitude and phase images of LG_{01} beam is given in the Fig.1.1.

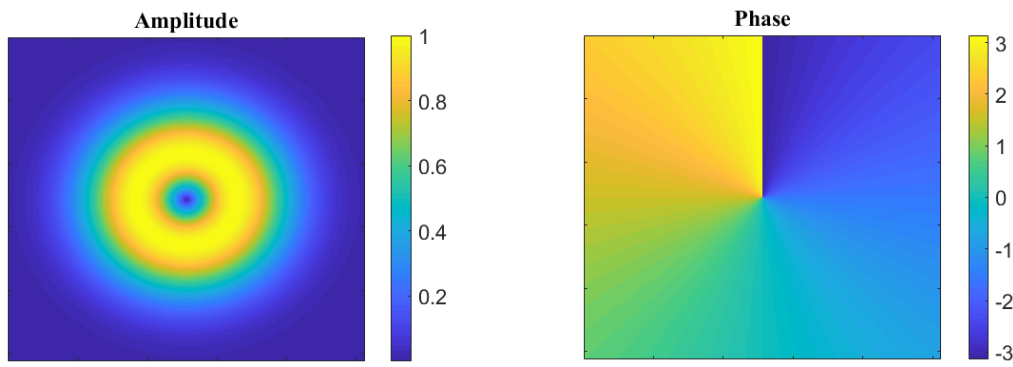


Figure 1.1 Amplitude and phase distribution of LG_{01} beam

Main reasons for considering the standard LG beams are due to their integrity even with the impact of turbulence [68 69 75 77 78] and due to that the vortex beams proved to have potential applications in free space optical communications (information carriers).

1.4.2 Adaptive optics

Adaptive optics is used to enhance the capability of optical systems by actively compensating for aberrations. Adaptive optics is real-time distortion-compensating systems. The aberrations can be represented in form of coefficients of Zernike polynomials [65] and these distortions can be corrected using adaptive optics by controlled adjustment of Zernike coefficients or disk harmonics of deformable mirror.

The most common adaptive optics system in use today consists of three subsystems i.e. a wavefront sensor, a deformable mirror and a control system [1].

1.5 Scope of the thesis

There have been several works in the recent past related to effects of atmospheric turbulence on light beams and the turbulence induced higher order aberrations [1-3, 7-8]. Overcoming the effects of atmospheric turbulence through adaptive optics plays an important role for free space optical communication and in imaging of distant objects in space using ground based telescopes. [1,68]. In the case of optical communication, one can also design the properties of source light beams so that it gets less affected by the atmospheric turbulence during its propagation [69-71]. In this thesis, the immunity of higher order Gaussian beams in maintaining its integrity during its propagation through atmospheric turbulence is experimentally investigated. Inferences from the investigation paved the way to explore wavefront sensing with higher resolution and better accuracy for the measurement of phase gradients. To achieve the accurate phase gradient measurement unaffected by amplitude variations in the optical field, interferometry based sensing scheme is proposed and experimentally demonstrated. For simulating the wavefront sensing using a natural light source or an artificially induced guide star, the proposed interferometer based wavefront sensor is tested with low coherent light source with finite spatial extent. The designs for maintaining the interference within temporal coherence domain and reviving the spatial coherence using diffraction effects ensured the sensing of wavefront.

1.6 Thesis Outline

In chapter 2, propagation analysis of laser Gaussian beam passing twice through a dynamic atmospheric turbulent mimicking Pseudo Random Phase Plate (PRPP) is carried out using variance matrix method. The characteristics like twist, symplectic Eigen values and asymmetry parameters are compared with characteristics of single

passage beams of topologically charged Laguerre Gaussian beams through same rotating PRPP.

In chapter 3, scintillation and beam wander study of turbulent impacted Gaussian and topologically charged vortex beams has been carried out. Aberration calculation on these beams using SHWFS has been done.

In chapter 4, wavefront detection using a common path vectorial shearing interferometer based wavefront sensor has been carried out. In this experiment 3 copies of input shearing beam is obtained using cascaded sagnac interferometer. The proof of principle of Vectorial shearing interferometer based wavefront sensor is carried out. Wavefront variation introduced due to change in position of collimating lens has been calculated and verified with simulated results.

In chapter 5, a comparative study on SHWFS and Vectorial interferometric wavefront sensor has been done. Aberrations introduced due to insertion of atmospheric turbulence mimicking pseudo random phase plate are measured and compared.

In chapter 6, sensing of low coherent wavefront is carried out using Vectorial shearing interferometer. The partial enhancement of spatial coherence is demonstrated by introducing a hard aperture at the source plane. The introduction of hard aperture at extended light source leads to the spatial coherence having Bessel distribution with extended side lobes. The fringe contrast has maintained at detection level by setting the lateral shear corresponding to one of the maxima of these side lobes. Wavefront of turbulent impacted (PRPP) low coherent wave has been detected using Vectorial shearing interferometer based wavefront sensor.

CHAPTER 2

Propagation analysis of double passage Gaussian and single passage topologically charged vortex laser beam using variance matrix

2.1 Introduction

Like conventional laser Gaussian beams, researchers have found that the Vortex beams (topologically charged) are also useful for free space optical communications [72, 79]. The vortex beams possess intensity and a helical phase structure with a point of undefined phase in the heart of helical phase structure. The phase variation around undefined phase known as singularity is in the order of $l (2\pi)$, where integer l stands for topological charge of the vortex beam. Unlike laser Gaussian beams, when these vortex beams propagate through atmospheric turbulence the normal turbulent impacted beam effects like scintillation, beam spreading and wandering are greatly reduced. These vortex beams with different topological charges can also be used for increasing data rate in free space optical communications using simultaneous multiplexing of different modes [72, 79]. Most of these beam characteristics analysis consider single passage through turbulence and many researchers [80-85] have shown the impact of enhanced back scattering of light beam through atmospheric turbulence when it passes twice through it. Recently, J. Yu et. Al [85] have reported that the enhanced backscattering behaviour of different topologically charged vortex beams through atmospheric turbulence, found that odd charges show negative enhancement and even charges show positive enhancement of backscattering. This is because enhanced backscattering of laser beams through atmospheric turbulence can be used for precision pointing and tracking. R. Sharma et. Al [86] have demonstrated that one can use variance matrix approach to characterize the turbulent affected He-Ne laser beam ($\lambda=632.8$ nm) using Shack-Hartmann wavefront sensor. Using the optical

invariant quality parameters like, optical uncertainty principle and symplectic Eigen values, we had analysed propagation of laser Gaussian beam through atmospheric turbulent mimicking Pseudo Random Phase Plate (PRPP). In this approach, unlike measuring conventional scintillation parameter, beam wandering and spreading of light beam through turbulence, we found twist parameter, asymmetry value of the beam and fluctuation of a turbulent infected He-Ne laser beam (6328 Å) using variance matrix. The wave propagation analysis using variance matrix approach requires the calculation of expectations of observable operators [50] on the wavefield and for a coherent wave field; this can be done in restricted manner by evaluating its second moments which is the elements of variance matrix (V).

In this chapter considering the paraxial scalar optics, propagation analysis of laser Gaussian beam passing twice through a dynamic atmospheric turbulent mimicking Pseudo Random Phase Plate (PRPP) is carried out and the characteristics is compared with characteristics of single passage beams of topologically charged c Laguerre Gaussian beams through same rotating PRPP. We used the optical invariant quality parameters like, optical uncertainty principle, symplectic Eigen values, for this turbulent impacted beam propagation analysis. The physical parameter from variance matrix like twist parameter(τ), asymmetry values (δ) of the beam and symplectic Eigen values (κ_1, κ_2) are used in this analysis which are obtained using Shack-Hartmann wavefront sensor as detector.

2.2 Beam propagation characterization using Variance matrix

The laser beam is a monochromatic light-field with the paraxial approximation travelling along the z axis can be described by its field amplitude as,

$$E(x, y, z, t) = E_0(x, y) \exp(-i(kz - \omega t)) \quad (2.1)$$

Where, $E_0(x, y)$ represents amplitude in its transverse plane, and $\exp(-i(kz - \omega t))$ indicates phase of that the light-field propagating close to the z axis. If the laser beam travels twice through the pseudo random phase plate (PRPP), the phase of such a double passage beam can be represented by $\Delta\phi$, then the transverse field amplitude $E(x, y)$ can be rewritten as,

$$E(x, y) = E_0(x, y) \exp(-i(\phi(x, y) + \Delta\phi)) \quad (2.2)$$

Where, $E_0(x, y)$ is the amplitude, $\phi(x, y)$ is the phase of light beam and $\Delta\phi$ represents the phase introduced in double passage laser beam through the pseudo random phase plate (PRPP) mimicking atmospheric turbulence. On the other hand, when the phase $\phi(x, y)$ has a singularity, then the light-field is said to carry a “charge” or angular momentum. A fundamental example for a laser light-field which possesses such a phase singularity is given by the Laguerre–Gaussian modes. In general a standard Laguerre Gaussian (LG) vortex beam with cylindrical co-ordinates is given by,

$$E_l(r, \phi) = \left(\frac{r}{w_z}\right)^{|l|} \times \exp\left[-\frac{r^2}{w_z^2} + il\phi\right] \quad (2.3)$$

In Eqn. 2.3, r is the radial coordinate, ϕ is the azimuthal coordinate and w_z is the transverse beam waist size. The azimuthal index l , corresponding to the topological charge of the LG vortex beam, indicates the number of twists of the helical wavefront within a wavelength and represents the amount of Orbital Angular Momentum. It can be positive or negative or zero.

In terms of rectangular co-ordinates for paraxial type LG beams passing through a pseudo random phase plate (PRPP) mimicking the atmospheric turbulence, the field component can be represented by,

$$E(x, y) = E_0(x, y) \exp(-i(m\phi + \delta\phi)) \quad (2.4)$$

Where, m takes integer values 0, 1, 2 etc., which determines the topological charges and the $\delta\phi$ term in Eqn.2.35 represents phase of LG beams single passage through PRPP. If $m=0$ then the beam will be simply Gaussian and if $m=1$ then it will be having topological charge 1 and for $m = 2$ it will be topological charge 2 and so on.

The variance matrix of a wave-field at a particular propagation distance z is estimated from the second moments of the “position” and “momentum” variables measured at various distances with respect to z . It can be estimated with the available data for the intensity and beam centroid position extracted from the Shack–Hartmann wavefront sensor (SHWFS). This does not involve any inbuilt wavefront reconstruction algorithm. The variance matrix estimation is thus universal and repeatable, given the same kind of wave-field. To get proper results the estimated V of an undistorted wave-field can be compared with the V corresponding to the distorted beam, i.e. the one, which is subject to pass through the random medium or turbulence mimicking medium such as a Pseudo-random phase plate (PRPP).

Now, the intensity of double passage beam through pseudo random phase plate mimicking atmospheric turbulence is given by,

$$I(x, y) = E_0(x, y) \exp(-i(\phi(x, y) + \Delta\phi)) \times E_0(x, y) \exp(i(\phi(x, y) + \Delta\phi)) \quad (2.5)$$

$$\begin{aligned}
I(x, y) &= |E_0|^2 \\
|E_0| &= \sqrt{I(x, y)}
\end{aligned}
\tag{2.6}$$

Calculation of variance matrix requires finding partial differentiation of intensity along x and y directions and it is given by,

$$\frac{\partial I(x, y)}{\partial x} = \frac{\partial |E_0(x, y)|^2}{\partial x} = 2|E_0(x, y)| \frac{\partial |E_0(x, y)|}{\partial x}
\tag{2.7}$$

$$\frac{\partial I(x, y)}{\partial y} = \frac{\partial |E_0(x, y)|^2}{\partial y} = 2|E_0(x, y)| \frac{\partial |E_0(x, y)|}{\partial y}
\tag{2.8}$$

Since we used Shack-Hartmann wavefront sensor's CCD for the intensity measurements, the intensity derivatives at a point (i, j) are given by,

$$\begin{aligned}
\frac{\partial I}{\partial x} &= \frac{I(i, j+1) - I(i, j)}{2\Delta x} + \frac{I(i, j) - I(i, j-1)}{2\Delta x} \\
\frac{\partial I}{\partial y} &= \frac{I(i, j+1) - I(i, j)}{2\Delta y} + \frac{I(i, j) - I(i, j-1)}{2\Delta y}
\end{aligned}
\tag{2.9}$$

In Eqn.2.9 the values Δx and Δy indicate the least count of the CCD i.e., the size of each pixel in millimetres in the x and y directions, respectively (here, it is 4.65 μm in both directions).

2.2.1 Variance Matrix

The variance matrix normally used for calculating beam propagation parameters like twist parameter (τ), symplectic Eigen values (κ_1 and κ_2) symmetry and asymmetry values (V_{as}) is given by following [87],

$$V = \begin{bmatrix} \langle \Delta \hat{x}^2 \rangle & \frac{1}{2} \langle \{ \Delta \hat{x}, \Delta \hat{p}_x \} \rangle & \langle \Delta \hat{x} \Delta \hat{y} \rangle & \langle \{ \Delta \hat{x} \Delta \hat{p}_y \} \rangle \\ \frac{1}{2} \langle \{ \Delta \hat{x}, \Delta \hat{p}_x \} \rangle & \langle \Delta \hat{p}_x^2 \rangle & \langle \{ \Delta \hat{p}_x \Delta \hat{y} \} \rangle & \langle \Delta \hat{p}_x \Delta \hat{p}_y \rangle \\ \langle \Delta \hat{x} \Delta \hat{y} \rangle & \langle \{ \Delta \hat{p}_x \Delta \hat{y} \} \rangle & \langle \Delta \hat{y}^2 \rangle & \frac{1}{2} \langle \{ \Delta \hat{y}, \Delta \hat{p}_y \} \rangle \\ \langle \{ \Delta \hat{x} \Delta \hat{p}_y \} \rangle & \langle \Delta \hat{p}_x \Delta \hat{p}_y \rangle & \frac{1}{2} \langle \{ \Delta \hat{y}, \Delta \hat{p}_y \} \rangle & \langle \Delta \hat{p}_y^2 \rangle \end{bmatrix} \quad (2.10)$$

Where the values of individual matrix elements are given by,

1. The term $\langle (\Delta \hat{x})^2 \rangle$:

$$\begin{aligned} \langle (\Delta \hat{x})^2 \rangle &= \langle (\hat{x} - \langle \hat{x} \rangle)(\hat{x} - \langle \hat{x} \rangle) \rangle \\ &= \langle (\hat{x}^2 - \hat{x} \langle \hat{x} \rangle - \hat{x} \langle \hat{x} \rangle + \langle \hat{x} \rangle^2) \rangle \\ &= \langle \hat{x}^2 \rangle - \langle \hat{x} \rangle \langle \hat{x} \rangle - \langle \hat{x} \rangle \langle \hat{x} \rangle + \langle \hat{x} \rangle^2 \\ &= \langle \hat{x}^2 \rangle - \langle \hat{x} \rangle^2 \\ &= \langle \hat{x}^2 \rangle - (c_1)^2 \end{aligned} \quad (2.11)$$

where, it should be noted that $\langle \hat{x} \rangle = c_1$ has been defined.

2. The term $\langle (\Delta \hat{y})^2 \rangle$:

$$\begin{aligned}\langle (\Delta \hat{y})^2 \rangle &= \langle \hat{y}^2 \rangle - \langle \hat{y} \rangle^2 \\ &= \langle \hat{y}^2 \rangle - (c_2)^2\end{aligned}$$

(2.12)

where, $\langle \hat{y} \rangle = c_2$.

3. The term $\langle (\Delta \hat{p}_x)^2 \rangle$:

$$\begin{aligned}\langle (\Delta \hat{p}_x)^2 \rangle &= \langle (\hat{p}_x - \langle \hat{p}_x \rangle)(\hat{p}_x - \langle \hat{p}_x \rangle) \rangle \\ &= \langle (\hat{p}_x^2 - \hat{p}_x \langle \hat{p}_x \rangle - \hat{p}_x \langle \hat{p}_x \rangle + \langle \hat{p}_x \rangle^2) \rangle \\ &= \langle \hat{p}_x^2 \rangle - \langle \hat{p}_x \rangle \langle \hat{p}_x \rangle - \langle \hat{p}_x \rangle \langle \hat{p}_x \rangle + \langle \hat{p}_x \rangle^2 \\ &= \langle \hat{p}_x^2 \rangle - \langle \hat{p}_x \rangle^2 \\ &= \langle \hat{p}_x^2 \rangle - (c_3)^2\end{aligned}$$

(2.13)

where again, $\langle \hat{p}_x \rangle = c_3$ has been defined.

4. The term $\langle (\Delta \hat{p}_y)^2 \rangle$:

$$\begin{aligned}\langle (\Delta \hat{p}_y)^2 \rangle &= \langle \hat{p}_y^2 \rangle - \langle \hat{p}_y \rangle^2 \\ &= \langle \hat{p}_y^2 \rangle - (c_4)^2\end{aligned}$$

(2.14)

where, $\langle \hat{p}_y \rangle = c_4$.

5. The term $\left\langle \frac{1}{2} \{ \Delta \hat{x}, \Delta \hat{p}_x \} \right\rangle$:

$$\begin{aligned}
\left\langle \frac{1}{2} \{ \Delta \hat{x}, \Delta \hat{p}_x \} \right\rangle &= \frac{1}{2} \left(\langle (\hat{x} - \langle \hat{x} \rangle) (\hat{p}_x - \langle \hat{p}_x \rangle) + (\hat{p}_x - \langle \hat{p}_x \rangle) (\hat{x} - \langle \hat{x} \rangle) \rangle \right) \\
&= \frac{1}{2} (\langle \hat{x} \hat{p}_x \rangle + \langle \hat{p}_x \hat{x} \rangle - 2 \langle \hat{x} \rangle \langle \hat{p}_x \rangle) \\
&= \frac{1}{2} (\langle \hat{x} \hat{p}_x \rangle + \langle \hat{p}_x \hat{x} \rangle) - (c_1 c_3) \\
&= \frac{1}{2} (\langle \hat{x} \hat{p}_x + \hat{p}_x \hat{x} \rangle) - (c_1 c_3) \\
&= \left\langle \frac{1}{2} \{ \hat{x}, \hat{p}_x \} \right\rangle - (c_1 c_3)
\end{aligned}
\tag{2.15}$$

6. The term $\left\langle \frac{1}{2} \{ \Delta \hat{y}, \Delta \hat{p}_y \} \right\rangle$:

$$\begin{aligned}
\left\langle \frac{1}{2} \{ \Delta \hat{y}, \Delta \hat{p}_y \} \right\rangle &= \left\langle \frac{1}{2} \{ \Delta \hat{p}_y, \Delta \hat{y} \} \right\rangle = \frac{1}{2} (\langle \hat{y} \hat{p}_y \rangle + \langle \hat{p}_y \hat{y} \rangle - 2 \langle \hat{y} \rangle \langle \hat{p}_y \rangle) \\
&= \frac{1}{2} (\langle \hat{y} \hat{p}_y + \hat{p}_y \hat{y} \rangle) - (c_2 c_4) \\
&= \left\langle \frac{1}{2} \{ \hat{y}, \hat{p}_y \} \right\rangle - (c_2 c_4)
\end{aligned}
\tag{2.16}$$

7. The term $\langle \Delta \hat{x} \Delta \hat{y} \rangle$:

$$\begin{aligned}
\langle \Delta \hat{x} \Delta \hat{y} \rangle &= \langle \Delta \hat{y} \Delta \hat{x} \rangle = \langle (\hat{x} - \langle \hat{x} \rangle) (\hat{y} - \langle \hat{y} \rangle) \rangle \\
&= \langle \hat{x} \hat{y} \rangle - \langle \hat{x} \rangle \langle \hat{y} \rangle \\
&= \langle \hat{x} \hat{y} \rangle - (c_1 c_2)
\end{aligned}
\tag{2.17}$$

8. The term $\langle \Delta \hat{x} \Delta \hat{p}_y \rangle$:

$$\begin{aligned}
\langle \Delta \hat{x} \Delta \hat{p}_y \rangle &= \langle \Delta \hat{p}_y \Delta \hat{x} \rangle = \langle (\hat{x} - \langle \hat{x} \rangle)(\hat{p}_y - \langle \hat{p}_y \rangle) \rangle \\
&= \langle \hat{x} \hat{p}_y \rangle - \langle \hat{x} \rangle \langle \hat{p}_y \rangle \\
&= \langle \hat{x} \hat{p}_y \rangle - (c_1 c_4)
\end{aligned}
\tag{2.18}$$

9. The term $\langle \Delta \hat{y} \Delta \hat{p}_x \rangle$:

$$\begin{aligned}
\langle \Delta \hat{y} \Delta \hat{p}_x \rangle &= \langle \Delta \hat{p}_x \Delta \hat{y} \rangle = \langle (\hat{y} - \langle \hat{y} \rangle)(\hat{p}_x - \langle \hat{p}_x \rangle) \rangle \\
&= \langle \hat{y} \hat{p}_x \rangle - \langle \hat{y} \rangle \langle \hat{p}_x \rangle \\
&= \langle \hat{y} \hat{p}_x \rangle - (c_2 c_3)
\end{aligned}
\tag{2.19}$$

10. The term $\langle \Delta \hat{p}_x \Delta \hat{p}_y \rangle$:

$$\begin{aligned}
\langle \Delta \hat{p}_x \Delta \hat{p}_y \rangle &= \langle \Delta \hat{p}_y \Delta \hat{p}_x \rangle = \langle (\hat{p}_x - \langle \hat{p}_x \rangle)(\hat{p}_y - \langle \hat{p}_y \rangle) \rangle \\
&= \langle \hat{p}_x \hat{p}_y \rangle - \langle \hat{p}_x \rangle \langle \hat{p}_y \rangle \\
&= \langle \hat{p}_x \hat{p}_y \rangle - (c_3 c_4)
\end{aligned}
\tag{2.20}$$

In the variance matrix elements there are two types, which are first order moments and the second order moments respectively. The first order moments related to the intensity measurements are given by following expressions,

$$\langle \hat{x} \rangle = \frac{\sum_{ij} x_{ij} I_{ij}}{\sum_{ij} I_{ij}}
\tag{2.21 (a)}$$

$$\langle \hat{y} \rangle = \frac{\sum_{ij} y_{ij} I_{ij}}{\sum_{ij} I_{ij}}$$

2.21 (b)

$$\langle \hat{p}_x \rangle = \frac{\sum_{ij} \left(\frac{x - x_0}{f} \right)_{ij} I_{ij}}{\sum_{ij} I_{ij}}$$

2.21 (c)

$$\langle \hat{p}_y \rangle = \frac{\sum_{ij} \left(\frac{y - y_0}{f} \right)_{ij} I_{ij}}{\sum_{ij} I_{ij}}$$

2.21 (d)

where $\langle \hat{x} \rangle$, $\langle \hat{y} \rangle$ represent position and $\langle \hat{p}_x \rangle$, $\langle \hat{p}_y \rangle$ represent momentum operators respectively. Similarly, the second order moments which, are related to the beam's width and angular divergence in the far field, are given by the following expressions,

$$\langle \hat{x}^2 \rangle = \frac{\sum_{ij} x_{ij}^2 I_{ij}}{\sum_{ij} I_{ij}}$$

2.22(a)

$$\langle \hat{y}^2 \rangle = \frac{\sum_{ij} y_{ij}^2 I_{ij}}{\sum_{ij} I_{ij}}$$

2.22(b)

$$\langle \hat{p}_x^2 \rangle = \lambda^2 \frac{\sum_{ij} \frac{1}{4I_{ij}} \left(\frac{\partial I}{\partial x} \right)_{ij}^2}{\sum_{ij} I_{ij}} + \frac{\sum_{ij} \left(\frac{x - x_0}{f} \right)_{ij}^2 I_{ij}}{\sum_{ij} I_{ij}}$$

2.22(c)

$$\langle \hat{p}_y^2 \rangle = \lambda^2 \frac{\sum_{ij} \frac{1}{4I_{ij}} \left(\frac{\partial I}{\partial y} \right)_{ij}^2}{\sum_{ij} I_{ij}} + \frac{\sum_{ij} \left(\frac{y - y_0}{f} \right)_{ij}^2 I_{ij}}{\sum_{ij} I_{ij}}$$

2.22(d)

and the second order moments of cross terms are given as,

$$\langle \hat{x} \hat{p}_x \rangle = \frac{\sum_{ij} x_{ij} \left(\frac{x - x_0}{f} \right)_{ij} I_{ij}}{\sum_{ij} I_{ij}}$$

2.23(a)

$$\langle \hat{y} \hat{p}_y \rangle = \frac{\sum_{ij} y_{ij} \left(\frac{y - y_0}{f} \right)_{ij} I_{ij}}{\sum_{ij} I_{ij}}$$

2.23(b)

Now, the observable operators array can be defined as $\{\xi_1, \xi_2, \xi_3, \xi_4\} = \{\hat{x}, \hat{p}_x, \hat{y}, \hat{p}_y\}$ for a given transverse field amplitude $A(x, y; z)$, for instance, $\Delta \xi_i$ is defined as $\Delta \hat{\xi}_i = \hat{\xi}_i - \langle \hat{\xi}_i \rangle$ with the expectation value $\langle \hat{\xi}_i \rangle = \int_{-\infty}^{\infty} \int_{-\infty}^{\infty} \psi^*(x, y; z) \hat{\xi}_i \psi(x, y; z) dx dy$. Then the entries V_{ij} of the variance matrix V corresponding to the transverse field amplitude $A(x, y; z)$ are defined as the expectation values $v_{ij} = \langle \Delta \hat{\xi}_i^\dagger, \Delta \hat{\xi}_j \rangle$ with i, j taking values from 1 to 4. In a more explicit form, the variance matrix V is defined as a 4×4 matrix which is written in block form following [87], Then the entries V_{ij} of the variance matrix V corresponding to the transverse field amplitude $E(x, y; z)$ for any propagating optical beam is defined as the expectation values $v_{ij} = \langle \Delta \hat{\xi}_i^\dagger, \Delta \hat{\xi}_j \rangle$ with i, j taking values from 1 to 4. In a more explicit form, the variance matrix V is defined as a 4×4 matrix which is written in block form following [86],

$$V = \begin{pmatrix} V^{11} & V^{12} \\ V^{21} & V^{22} \end{pmatrix} \quad (2.24)$$

Where, the terms are defined as

$$V^{11} = \begin{pmatrix} \langle \Delta \hat{x}^2 \rangle & \frac{1}{2} \langle \{ \Delta \hat{x}, \Delta \hat{p}_x \} \rangle \\ \frac{1}{2} \langle \{ \Delta \hat{x}, \Delta \hat{p}_x \} \rangle & \langle \Delta \hat{p}_x^2 \rangle \end{pmatrix} \quad (2.25)$$

$$V^{12} = (V^{21})^T = \begin{pmatrix} \langle \Delta \hat{x} \Delta \hat{y} \rangle & \langle \{ \Delta \hat{x} \Delta \hat{p}_y \} \rangle \\ \langle \{ \Delta \hat{p}_x \Delta \hat{y} \} \rangle & \langle \Delta \hat{p}_x \Delta \hat{p}_y \rangle \end{pmatrix} \quad (2.26)$$

$$V^{22} = \begin{pmatrix} \langle \Delta \hat{y}^2 \rangle & \frac{1}{2} \langle \{ \Delta \hat{y}, \Delta \hat{p}_y \} \rangle \\ \frac{1}{2} \langle \{ \Delta \hat{y}, \Delta \hat{p}_y \} \rangle & \langle \Delta \hat{p}_y^2 \rangle \end{pmatrix} \quad (2.27)$$

By substituting Eqns.2.25 2.26 and 2.27 in the matrix elements of Eqn.2.24, the variance matrix will reduce to Eqn.2.10. The important application of this variance matrix described in Eqn. 2.10 is for finding the beam propagation characteristics.

2.2.2 Characteristics of Variance matrix

From Eqns. 2.16 and 2.18, the 2×2 matrices V^{11} and V^{22} can be recognized individually as variance matrices for the variables $\Delta\hat{x}$ and $\Delta\hat{y}$ or the matrices for the two separate single modes.

For V^{11} ,

$$\begin{aligned} Det(V^{11}) &= \langle \Delta\hat{x} \rangle^2 \langle \Delta\hat{p}_x \rangle - \frac{1}{4} \left(\langle \{ \Delta\hat{x}, \Delta\hat{p}_x \} \rangle \right)^2 \\ &= \langle \Delta\hat{x} \rangle^2 \langle \Delta\hat{p}_x \rangle - \frac{1}{4} \left| \langle \{ \Delta\hat{x}, \Delta\hat{p}_x \} \rangle \right|^2 \end{aligned} \quad (2.28)$$

It should be noted that for two Hermitian operators $\Delta\hat{x}$ and $\Delta\hat{p}_x$

1. $\{ \Delta\hat{x}, \Delta\hat{p}_x \}$ is always Hermitian i.e.,

$$\{ \Delta\hat{x}, \Delta\hat{p}_x \}^\dagger = \{ \Delta\hat{x}, \Delta\hat{p}_x \} \quad (2.29)$$

2. $[\Delta\hat{x}, \Delta\hat{p}_x]$ is always anti-Hermitian i.e.

$$[\Delta\hat{x}, \Delta\hat{p}_x]^\dagger = -[\Delta\hat{x}, \Delta\hat{p}_x] \quad (2.30)$$

Proof for uncertainty principle for above mentioned operation derived using Schwartz inequality is given by,

$$Det(V^{11}) \geq \frac{\hbar^2}{4} \quad (2.31)$$

It is worth noticing that when the 2×2 matrix $V_{11/22}$ (V^{11}/V^{22}) has a (canonical) diagonal form,

$$V_{11/22} = \begin{pmatrix} \kappa & 0 \\ 0 & \kappa \end{pmatrix} \quad (2.32)$$

Then the statement of uncertainty principle takes the following form:

$$\begin{aligned} \text{Det}(V_{11/22}) &\geq \frac{\hat{\lambda}^2}{4} \\ \kappa^2 &\geq \frac{\hat{\lambda}^2}{4} \\ \kappa &\geq \frac{\hat{\lambda}}{2} \end{aligned} \quad (2.33)$$

where κ is the symplectic Eigen value.

The variance matrix V obeys the uncertainty principle and it can be stated as following [86],

$$V + \frac{i\hat{\lambda}}{2} \alpha \geq 0 \quad (2.34)$$

where, $\alpha = \sigma \oplus \sigma$ and $\sigma = \begin{pmatrix} 0 & 1 \\ -1 & 0 \end{pmatrix}$ with σ , the Pauli matrix. The operator \oplus

denotes the Kronecker sum. The variance matrix contains several important wave propagation physical parameters like twist of light beam (τ), the symplectic Eigen values denoting spread of light beams ($\kappa_{1,2}$), symmetry and asymmetry of propagating wave field (V_δ). Apart from these parameters using the intensity measurements one can find scintillation and beam wandering parameters of the propagating light beam.

2.3 Computation of Physically Significant Parameters from Variance matrix

The variance matrix completely specifies the wave-field, like symplectic Eigen values (κ_1, κ_2), twist parameters (τ) and symmetry (δ) of propagating light beams. These beam characteristics parameters are calculated from the Variance matrix.

2.3.1 Symplectic Eigen values (κ_1, κ_2)

A real linear transformation on the variables $\hat{\xi}$ with a 4×4 real matrix S such that following [88],

$$\hat{\xi} \rightarrow \tilde{\xi} = S\hat{\xi}$$

This transformation is canonical if $\hat{\xi}$ obeys the same commutation relationships as do $\tilde{\xi}$. This restriction amounts to saying,

$$\beta = S\beta S^T \quad (2.35)$$

where, $S \in S_p(2n, R)$. Since $n=2$ is being considered here $S \in S_p(4, R)$. The symmetric symplectic transform of the 4×4 matrix V under such S is as follows:

$$V' = SVS^T \quad (2.36)$$

If a given V is physically realizable then its Symplectic transform V' and the invertibility of S also guarantees the opposite statement. In order to check the realizability of a variance matrix, one needs to check the feasibility of the Symplectic

transform of V . A simple (canonical) form for the same with only diagonal entries is guaranteed by the following Williamson's Theorem: which states that,

“For any real symmetric positive definite $2n \times 2n$ matrix V , there exists $S \in S_p(2n, R)$ such that the symplectic transform of V by S has the canonical scaled diagonal form, unique up to the ordering of κ_j ”.

For $n=2$ case

$$\begin{aligned}
 V'' &= S V S^T \\
 &= \begin{bmatrix} \kappa_1 & 0 & 0 & 0 \\ 0 & \kappa_1 & 0 & 0 \\ 0 & 0 & \kappa_2 & 0 \\ 0 & 0 & 0 & \kappa_2 \end{bmatrix}
 \end{aligned} \tag{2.37}$$

Here κ_1 and κ_2 are referred to as symplectic Eigen values of V . the transformation expressed in (2.37) is not a similarity transformation, hence the Eigen values of V'' are not in general the Eigen values of V . However the transformation,

$$\begin{aligned}
 (V'' \beta)^2 &= S (V \beta)^2 S^{-1} \\
 &= -diag(k_1^2, k_1^2, k_2^2, k_2^2)
 \end{aligned} \tag{2.38}$$

is a similarity transformation and so the Eigen values of $(V \beta)^2 = -(V \beta)(V \beta)$ has a spectrum (of Eigen values) i.e., $k_1^2, k_1^2, k_2^2, k_2^2$. Thus one can evaluate the Eigen values of $-(V \beta)^2$ in order to calculate the symplectic Eigen values. These symplectic Eigen values indicate the presence of higher-order modes in the wave-field.

2.4.2 Twist Parameter (τ)

Twist parameter τ is the measure of how much a wave-field twists as it propagates along the z axis and it is given by:

$$\tau = \frac{1}{\lambda} \left(\langle \hat{x} \hat{p}_y \rangle - \langle \hat{y} \hat{p}_x \rangle \right) = \frac{1}{\lambda} \text{Tr} \left(V_{12} (-i\sigma_2) \right) \quad (2.39)$$

2.3.3 Asymmetry Parameter

The distance measure between two variance matrices can be used as an effective tool towards checking the wave-fields asymmetry in x and y directions and at the same time can compare asymmetry between two variance matrices calculated for the same wave-field in two different situations.

Given two variance matrices V_1 and V_2 , the quantity:

$$V_\delta = \frac{\text{Tr}(V_1 - V_2)^2}{\text{Tr}(V_1)^2 + \text{Tr}(V_2)^2} \quad (2.40)$$

V_δ captures how different the variance matrix V_1 is from the variance matrix V_2 . This quantity can be used to compare two wave-fields at the level of the second moments. If the two wave-fields are identical, then $V_\delta=0$, and if the two wave-fields are not identical, then $0 \leq V_\delta < 1$. Similarly, V_δ can also be used to capture the asymmetry of a wave-field in the x and y variables. Assuming $V_1 = V_{11}$ and $V_2 = V_{22}$ then $V_\delta = V_{as} = 0$ if the wave-field in consideration is symmetric. If the wave-field is asymmetric in the variables x and y, then $0 \leq V_{as} < 1$.

2.4 Experimental results and discussion

The experiment is divided into two parts. First the laser Gaussian beam is passed twice through rotating pseudo random phase plate which is turbulence mimicking simulator in laboratory condition. Second part involves the propagation of different topologically charged vortex beams through the same rotating PRPP. The intensity and centroid information for both cases are recorded using SHWFS at different distance from PRPP along z (beam propagation) direction.

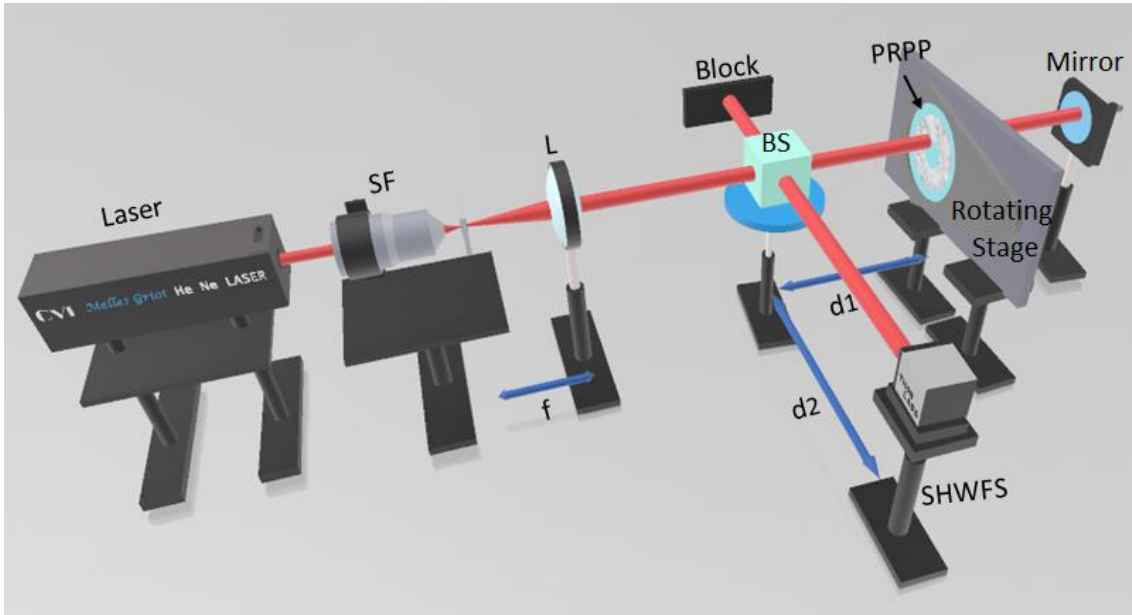


Figure 2.1 shows the experimental set-up for double pass laser Gaussian beam.

Fig. 2.1 shows the experimental geometry where, the collimated laser beam from He-Ne source is propagated through a rotating pseudo random phase plate (PRPP) mimicking atmospheric turbulence twice.

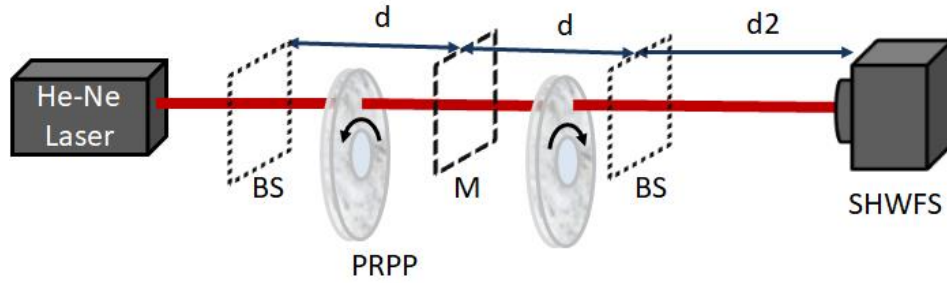


Figure 2.2 shows the conceptual arrangement of experimental geometry for Fig. 2.1

The Laguerre-Gaussian beam of different topological charges are passed through the same PRPP only once for a comparative analysis at various distances and the experimental geometry for single passage of propagation of LG beams of different topological charges is given in Fig. 2.3. In this part, vortex Phase plate is used to generate different topological charges. The vortex phase plate (manufactured by RPC Photonics.) geometry and its charge map are shown in Fig. 2.4(a) and (b) respectively.

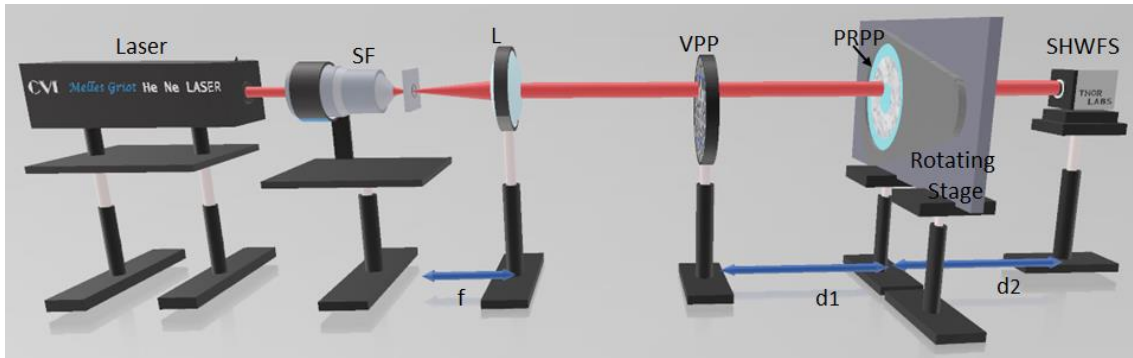


Figure 2.3 shows the experimental set-up for single pass laser vortex beam.

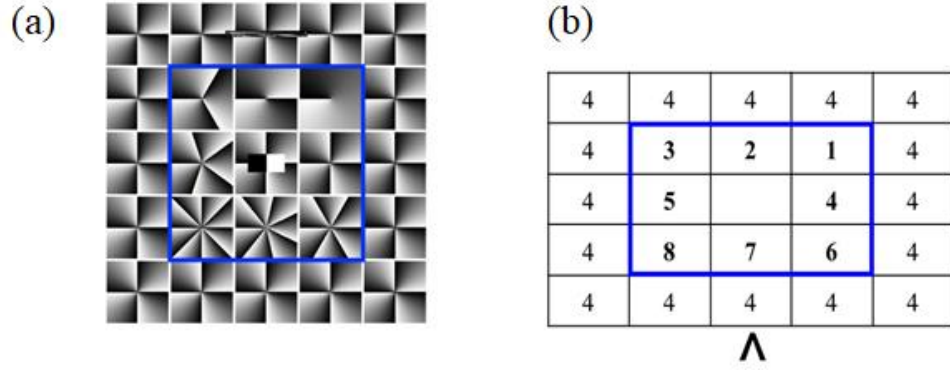


Figure 2.4 shows (a) Vortex geometry of phase plate and (b) Charge map of phase plate manufactured by RPC Photonics.

The working principle and details of Shack-Hartmann wavefront sensor is also given in Appendix-B and the details of pseudo random phase plate (PRPP) used in this experiment is given in Appendix-A respectively.

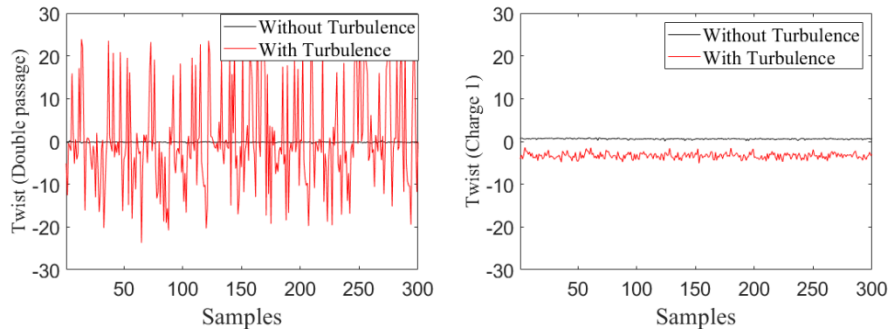
The propagation characteristics of a double passage of He-Ne Laser Gaussian beam and single passage of topologically charged 1, 3 (odd) and 2, 4 (even) Laguerre Gaussian beam through a dynamic (Rotating) turbulent mimicking PRPP are carried out using a Shack-Hartmann wavefront sensor. The Shack-Hartmann Wavefront Sensor used in this experiment consists of 10mm×10mm×2mm lenslet array having lenslet pitch of 150 μm and a 1280 \times 1024 pixels CCD with the size of each pixel being 4.65 μm \times 4.65 μm . The 1024 \times 1024 pixels CCD surface area of SHWS sensor is divided into 31 \times 31 domains, with these domains being labelled by indices i, j (starting from top most left corner) as has been shown in the Fig.B.1 and have values $1 \leq i, j \leq 31$. The incoming wavefront gets divided into 31 \times 31 parts, and each part is focused into a spot in one domain by its corresponding lenslet as shown in Fig. B.1. The spot centroid and intensity coordinates corresponding to each of these domains are labelled as x_{ij} , y_{ij} and I_{ij} respectively for position and intensity values respectively. Initially, using the geometry shown in Fig. 2.1 the laser beam from He-Ne laser is allowed to propagate after double passage through a distance d (d_1+d_2) and detected using SHWS. Then the PRPP is inserted at a distance from laser in such a way that the turbulent impacted beam can propagate same distance d like the previous

case. This will enable us to compare the turbulent fluctuations at same distances. After finding the twist parameter for a double passage laser beam through a dynamic (rotating) PRPP mimicking atmospheric turbulence, the experiment was carried out for odd and even topologically charged LG beams propagating through the same PRPP using the experimental geometry shown in Fig. 2.3. The topologically charged beams are generated using vortex phase plate (Fig. 2.4 a, b). Unlike double passage beams, the topologically charged beams (odd and even) pass through PRPP only once as it is evident from the geometry shown in Fig. 2.3.

The speed of rotating dynamic PRPP is adjusted to the same level of wavefront sensor speed so that the sensor sees the rotating PRPP as stationary. In a similar way using the experimental geometry shown in Fig. 2.3 first the intensities of topologically charged beams (Odd and Even) without propagating through PRPP is determined using the same Shack-Hartmann wavefront sensor and then after inserting the rotating PRPP the intensities of turbulent impacted topologically charged beams of all 4 charges have been measured for twist parameter calculations

2.4.1 Twist parameter

The twist parameters of a double passage beam through dynamic atmospheric turbulence mimicking pseudo random phase plate and the single passage of Laguerre Gaussian beams of odd charges (1, 3) and even charges (2, 4) through dynamic atmospheric turbulence mimicking Pseudo Random Phase Plate (PRPP) are analyzed at various propagating distances.



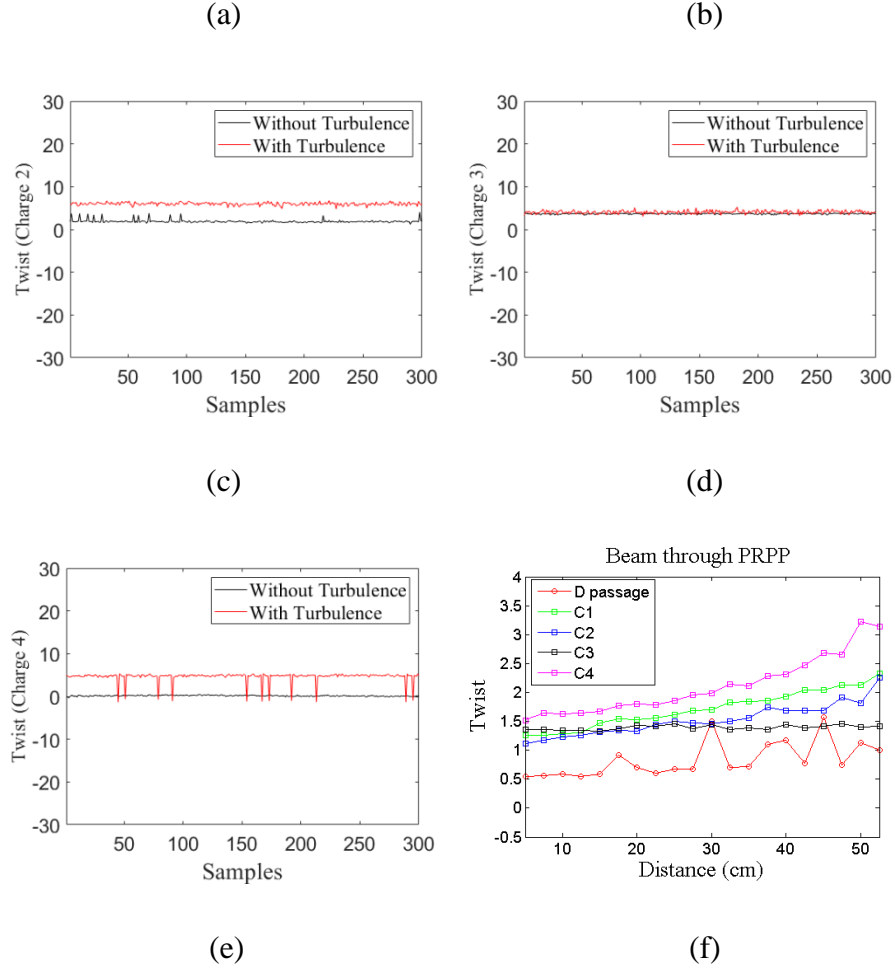


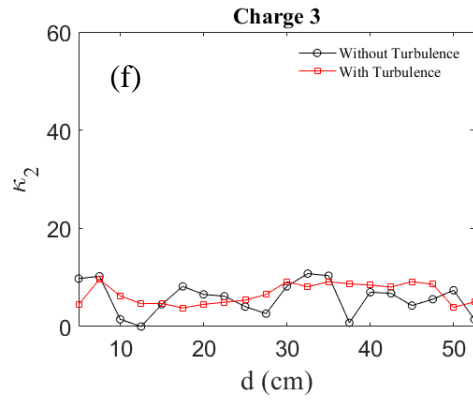
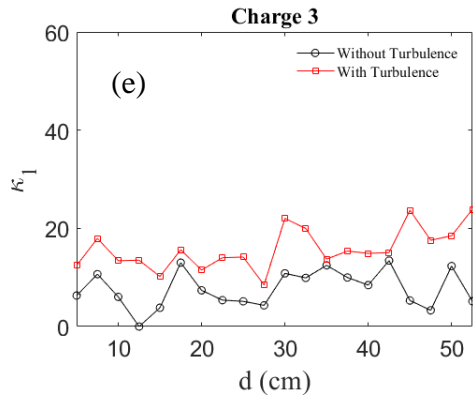
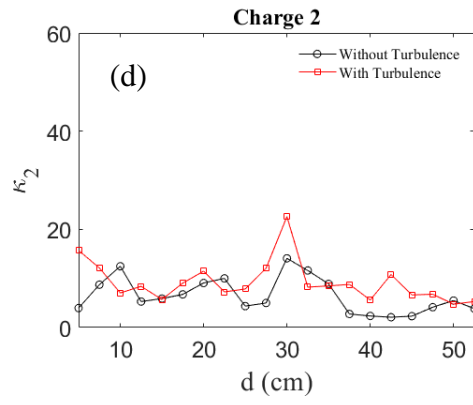
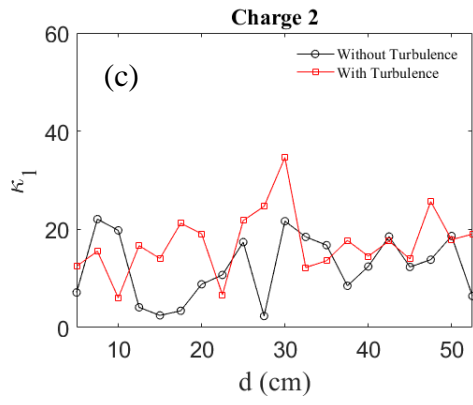
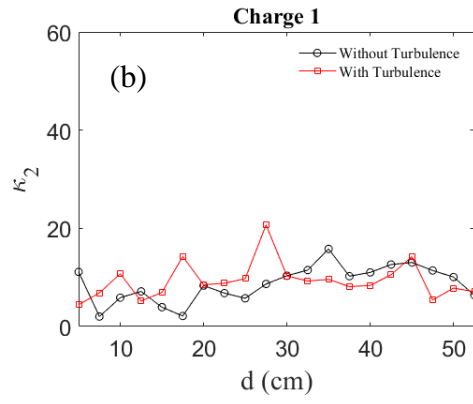
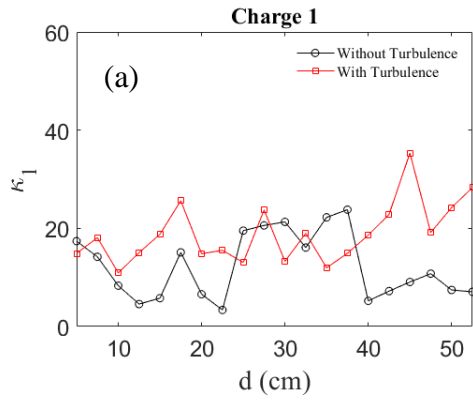
Figure 2.5 shows (a-e) Twist values for double pass Gaussian, vortex beam charge 1, 2, 3 and 4 respectively at 30 cm from PRPP. (f) Twist parameter for all beams at different distance from PRPP.

The twist parameter for a double passage beam is shown in Fig. 2.5(a), where at distance $d=30\text{cm}$, 300 samples at an interval of 2.5cm are measured using SHWS data and computed. The dark line shows the twist values for non-turbulent impacted beam (without inserting PRPP) and red lines show the twist parameter for a turbulence impacted (after insertion of rotating PRPP) double passage beam respectively. As expected the twist is more for the double passage beam through a rotating PRPP. Similarly Fig. 2.5 b, c, d and e show the twist parameters computed for the topologically charged LG beams with and without inserting rotating PRPP. It

can be seen from the Fig. 2.5 b, c, d and e the twist parameter is same for even charges (2, 4) at a particular distance ($d=30\text{cm}$) and it is different for odd charges (1, 3) at same distance. The twist values are not exactly matching with charge of the beam as the effect of external twist. The exact angular momentum (twist) cannot be calculated without knowing the proper point of origin [90]. Recently, J Yu et al [85] has shown that the topologically charged beams show enhanced back scattering effect on evenly charged beams and none for oddly charged beams for double passage vortex beams through turbulence. However in this case from Fig. 2.5, it is clear that evenly charged vortex beams show similar positive twist value compared with oddly charged vortex beams even for a single passage. This is an important observation in our analysis as for single passage of topologically charged beams, even charges that is 2, 4 show same positive twist values (Fig. 2.5c and 2.5e) and odd charge 1 shows negative twist value (2.5b) and whereas Charge 3 shows zero twist(2.5d)at same distance of measurement from PRPP. In case of double passage Gaussian beam, at the same distance i.e. 30 cm from rotating PRPP Fig. 5a shows large twist values in both positive and negative directions. Figure 2.5(f) shows a comparative plot computed for all 5 cases, and from that it is clear that as distance increases the charge 4 has highest twist value at a distance of 50 cm from the PRPP followed by charge 1, 2 and 3. It is interesting to observe that charge 3 has lowest twist values among all charges and its twist value is uniformly same up to 50 cm from 5 cm distance from the PRPP. Also, it is evident from Fig. 2.5(f), that the double passage beam has same twist value equivalent to charge 2, 3 at a distance 30 cm from PRPP and 45 cm from PRPP respectively. Thus the double passage beam acquires topological charge values of two and three at two distances as it propagates through turbulence.

2.4.2 Symplectic Eigen Values

The symplectic Eigenvalues of variance matrix for the double passage and the single passage of different topologically charged LG beams through dynamic PRPP are calculated.



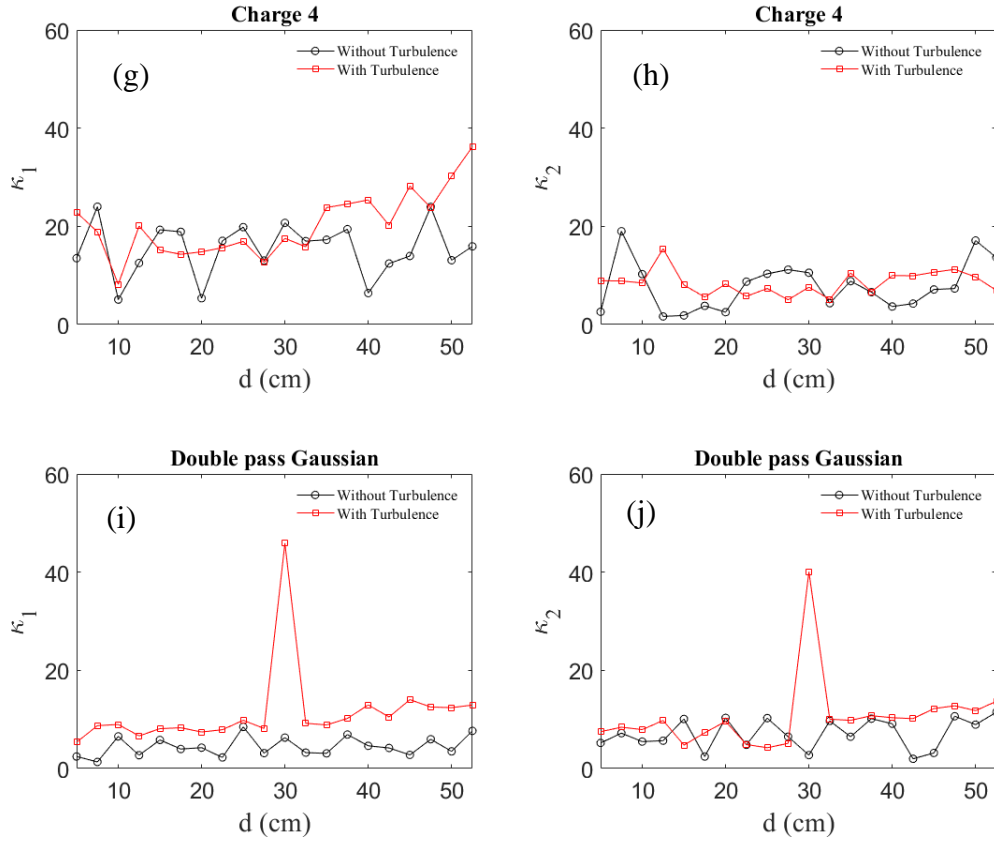


Figure 2.6 shows the plot of κ_1 and κ_2 for different charge-1 (a-b), charge-2 (c-d), charge-3 (e-f), charge-4 (g-h) beams and double passage Gaussian beam (i-j). Red and black colour plot shows symplectic Eigen values for beam with and without inserting rotating PRPP.

Figure 2.6(a) and (b) shows the symplectic Eigen values (κ_1 and κ_2) computed for the topologically charge-1 LG beams with and without inserting rotating PRPP. Figure 2.6(c) and 2.5(d) for charge 2 and so on. Thus, Figure 2.6(a), (c), (e), (g) and (i) show the κ_1 values for charges 1, 2, 3, 4 and double passage Gaussian beam respectively. Figure 2.6(b), (d), (f), (h) and (j) show the κ_2 values plotted with respect to distances from PRPP for charges 1,2,3,4 and double passage Gaussian beam respectively. The symplectic Eigen value κ_1 representing beam spread and presence of higher order modes show for charge 1 beam alternatively maximum and minimum values at various distances as the beam propagates after turbulence impact. The value reaches

maximum at a distance 45 cm but drops to 20 at 50 cm and again it increases (Fig. 2.6a). At the same time in other direction i.e. the symplectic Eigen value κ_2 for the same charge 1, has maximum value at a distance 28 cm but as beam propagates further it increases and decreases but, drops back to its initial value at a distance of 55 cm. In case of charge 2, the Eigen value κ_1 reaches maximum at 30 cm and again raises to second maxima 25 at a distance close to 50 cm. The κ_2 value for same charge 2 reaches maximum value of 25 at 30 cm and drops down close to its initial starting value at 55 cm. For charge 3 the maximum values for κ_1 reaches at 3 distances 30 cm, 45 cm and 55 cm and the value κ_2 shows uniformly flat curve and reach its initial value at 53 cm. The κ_1 value for charge 4 reaches maximum value only after the turbulent impacted beam reaches a distance of 53 cm and κ_2 value remains slightly higher than charge 3 but remains flat mostly and reaches lowest value even below turbulent un-impacted beam at 53 cm. Finally, the plot shown in Fig. 2.6i and 2.6j for double passage Gaussian beam show that the Eigen values κ_1 and κ_2 reach maximum at 30 cm and remains uniform before and after 30 cm distances. These plots clearly show that the topologically charged beams show instability of higher order modes as turbulent impacted beam propagates but twice turbulent impacted Gaussian beam show a strong higher order mode at 30 cm in both directions(κ_1 and κ_2).

2.4.3 Asymmetry Parameter

Asymmetry values for double passage and topologically charged beams are shown in Fig.2.7.

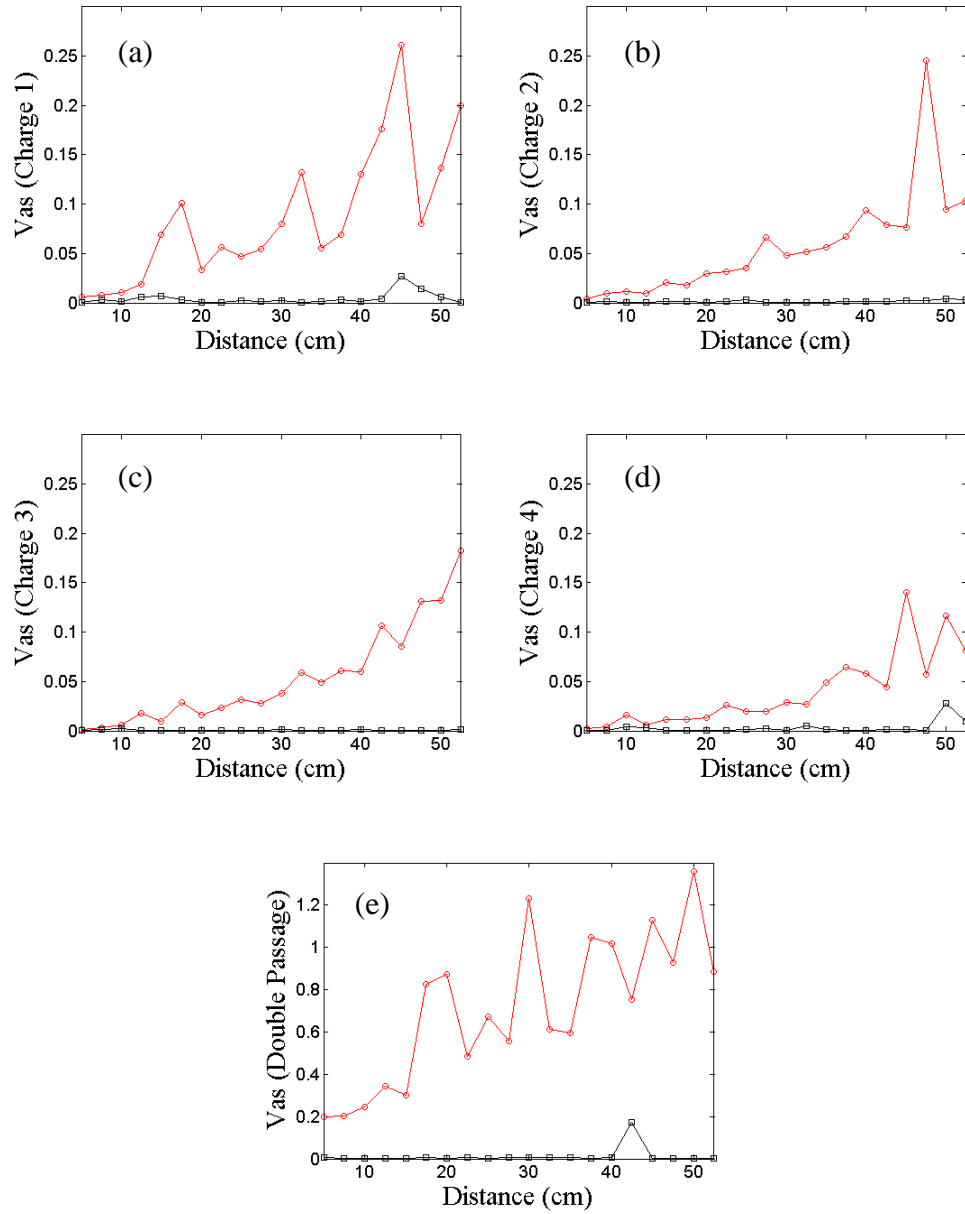


Figure 2.7 shows the plot of V_{as} for different charge-1 (a), charge-2 (b), charge-3 (c), charge-4 (d) beams and double passage Gaussian beam (e). Red and black colour plot shows Asymmetry values for beam passing through with and without rotating PRPP.

Figure 2.7 (a), (b), (c), (d) and (e) shows the Asymmetry parameter (V_{as}) computed for the topologically charged LG beams with (red colour) and without (black colour)

inserting rotating PRPP for the charges 1, 2, 3, 4 and double passage beam respectively. The asymmetry value for charge 1 reaches a maximum of 0.25 at a distance of 45 cm and then falls below .1 before it rises again to 0.2 at a distance of 53 cm. For charge 2 it reaches maximum value at a distance close to 50 cm and falls back to 0.1. For charge 3 the asymmetry gradually increases to a maximum of 0.18 at 52 cm and for charge 4 the asymmetry values are below 0.15 and only at a distance of 45 cm it touches 0.15. This reveal that charge 4 has more symmetry than all other topologically charged beams. On the other hand from Fig. 2.7e it is clear that double passage turbulent impacted Gaussian beam is more asymmetrical in nature as it propagates with its minimum value starting from 0.2 and reaching a maximum of 1.5 at 50 cm.

2.5 Observation

We have carried out a detailed experimental analysis of double passage Gaussian beam through a dynamic (rotating) pseudo random phase plate (PRPP) mimicking atmospheric turbulence and single passage topologically charged Laguerre Gaussian beams of odd and even charges. We used variance matrix analysis for finding twist parameter (τ), symplectic Eigen values (κ_1 and κ_2) and asymmetry parameter (V_{as}) of the turbulent impacted beams. i) The twist parameter has same positive twist values for even charges (2,4) at a distance of 30 cm and it is at zero level for charge 3 and shows negative twist value for charge 1 at the same distance. A comparative plot computed for all 5 twist values show that as distance increases the charge 4 has highest twist value at a distance of 50 cm from the PRPP followed by charge 1, 2 and 3. Charge 3 has lowest twist values among all charges and its twist value is consistence from 5cm to 50 cm. when twist parameters are compared it is found that the Gaussian beam passing twice through PRPP behaves like Laguerre Gaussian beams of charge 2 at a distance of 30 cm and charge 3 at a distance of 45 cm. ii) The symplectic Eigen value (κ_1) show stronger instability of higher order modes in one direction and symplectic Eigen value (κ_1 and κ_2) show lesser instability of higher

order modes in other direction. However for a double passage turbulent impacted Gaussian beam at a distance of 30 cm the Eigen values (κ_1 and κ_2) show strong stable higher order mode in both directions which is an interesting result. iii) The asymmetric parameter measurements at various distances clearly reveal that as topological charges increase the symmetry of beam increases and the asymmetry increases for double passage Gaussian beam as propagation distance increases.

Chapter 3

Insensitiveness of higher order topologically charged Laguerre Gaussian beams to dynamic turbulence impact

3.1 Introduction

One of the most important characteristics of the vortex beams is the topological charge which is measure of its angular momentum and remains stable under phase perturbations of the beam. The topologically charged vortex beams shows robustness when propagate through weak and strong turbulence using multiple phase screen simulations [69, 79]. Hence, vortex beams can be used for free space optical communications as they are insensitive to atmospheric turbulence. One of the major disturbances in free space optical communications is the scintillation effect due to atmospheric turbulence. Xiang long Liu et al showed that Gaussian Shell model vortex beams have less effect due to scintillation compared to Gaussian Shell model beams when they propagate through atmospheric turbulence [77]. There has been flurry of research works in propagation characteristics of Gaussian and topologically charged beams through atmospheric turbulence [69-79]. But, these works are mostly simulation based analysis, in this work we present the wave propagation analysis of Gaussian and topologically charged L-G beams through a dynamic (rotating) pseudo random phase plate which mimics atmospheric turbulence in real sense. There are two parts in our experimental analysis, with first one for determining scintillation index and beam wandering parameter for Laser Gaussian and topologically charged vortex beams of 4 charges(1, 2, 3 and 4) and the second one for determining Zernike Polynomials of turbulent impacted Laser Gaussian and topologically charged beams respectively. In this experiment, we have used a Pseudo-Random Phase Plate (PRPP) which is a turbulence mimicking random medium for generating artificial laboratory-level turbulence (Appendix A). The PRPP can be rotated at various velocities with

the help of a computer controlled stepper motor with a single driver, so that the time varying phase profile of turbulence can be achieved. Our detailed experimental results show the robustness of higher order topologically charged LG beams through a dynamic turbulence and their insensitiveness to refractive index fluctuations of atmospheric turbulence.

3.2 Experimental procedure and theory

3.2.1 Propagation characteristics of LG beams through a dynamic(Rotating) turbulence mimicking Pseudo Random Phase Plate (PRPP)

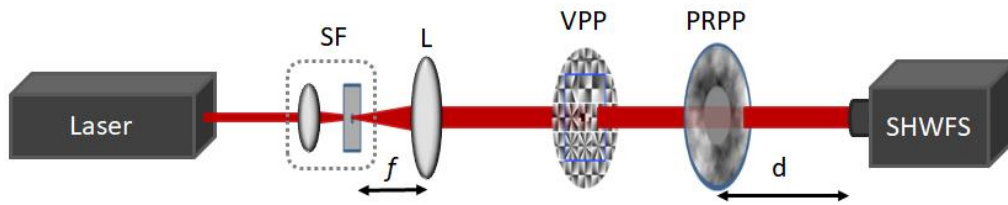


Figure 3.1 shows the experimental set-up for different topological charged beams passing through PRPP. In this set-up SF is Spatial Filtering assembly, L is collimating Lens, VPP is Vortex Phase plate, PRPP is Pseudo Random Phase Plate its details are given in Appendix-A and SHWFS is Shack-Hartmann Wavefront sensor.

3.2.2 Scintillations due to dynamic turbulent impact

Whenever, an optical beam passes through atmospheric turbulence intensity of light beam fluctuates and scintillation of light beam corresponds to this intensity fluctuations. The scintillation is mainly caused due to refractive index fluctuations in the turbulent atmosphere. While measuring the scintillations, at the ground based adaptive optics system, we assume that the power spectrum of the phase is taken as almost equal to the power spectrum of the relative fluctuations of the complex amplitude (neglecting the log-amplitude). Normally, the optical path fluctuations in

thin atmospheric layer like that of turbulence is considered to be smaller than 1 i.e. $\phi(\rho) < 1$ and therefore the field $E_h(r)$ immediately after the thin atmospheric turbulent layer can be written as [75-78],

$$E_h(r) = E_0 \exp(i\phi) \cong 1 + i\phi(r) \quad (3.1)$$

and after free propagation when it reaches ground based adaptive optics system via ground based telescope we get,

$$E_0(r) = 1 + i\phi(r) \times \frac{1}{i\lambda h} \exp\left(\frac{i\pi r^2}{\lambda h}\right) \quad (3.2)$$

Introducing the complex term in Eqn.2.4 as $C(r) = i\phi(r) \times \frac{1}{i\lambda h} \exp\left(\frac{i\pi r^2}{\lambda h}\right)$ and rewriting Eqn. 3.2 as,

$$E_0(r) = 1 + C(r) \quad (3.3)$$

The term $C(r)$ in Eqn.3.3 represents the relative fluctuations of the complex amplitude at the ground due to the turbulent thin layer at an altitude of h. The real part $\varepsilon(r)$ and imaginary part $\phi_0(r)$ represent relative fluctuations of phase $\phi(r)$ in the complex quantity $C(r)$ respectively.

The real part $\varepsilon(r) = \phi(r) \times \frac{1}{\lambda h} \cos\left(\frac{i\pi r^2}{\lambda h}\right)$ and the imaginary part

$\phi_0(r) = \phi(r) \times \frac{1}{\lambda h} \sin\left(\frac{i\pi r^2}{\lambda h}\right)$ follow Gaussian statistics as the phase is Gaussian.

Now, the complex field amplitude at the ground becomes,

$$E_0(r) = 1 + \varepsilon(r) + i\phi_0(r) \quad (3.4)$$

And the intensity $I(r)$ can be written after neglecting second order terms,

$$I(r) = |E_0(r)|^2 \cong 1 + 2\varepsilon(r) \quad (3.5)$$

The term $2\varepsilon(r)$ in Eqn. 3.5 describes the relative fluctuations of the intensity and one can measure the scintillation index which is defined by the term σ_I^2 and is normalized variance of irradiance fluctuation. The scintillation index is defined as,

$$\sigma_I^2 = \frac{\langle I^2 \rangle - \langle I \rangle^2}{\langle I \rangle^2} \quad (3.6)$$

Where, $\langle I \rangle$ is ensemble average of irradiance (Intensity) of the optical beam defined by Eqn. 3.5. The scintillation index is unit less quantity.

The experimental geometry shown in Fig. 3.1 is used for determining the scintillation index and beam wandering of the turbulent impacted topologically charged LG beams and laser Gaussian beams. The laser beam from a He-Ne laser is spatially filtered and collimated before it falls on a vortex phase plate (R C Photonics) which was used to generate topologically charged beams. The laser beam after passing through a vortex phase plate gets topologically charged and then it passes through a dynamic (Rotating) PRPP mimicking atmospheric turbulence as shown in Fig. 3.1. The turbulent impacted topologically charged beams then fall on a Shack Hartmann wavefront sensor. The Shack-Hartmann sensor is the image sensor, which provides high sensitivity and a wide dynamic range that are ideal for high precision measurement. The Thorlabs Shack-Hartmann sensor's CCD has an image resolution of 1.3 megapixels and sensitivity up to $\lambda/150$ and it has a wavelength range of 400-

900 nm. For laser Gaussian beam we have used the phase term given by Eqn. 2.3 and for topologically charged beams Eqn. 2.3 is modified to include the charge terms. Though the Laguerre Gaussian beams are represented in cylindrical co-ordinates for measuring scintillation index it can be in rectangular co-ordinates for paraxial type LG beams passing through a pseudo random phase plate (PRPP) mimicking the atmospheric turbulence. So, the complex electric field $E(r) = E_0 \exp(-i(m\phi + \delta\phi))$ where whenever $m = 0$ it is Gaussian and for 1, 2, 3.. the charges become 1,2,3 ... The term δ represents single passage accumulated phase through the dynamic turbulence. Initially, without introducing the vortex phase plate, only laser beam is allowed to pass through the rotating PRPP and then after introducing Vortex Phase Plate in the experimental set up shown in Fig. 3.1 the topologically charged beams are generated and allowed to pass through the rotating PRPP. Thus all beams including Laser Gaussian and topologically charged beams will be impacted by the turbulence.

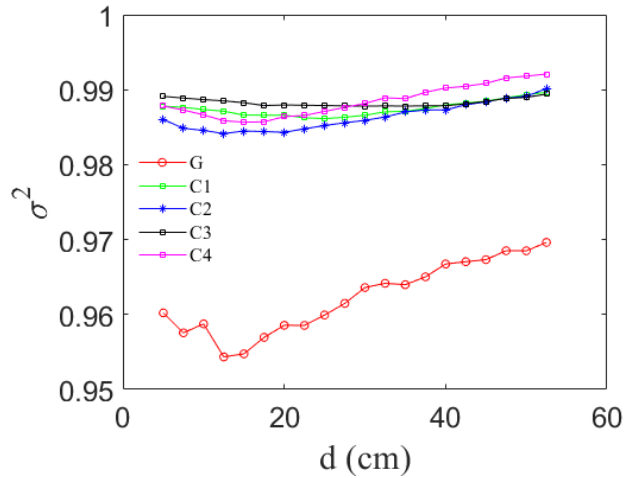


Figure 3.2 shows Scintillation index for Gaussian and topologically charged beams at different distance.

The speed of rotating PRPP is controlled using a stepper motor in such a way that it sees the Shack Hartmann Wavefront sensor at stationary. This helps us to record accurate values. The irradiance of the turbulent affected beams and its centroid points

are captured at various distances from PRPP by positioning the Shack-Hartmann wavefront sensor at various distances. In total 300 samples have been recorded at a plane 5 cm from the position of rotating PRPP. This process is then repeated at ten different planes with an interval of 2.5 cm. From the recorded irradiance data, the scintillation index i.e. σ_I^2 is measured and the same is plotted which is shown in Fig. 3.2. The intensity data for all 5 turbulent impacted beams are measured from a distance 5 cm from rotating PRPP to a maximum value of 55 cm. The plot in Fig. 3.2 clearly shows that the scintillation index fluctuates greatly for a laser Gaussian beam and minimum for topological charges 1, 2, 3 and 4 and is less than 1. The charge 4 shows small initial variations up to a distance of 20 cm and then increases a bit more compared to other charges. All other 3 charges show minimum scintillations effect. The vortex phase plate, operating on a Gaussian beam does not produce a LG beam, i.e. it is not a doughnut beam, but is a Gaussian beam with a step-like vortex. But after propagation it becomes a doughnut beam, as the step-like vortex is unstable. The scintillation effect could be due to the doughnut shape, rather than the vortex itself. Also, as the charge increases, the size of the dark centre increases, so this will make scintillation more stable. This result clearly establishes that topologically charged beams show minimum scintillation effects due to turbulent impact compared to laser Gaussian beam.

3.2.3 Beam wandering due to dynamic turbulent impact along x and y directions

Beam wandering effects in the turbulence atmosphere occurs, when a beam of light propagates through it due to random fluctuations in the refractive index [3]. In the turbulent field, the in-homogeneities scale ranges from few millimetres (l_0) to several meters (L_0) and those in-homogeneities which are large compared with the diameter of the propagating light beam tend to deflect the beam, whereas those in-homogeneities which are small compared with the beam diameter tend to broaden the light beam. Thus beam wandering effect occurs due to later i.e. smaller in-

homogeneities in which the laser beam waist is broadened. The beam wandering effect causes the centroid of laser beam to move randomly due to motion of individual eddies in the atmosphere [3, 71]. The beam wandering phenomena can be of two types i) jitter and ii) drift. The jitter type beam wandering is mainly due to fastness of wander and drift type beam wandering effect is due to slowness of wander in the turbulent field. The simplest way of determining beam wandering is by using Shack Hartmann wavefront sensor where the shift of centroid along x and y directions due to the impact of turbulent field can be directly measured. Fig. 3.3 shows a typical Shack-Hartmann wavefront sensor measuring the centroid shift of incoming aberrated beam.

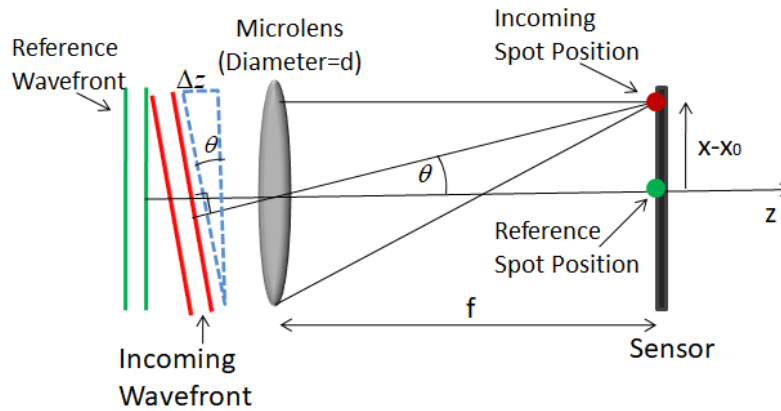


Figure 3.3a shows one micro lens of lens let array.



Figure 3.3b Spot diagram for plane reference beam. **Figure 3.3c** Spot diagram for aberrated beam

Fig. 3.3a, shows the un-distorted and distorted wavefront spot positions of a single lens of lens-let array of Shack Hartmann wavefront sensor along x-direction. The incoming wavefront, if it is perfectly collimated then at the detector of Shack-Hartmann wavefront sensor, we will get exact centre spots at the detector as shown in Fig. 3.3b due to all lens let arrays. On the other hand if it is distorted due to aberration of incoming wavefront then it will show displaced centroid spots as shown in Fig. 3c. For determining beam wandering of the turbulent impacted beam, since we require the centroid shifts along x and y direction in the transverse plane of incoming beam, we can directly get it from Shack-Hartmann wavefront sensor. In our experiment we recorded these centroid shifts along x ($x - x_0$) and y ($y - y_0$) directions for turbulent impacted Laser Gaussian beam, topologically charged beams for 4 charges (1, 2, 3 and 4) using a Shack-Hartmann wavefront sensor using the experimental geometry shown in Fig. 3.1. The centroid shifts along x and y directions are measured for all 5 turbulent impacted beams, at various distances starting from 5 cm to 55 cm from the rotating PRPP. The results are plotted for all 5 turbulent impacted beams and are shown in Fig. 3.4a and Fig. 3.4b for x and y directions centroid shift respectively. The beam wandering along x direction (Fig. 3.4a) for a turbulent impacted laser Gaussian beam (Blue colour) shows extreme positions from + 40 to $-5\mu\text{m}$ as the distance from rotating PRPP increases. The (-) sign represents the co-ordinate chosen keeping centre of the sensor as origin. For topologically charged beams the beam wandering values are positive and lesser than Laser Gaussian beam. Only topological charge 2 beam shows +24 μm value at a distance of 30 cm. Similarly, along y direction the beam wandering value goes from positive 13 μm to negative 12 μm as distance from rotating PRPP increases for a laser Gaussian beam (Fig. 3.4b). But for topologically

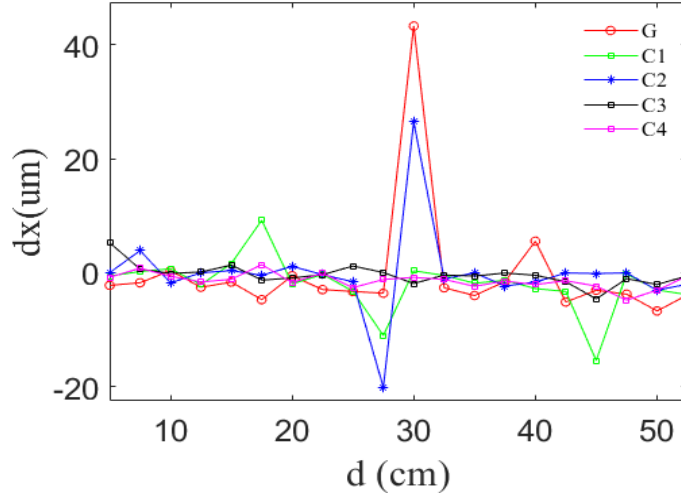


Figure 3.4a Beam wander in x-direction

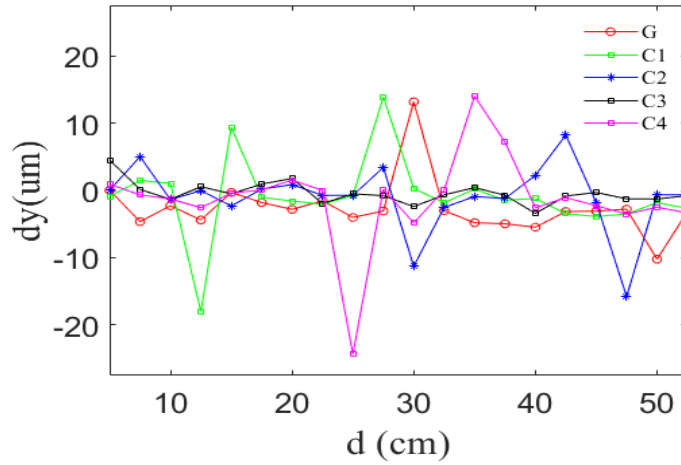


Figure 3.4b Beam wander in y-direction

charged beams the beam wandering values for charge 1 goes down to -19 from $13\mu\text{m}$ as distance increases along y-direction (Fig. 3.4b). For charge 2 goes down to -18 from $8\mu\text{m}$ as distance increases along y-direction. For charge 4 goes down to -22 from $14\mu\text{m}$ as distance increases along y-direction. For charge 3 the beam wandering values remain mostly positive along y-direction.

3.2.4 Intensity and Zernike polynomials measurements for turbulent impacted Laser Gaussian and topologically charged beams

In the second part of our experiment we generated the topologically charged Laguerre Gaussian beams as well as Gaussian beam using a Spatial Light Modulator. The amplitude and phase images of LG_{01} beam generated using SLM is given in the Fig. 3.5. The SLM used in the experiment is Holoeye PLUTO phase-only SLM based on reflective LCOS micro-displays with a resolution of 1920×1080 pixels and pixel size of $8\mu\text{m}$. It is optimized for different wavelength ranges (420-1700 nm). The phase patterns are set at the center of SLM. In this experiment we measured from the intensity patterns of turbulent impacted Gaussian and LG beams the Zernike Polynomials for obtaining lower and higher order aberrations.

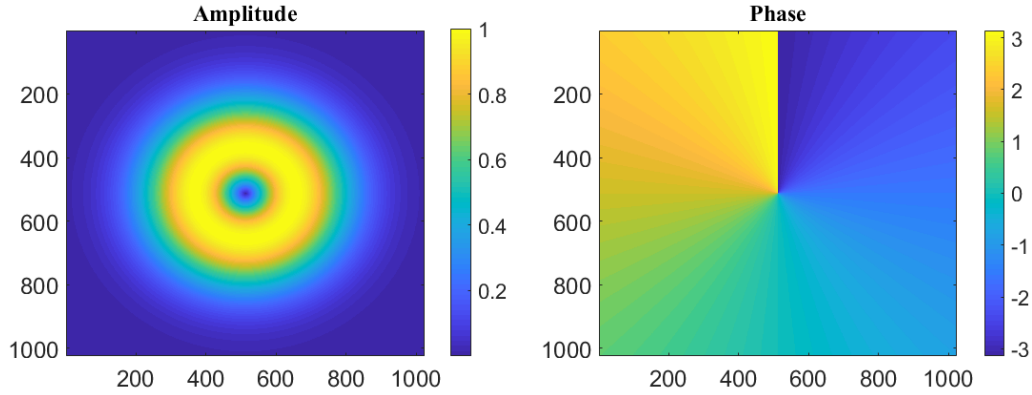


Figure 3.5 shows amplitude and phase distribution of LG_{01} beam.

Consider, Fig. 3.6 in which the light beam from He-Ne laser of 632.8nm wavelength is spatially filtered using spatial filtering assembly and falls on a collimation lens. The collimated laser beam further passes through a polarizer and falls on the spatial light modulator (SLM) in which the phase profile of Laguerre-Gaussian light beam of different modes is loaded. The information is loaded by the computer controlled phase hologram generated using MATLAB programming. The reflected beam from SLM then passes through a pinhole and mirror as shown in Fig. 3.6. The mirror reflects this beam towards the Pseudo Random Phase Plate (PRPP) which is fixed on

a rotary stage. The laser beam further gets split by a beam splitter to reach CCD (Charge Coupled Device) and Shack-Hartmann wavefront sensor simultaneously for detection. First the SLM is programmed to produce simple Gaussian beam by making $m=0$ and then it is allowed to fall on the Shack-Hartmann wavefront sensor and CCD camera. The Zernike polynomials and intensity of Gaussian beam without turbulence is recorded.

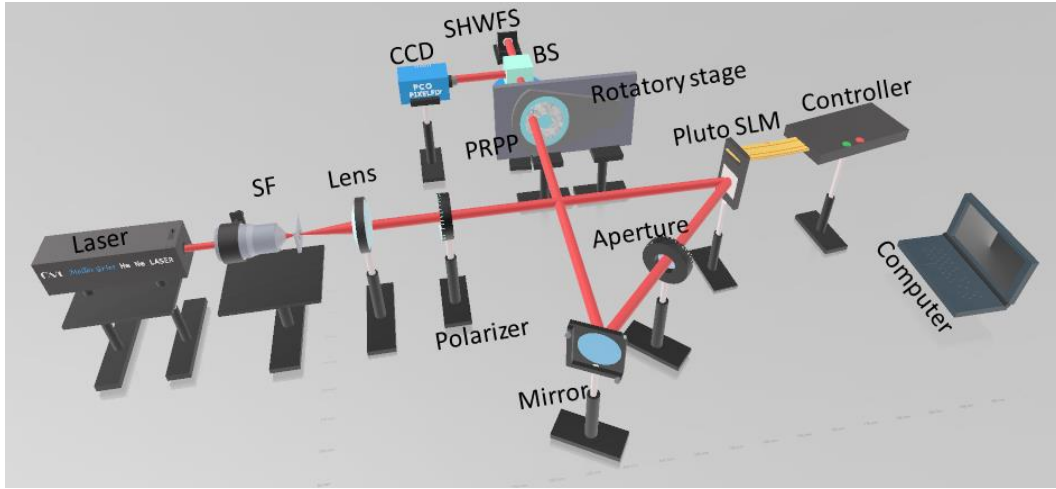
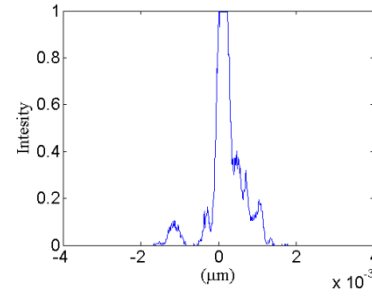
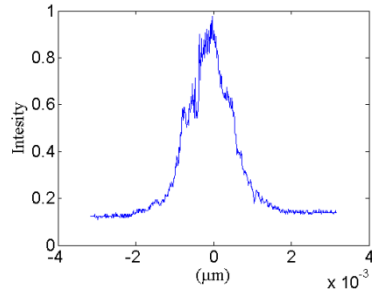
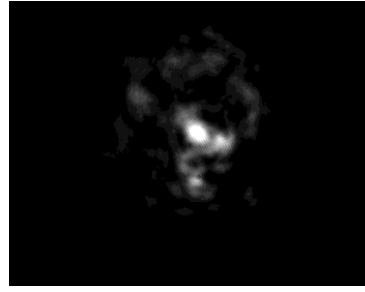
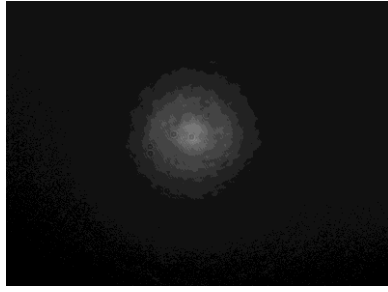


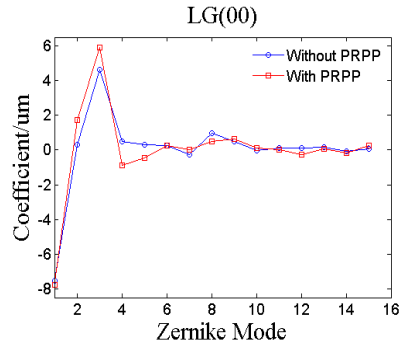
Figure 3.6 shows experimental set-up for SLM generated LG beam passing through PRPP.

Then the PRPP is introduced and rotated at a speed where the Shack-Hartmann wavefront sensor and CCD can record. Figure 3.7a, b and c show the intensity of Gaussian beam without propagating through turbulent beam and with propagating through turbulent beam and corresponding Zernike polynomials for both respectively. From Fig. 3.7 c it is clear that there is no much turbulent impact on higher order aberrations but variations occur due to lower order aberrations like tilt/piston. Then experiments are repeated for topologically charged beams of 1, 2 and 3 by propagating without and with dynamic turbulence using the same geometry shown in Fig. 3.6.



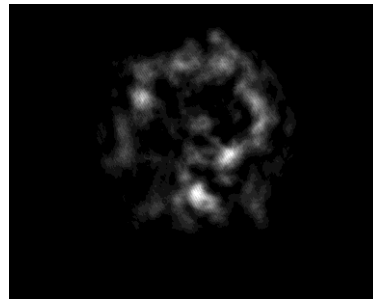
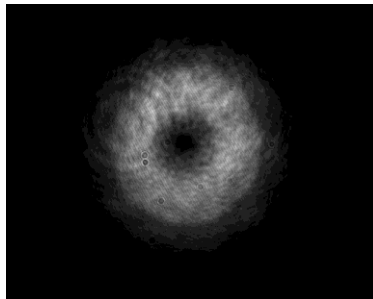
(a)

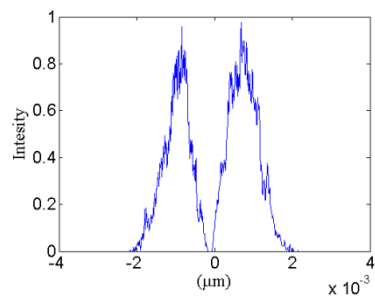
(b)



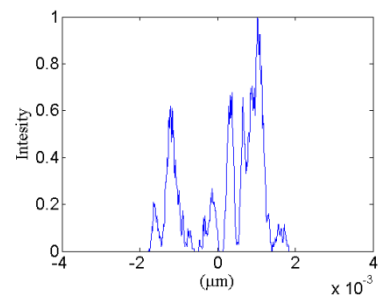
(c)

Figure 3.7 shows the recorded intensities and Zernike coefficients for different Gaussian charged beam.

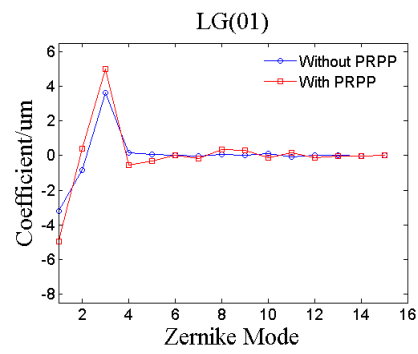




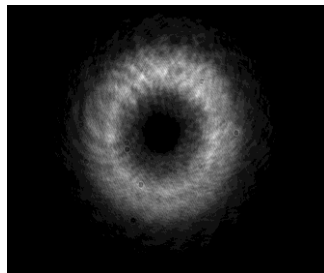
(a)



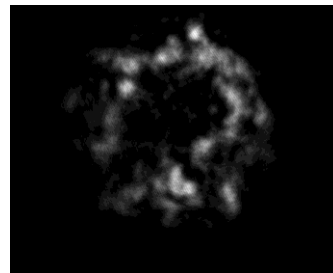
(b)



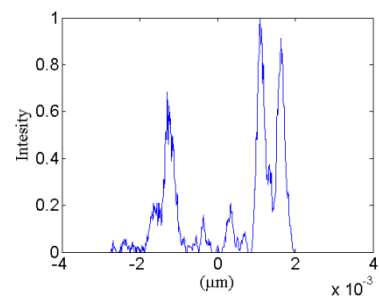
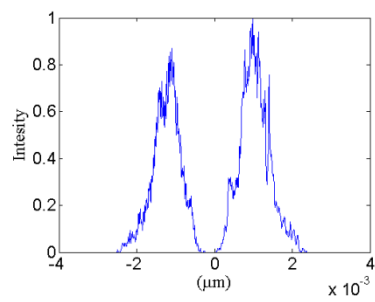
(c)

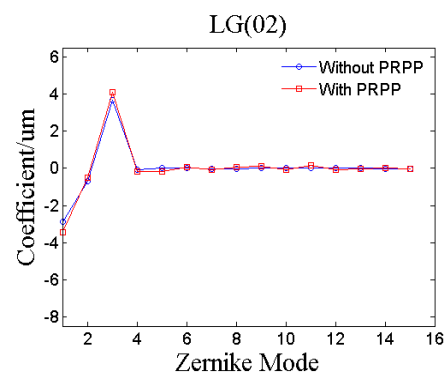


(d)

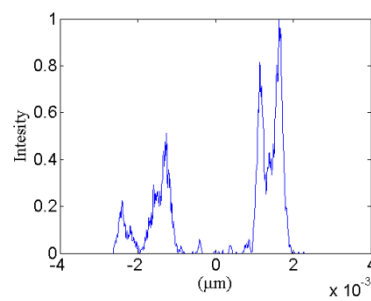
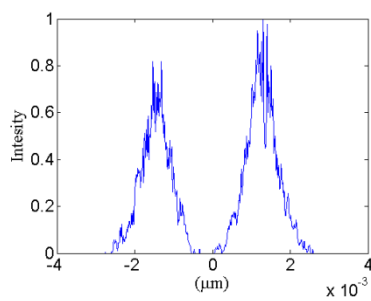
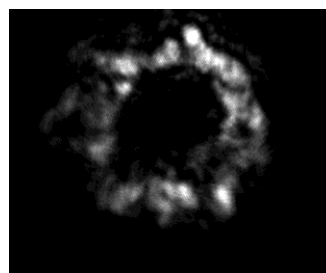
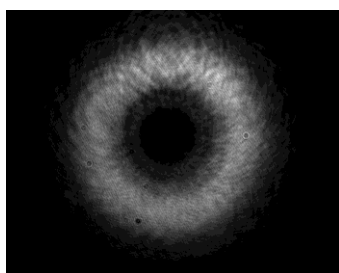


(e)



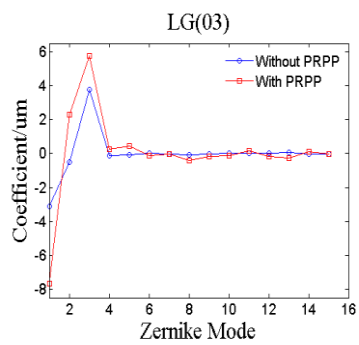


(f)



(g)

(h)



(i)

Figure 3.8 shows the recorded intensities and Zernike coefficients for different topologically charged beams.

The intensities are recorded and using Shack-Hartmann sensor Zernike polynomials are plotted. Figure 3.8a and b show the intensities of topologically charged beam for charge 1, without and with turbulent impact. Figure 3.8c shows the Zernike polynomials representing both higher order and lower order aberrations for both un-impacted and turbulent impacted beams respectively. Similarly for charge 2, Fig. 3.8 d, e and f show the influence of turbulence impact and finally for charge 3, Fig. 3.8 g, h and i show the intensities and Zernike polynomials for un-impacted and turbulence impacted beams respectively. The photographs of intensities of turbulent impacted Gaussian and 3 topologically charged beams show that compared to topologically charged beam with charge 1, the charge 3 has least impact of turbulence. Also, the Zernike polynomials of laser Gaussian and topologically charged beams, show almost similar values for lower and higher order aberrations for turbulent un-impacted and impacted beams respectively. The impact of dynamic turbulence is severe for laser Gaussian beam(Fig. 3.7 b), However it is much lesser for topologically charged beam of charge 3 (Fig. 3.8 h). These results clearly show that as topologically charge increases the robustness of Laguerre Gaussian beam increases considerably.

3.3 Observation

In detailed experimental analysis for measuring scintillation index and beam wandering values of a dynamic turbulent impacted laser Gaussian and topologically charged beams (Charges 1, 2, 3 and 4) has been performed. The experimental geometry shown in Fig. 3.6, used for finding Zernike polynomials of same turbulent impacted laser Gaussian and topologically charged (Charges 1, 2 and 3) beams respectively. It is observed that compared to Laser Gaussian beams, the topologically charged beams show much less scintillation index values. In case of beam wandering along both x and y directions, Laser Gaussian beam show large variations compared to topologically charged beams. It is observed in Fig. 3.7-3.8, when Gaussian and

Laguerre Gaussian beam passed through dynamic turbulence the charge of higher order beam retains.

It can be observed from the results shown in Fig. 3.7c and 3.8 (c, f, i) that change in lower order Zernike coefficients value (piston and tilt) for all beam with and without PRPP is distinguishable. However the higher orders Zernike coefficients values are not changing much. This may be because of under sampling of incoming wavefront from shack Hartman wavefront sensor. In experimental set-up in Fig 3.6, the PRPP is not imaged over SHWFS, so beam passing through PRPP is also propagating in free space before reaching to SHWFS. The r_0 fried coherence length for PRPP is 320 μm [88, 89] and size of one micro lens of SHWFS is 150 μm . So only 4 micro lenses are sampling that region which results in tilt information. For detecting the phase information properly, Wavefront sensor with more resolution will be required. This is the motivation for chapter 4.

Chapter 4

Vectorial shearing cascaded Sagnac interferometric wavefront sensor

4.1 Introduction

A wavefront sensor is device to measure the aberrations in an optical wave front. A wavefront sensor is immensely used in optical shop testing, ophthalmology and in adaptive optics system. Wavefront is the locus of field with same phase. It is difficult to get the direct phase at optical frequency due to the limited response time of available detectors. So, the phase has to be encoded into intensity for any meaningful measurement. The intensity change can be brought forward by refraction, diffraction or interference. As a result the fundamental aspects of light propagation paved the way for sensing the phase/phase gradients in the wavefront. The wavefront sensors that work on principle of intensity transport such as refraction and diffraction are micro-lens based Shack-Hartmann and grating based wavefront sensor respectively. The wavefront sensors based on intensity redistribution are interferometric wavefront sensors where the phase gradients are detected from the resulting intensity redistribution.

In the strong turbulence situation, interferometric sensors such as the self-referencing interferometer (SRI) are considered to be good choices. SRI has an inherent advantage that it does not require any separate reference optical field. However, the quantity that can be measured using such interferometers is not the phase of the optical field, but the phase gradient. The scalar interferometers like lateral, radial and rotational shear interferometers are used to measure the phase gradient. The phase gradients measured from either of them can give gradients along only single coordinate direction (x/y/radial/azimuthal). To realize the complete 2-D wavefront reconstruction from the gradient data, especially for wavefronts lacking

symmetry in Cartesian/polar coordinates, gradients along both orthogonal coordinates (x and y or radial and azimuthal) need to be measured.

To overcome the problem of reconstruction of 2D wavefront reconstruction, we propose a vectorial shearing interferometer based wavefront sensor. It is an extension of the 1-D lateral shearing and is able to displace the wavefront with a suitable amount in two orthogonal directions (x and y) and measure the corresponding interference independently. For a robust wavefront sensing scheme, all the three interfering copies of the wavefronts should ideally pass through the same path, encountering every element of the system, so that the system induced error does not reflect in the relative phase measurement. This is possible only in common path interferometer as it will ensure that no dynamically varying phase difference gets introduced between the interfering copies of wavefront. Keeping these points in mind, we have designed vectorial shearing wavefront sensor using a pair of cascaded Sagnac interferometers that allow spatial frequency multiplexing in the interferogram to detect the vector gradients simultaneously and independently along orthogonal directions x and y respectively. In this approach, the vector gradients are simultaneously extracted using Fourier transform method of fringe analysis and by two-dimensional numerical integration method for sensing a complete wavefront.

4.2 Principle of Vectorial Shearing wavefront sensor

The conceptual diagram for common-path vectorial shearing wavefront sensor is shown in Fig.4.1. The system is a combination of a pair of cascaded Sagnac interferometers and a 4-F telescopic system with two lenses of focal length f_1 and f_2 respectively. The core part of this system is the common path vectorial shearing interferometer. It is positioned between the lens L1 and its back focal plane. O is the object plane which is at Z_1 distance from plane-A i.e. focal plane of lens L1. The combination of lens L1 and vectorial shearing interferometer will generate four copies of the Fourier transform of input wavefront at plane-F which can be equally separated along x and y direction i.e. \hat{x}_s and \hat{y}_s respectively. The detailed alignment

to achieve it will be explained in experimental section. Plane-B is the back focal plane of the lens L2 where all four wavefront copies will completely overlap. Plane-I is the shearing plane at which wavefront can be sheared long two perpendicular directions simultaneously. Plane-I is at Z_2 distance from back focal plane of lens L2.

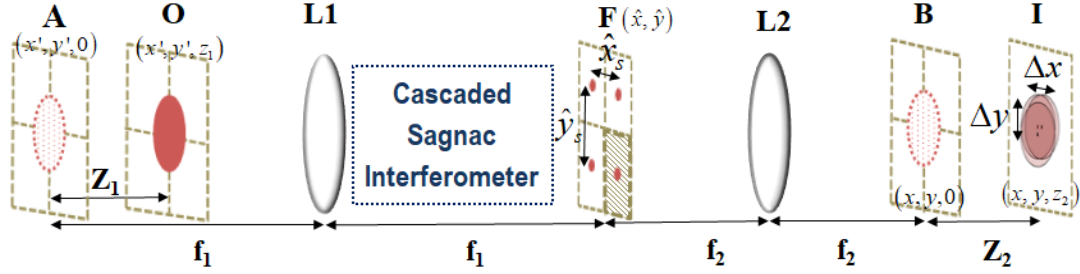


Figure 4.1 shows conceptual diagrams for common-path Vectorial shearing wavefront sensor

Let $u_o(x', y', \nu)$ be the field at object plane O corresponding to a monochromatic light component having frequency $\nu = c/\lambda$, where c is the velocity of the light and λ is the wavelength. The field at plane A will be following [91] as:

$$u_A(x', y', \nu) = F_{(f_1)}^{-1} \left\{ F_{(f_1)} [u_o(x', y', \nu)] \times \exp \left(-i \frac{2\pi z_1}{\lambda} \sqrt{1 - \frac{\hat{x}^2}{f_1^2} - \frac{\hat{y}^2}{f_1^2}} \right) \right\} \quad (4.1)$$

Where $F_{(f_1)}$ and $F_{(f_1)}^{-1}$ represents the Fourier and inverse Fourier transform due to lens L1. Field at plane F will be Fourier transform of field at plane-A and can be written as

$$U_F \left(\frac{\hat{x}}{\lambda f_1}, \frac{\hat{y}}{\lambda f_1}, \nu \right) = F_{(f_1)} [u_o(x', y', \nu)] \times \exp \left(-i \frac{2\pi z_1}{\lambda} \sqrt{1 - \frac{\hat{x}^2}{f_1^2} - \frac{\hat{y}^2}{f_1^2}} \right) \quad (4.2)$$

For brevity, the scaling and normalization factors are dropped from the equation. Now the field of shifted beam at plane F can be written as,

$$U_{FS}\left(\frac{\hat{x}}{\lambda f_l}, \frac{\hat{y}}{\lambda f_l}, \nu\right) = U_o\left(\frac{\hat{x} - \hat{x}_s}{\lambda f_l}, \frac{\hat{y} - \hat{y}_s}{\lambda f_l}, \nu\right) \times \exp\left(-i \frac{2\pi z_l}{\lambda} \sqrt{1 - \frac{(\hat{x} - \hat{x}_s)^2}{f_l^2} - \frac{(\hat{y} - \hat{y}_s)^2}{f_l^2}}\right) \quad (4.3)$$

Where, wavefront copies are shifted to each other by \hat{x}_s along \hat{x} -direction and \hat{y}_s along \hat{y} -direction. $U_{FS}(\hat{x}/\lambda f_l, \hat{y}/\lambda f_l, \nu)$ represents field of one of the shifted copies at plane F.

Field at plane B will be Fourier transform of the field at input focal plane of lens L2 (having focal length of f_2)

$$u_B(x, y, \nu) = F_{(f_2)} \left\{ U_{FS} \left(\frac{\hat{x}}{\lambda f_l}, \frac{\hat{y}}{\lambda f_l}, \nu \right) \right\} \quad (4.4)$$

$$u_B(x, y, \nu) = F_{(f_2)} \left[F_{(f_1)} \{ u_o(x', y', \nu) \} \times \exp \left(-i \frac{2\pi z_1}{\lambda} \sqrt{1 - \frac{\hat{x}^2}{f_1^2} - \frac{\hat{y}^2}{f_1^2}} \right) \right] \quad (4.5)$$

Now, field at shearing plane I, can written as

$$u_{I,n}(x, y, \nu) = F_{(f_2)}^{-1} \left\{ F_{(f_2)} [u_B(x, y, \nu)] \times \exp \left(i \frac{2\pi z_2}{\lambda} \sqrt{1 - \frac{\hat{x}^2}{f_2^2} - \frac{\hat{y}^2}{f_2^2}} \right) \right\} \quad (4.6)$$

Where, n in $U_{I,n}(x, y)$ represents the one of the copy of input field generated by cascaded Sagnac interferometer. Since we will select only three copies, so n can have values of 1, 2 and 3.

$$u_{I,n}(x, y, \nu) = F_{(f_2)}^{-1} \left[F_{(f_2)} \left[F_{(f_2)} \left\{ U_{FS} \left(\frac{\hat{x}}{\lambda f_1}, \frac{\hat{y}}{\lambda f_1}, \nu \right) \right\} \right] \times \exp \left(i \frac{2\pi z_2}{\lambda} \sqrt{1 - \frac{\hat{x}^2}{f_2^2} - \frac{\hat{y}^2}{f_2^2}} \right) \right] \quad (4.7)$$

Substituting the value of $U_{FS}(\hat{x}/\lambda f_1, \hat{y}/\lambda f_1, \nu)$ from Eqn.4.3 in above Eqn.4.7.

$$u_{I,n}(x, y, \lambda) = F_{(f_2)}^{-1} \left[\begin{aligned} & U_O \left(\frac{-\hat{x} - \hat{x}_s}{\lambda f_1}, \frac{-\hat{y} - \hat{y}_s}{\lambda f_1}, \lambda \right) \\ & \times \exp \left(-i \frac{2\pi z_1}{\lambda} \sqrt{1 - \frac{(\hat{x} + \hat{x}_s)^2}{f_1^2} - \frac{(\hat{y} + \hat{y}_s)^2}{f_1^2}} \right) \times \\ & \exp \left(i \frac{2\pi z_2}{\lambda} \sqrt{1 - \frac{\hat{x}^2}{f_2^2} - \frac{\hat{y}^2}{f_2^2}} \right) \end{aligned} \right] \quad (4.8)$$

Substituting the value of $z_1 = z_2/m^2$, $m = f_1/f_2$ in above equation, where m is the lateral magnification and m^2 is longitudinal magnification. After doing binomial expansion and rearranging the Eqn.4.8, field of one of the wavefront at plane-I can be written as:

$$\begin{aligned}
u_{I,n}(x, y, \nu) = & -\exp\left(i \frac{2\pi z_2}{\lambda} \left(1 - \frac{f_1^2}{f_2^2} + \frac{\hat{x}_{s,n}^2 + \hat{y}_{s,n}^2}{2f_2^2}\right)\right) \\
& \times \exp\left(-i \frac{2\pi}{\lambda f_2} (x\hat{x}_{s,n} + y\hat{y}_{s,n})\right) \\
& \times u_O\left(\frac{-I}{m}\left(x + \frac{\hat{x}_{s,n} z_2}{f_2}\right), \frac{-I}{m}\left(y + \frac{\hat{y}_{s,n} z_2}{f_2}\right), \nu\right)
\end{aligned} \tag{4.9}$$

The field at plane-I can be divided into three parts. The first shows a constant phase depending on the focal lengths of lenses L1 and L2 and image plane or shearing plane distance Z_2 from plane-B (the back focal plane of lens L2). Second part shows the presence of a linear phase which is a function of focal length of lens L2, the separation introduced at the output of the cascaded Sagnac interferometer i.e. $\hat{x}_{s,n}$ and $\hat{y}_{s,n}$ respectively. Part three shows the complex field of wavefront at plane O which is inverted, scaled by factor of $m = f_2/f_1$ and shifted by $\hat{x}_{s,n} z_2/f_2$ along x-direction and by $\hat{y}_{s,n} z_2/f_2$ along y-direction. Out of four copies generated, the three orthogonally sheared copies of the wavefront alone can be selected by spatially filtering them at plane-F. These three copies interfere at plane-I as shown in Eqn. 4.10 and the resulting intensity is recorded by a CCD.

$$I_I(x, y, \nu) = \left| u_{I,1}(x, y, \nu) + u_{I,2}(x, y, \nu) + u_{I,3}(x, y, \nu) \right|^2 \tag{4.10}$$

4.3 Experimental Procedure

The experimental set-up for the implementation of the Vectorial shearing is shown in Fig.4.1. It consists of telecentric system and cascaded Sagnac interferometer. The two cascaded Sagnac interferometers are shown in Fig. 4.2. First Sagnac shown in Fig.

2(a) consist of mirrors M1, M2 and beam splitter BS1. It generates two copies (1-red and 2-green) of input wavefront (blue) separated symmetrically along y-axis such that such separation between two copies is \hat{x}_s . The output of Sagnac-1 is given to the Sagnac-2 shown in Fig. 4.2(b). Sagnac-2 consists of mirrors M3, M4 and beam splitter BS2. It also generates two copies for every single wavefront at its input, but separate them symmetrically along x-axis. Thus the output of Sagnac-2 contains four copies i.e. 1', 2', 3' and 4'. The separation along y-direction is \hat{y}_s . This separation of wavefront along x and y direction can be controlled by shifting one of the mirror in Sagnac 1 and equal tilting of both the mirrors in Sagnac 2 as represented in Fig.4.2. By doing this we achieve co-propagating but spatially separated copies of wavefront.

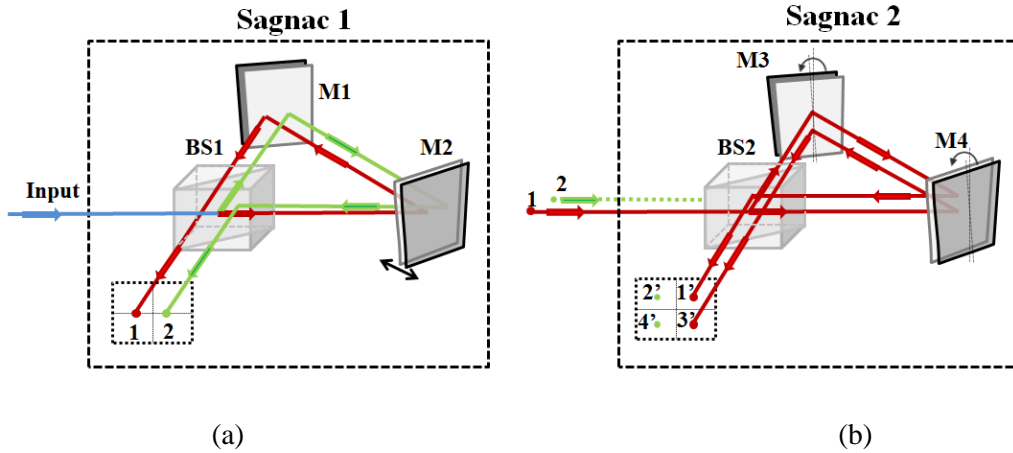


Figure 4.2 Generation of four copies of the wavefront using two Sagnac interferometers kept in series.

By introducing the lens L1 (focal length $f_1 = 500\text{mm}$) at the input of the cascaded Sagnac interferometers, four copies represented as 1', 2', 3' and 4' becomes Fourier transform $U_{FS}\left(\frac{\hat{x}}{\lambda f_1}, \frac{\hat{y}}{\lambda f_1}, \nu\right)$ related to the input wavefront $u_o(x', y', \nu)$ as represented in Eqn. 4.2. The lens L2 (focal length $f_2 = 200\text{mm}$), introduced at the output of the cascaded Sagnac interferometer performs another Fourier transform in order to obtain $u_{l,n}(x, y, \nu)$ at plane I. We record the interferogram of laterally sheared beams, described by Eqn. 4.10, on CCD (PCO pixelfly, 1392x1040, with pixel size of 6.4 μm)

kept at plane I, located at a distance $z_2 = 18\text{mm}$ from plane-B, the back focal plane of lens L2. Being nearly common-path geometry allow us to cancel any system induced errors and surrounding vibrations. .

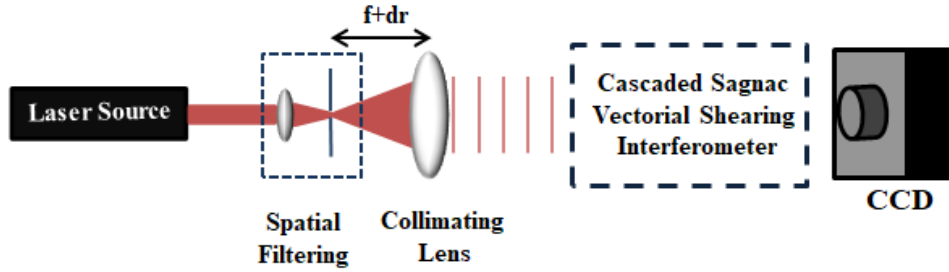


Figure 4.3 Wavefront sensing using vectorial shearing interferometer.

Experimental set-up to validate vectorial shearing cascaded Sagnac interferometric wavefront sensor is shown in Fig. 4.3. In this set-up, a He-Ne laser (633nm) is used as a source whose output is spatially filtered and then collimated with lens L having focal length f of 100mm. This collimated beam is fed as input to the vectorial shearing wavefront sensor followed by CCD. As the position of the collimating lens L changes ($f+dr$), the shape of the beam changes. Depending upon the direction in which the lens is moved the beam output may be converging or diverging. The collimating lens is moved in direction towards the VSWFS with step size of 0.5mm. Corresponding to each position of lens the interferogram is recorded with 8-bit CCD as shown in Fig 4.4(a).

4.4 Results and Analysis

The recorded interferogram when the collimating lens is shifted by an amount of $dr=3\text{mm}$ from the initial position is shown in Fig 4.4(a). The selected region of interferogram for processing is marked with white color square (having each side of 2.6mm). The spatial carrier frequency multiplexed interfered data corresponds to the superposition of three sheared wavefronts. The phase gradients can be obtained using

Fourier transform method of fringe analysis [92-94]. Fig. 4.4(b) shows the 2D Fourier spectrum of the recorded interferogram with spatial frequencies f_x and f_y represented as $\hat{x}_s/\lambda f_2$ and $\hat{y}_s/\lambda f_2$. There are seven spots in Fig. 4.4(b) in which the center one is the zeroth order term representing the dc-part in the recorded interferogram. The upper three are resulting from the mutual superposition of sheared wavefronts. They get separated due to the spatial carrier frequency introduced. Their conjugates appear at the lower side. Out of the upper three spots, one along x-direction and one along y-direction is selected (marked with yellow circle) and filtered out. The spatial filter having diameter of 400 μ m is used in our experiment. After doing inverse Fourier transform of the selected spot, phase of the complex field can be calculated. However, precise amount of the spatial carrier frequency introduced should be known. In addition, it should be noted here that during the alignment of the cascaded Sagnac interferometers and the accompanying lenses, there can be system induced aberrations which should be cancelled. Therefore, the phase of the complex field obtained for a particular case is always compared to that obtained for the initial condition of a well collimated beam; thereby automatically cancelling the spatial carrier frequency and the system induced aberrations.

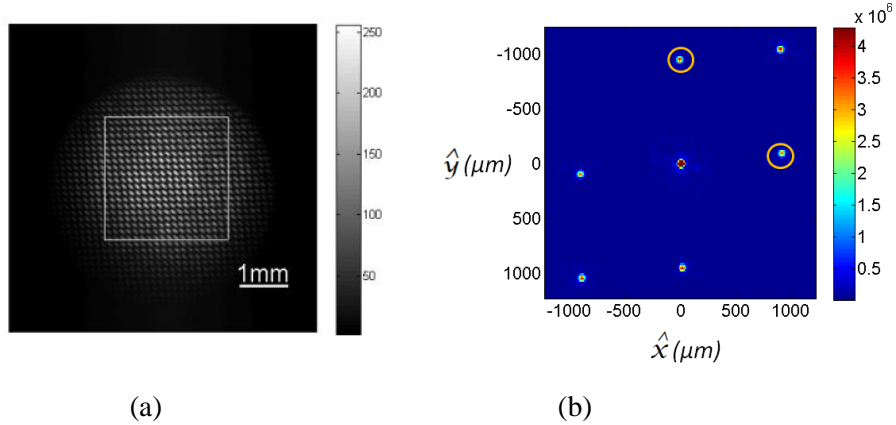
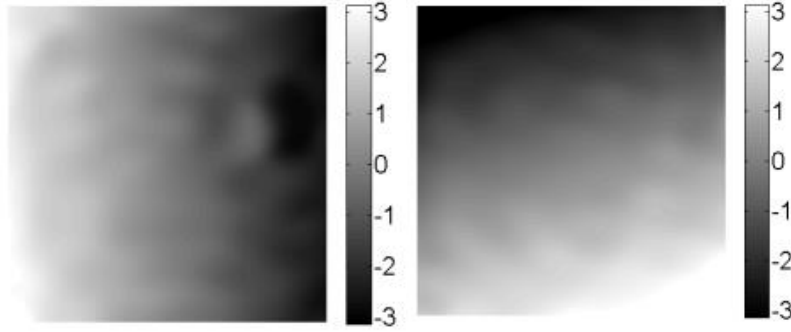


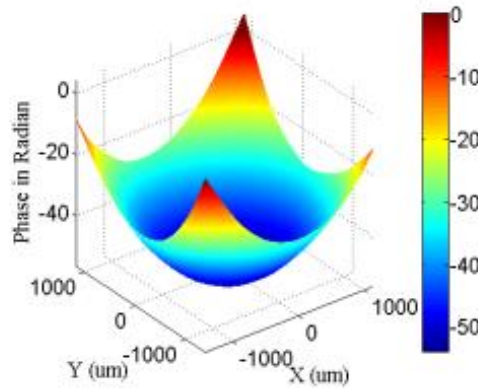
Figure 4.4 (a) Vectorial sheared fringe pattern, (b) Fourier transform of fringe pattern.

Further, proper phase unwrapping algorithm is performed to get the phase gradient information without 2π jumps. Fig. 4.5(a) and 4.5(b) shows the calculated phase gradient information along x and y directions respectively when the collimating lens is shifted by an amount of 3mm from the initial position. We use two-dimensional trapezoidal numerical integration method to integrate these x and y gradient that will reconstruct the complete wavefront $W(x,y)$. Since we are doing relative gradient measurement, the constant of integration will not affect the results much. Fig. 4.5(c) shows the reconstructed wavefront from obtained phase gradients. The same process is repeated for recorded interferograms at different positions of collimating lens L ($dr=0.5\text{mm}$, 1.0mm , 1.5mm , 2.0mm , and 2.5mm) from the initial position. Then lens L is moved back to its initial collimation position with same step size ($dr=2.0\text{mm}$, 1.5mm , 1.0mm , 0.5mm and final collimation state).



(a)

(b)



(c)

Figure 4.5 (a) Gradient along X-direction, (b) Gradient along Y-direction (c) Reconstructed Wavefront.

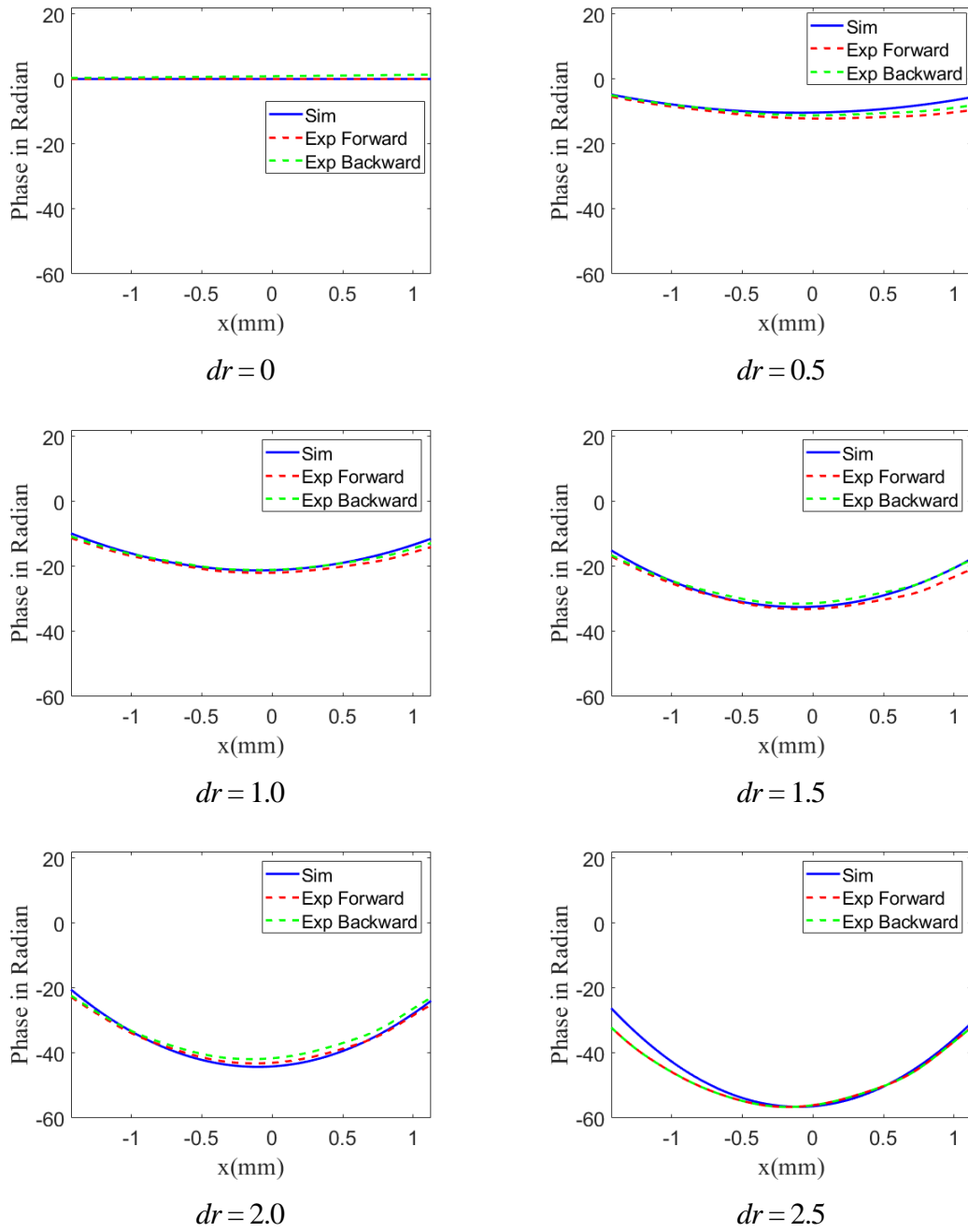
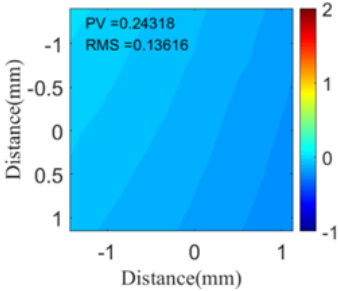
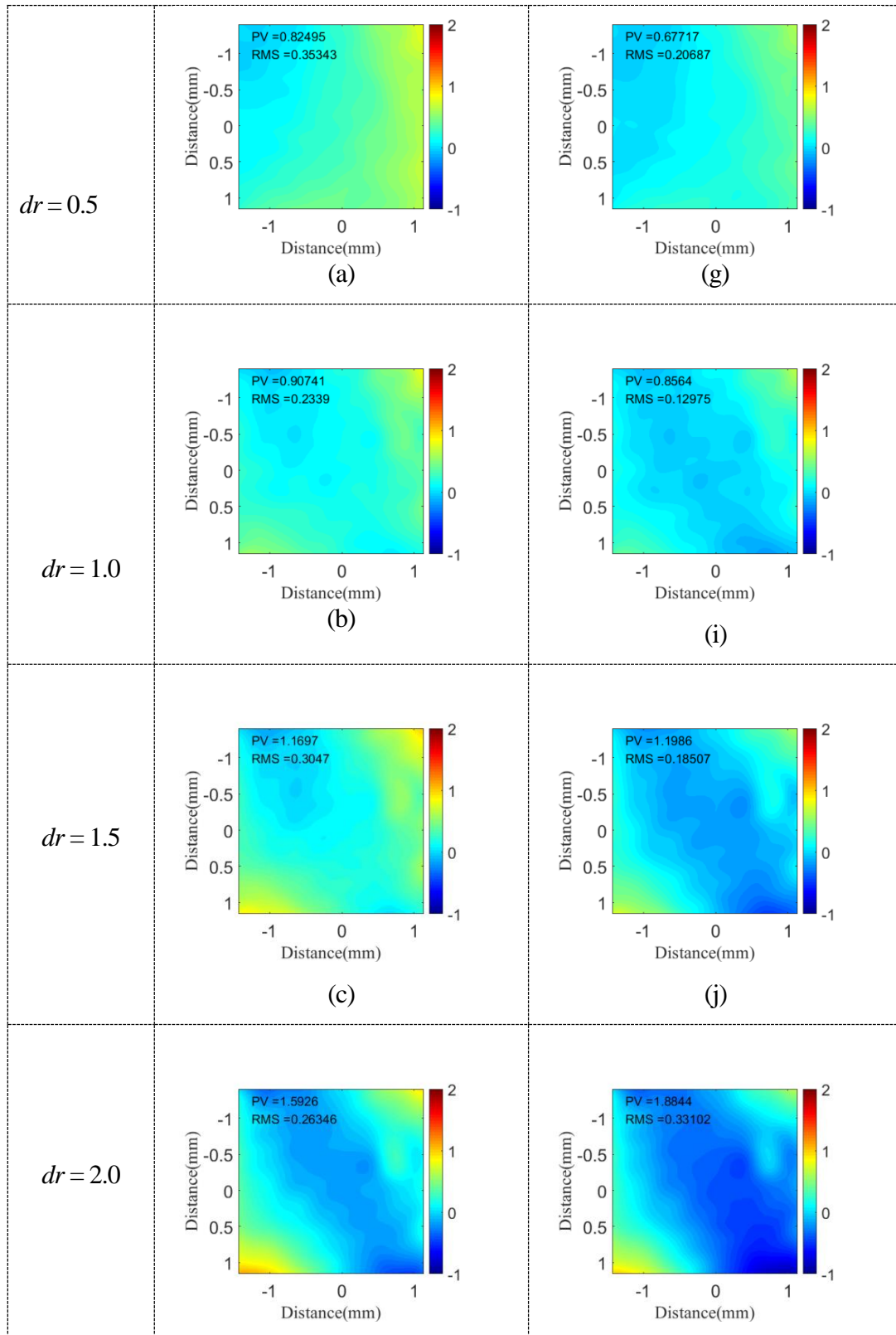


Figure 4.6 Shows the horizontal line profile ($y=0$) of reconstructed wavefront at different positions of collimating lens along z -direction with step size of 0.5mm. Red and green coloured dashed lines show experimental results and blue coloured line shows simulation results.

Using the parameters used for the experiment, a numerical simulation was performed using MATLAB software for wavefront reconstruction by using phase gradients obtained by orthogonal shearing of wavefront with different position of collimating lens as done in experiment. Fig. 4.6 shows the experimental (Red and Green dashed line) and simulation (Blue line) results. Red dashed line represents the wavefront reconstructed when lens moved forward along z -direction with step size of 0.5mm. Green dashed line represents the wavefront when lens moved in backward direction. The matching results confirm the accurate and stable wavefront reconstruction achieved using the scheme. From the results shown in Fig. 4.6, a deviation in wavefront shows a gradually increasing/decreasing tilt. This can be attributed to the in-plane mechanical movement of lens mount when the collimating lens is shifted in z -direction.

Lens L position (mm)	Deviations from reference/simulated wavefront during	
	Forward motion of Lens L from $dr = 0\text{mm}$ to 2.5mm	Backward motion (return) of Lens L from $dr = 2.5\text{mm}$ to 0mm
$dr = 0$		 <p>(f)</p>



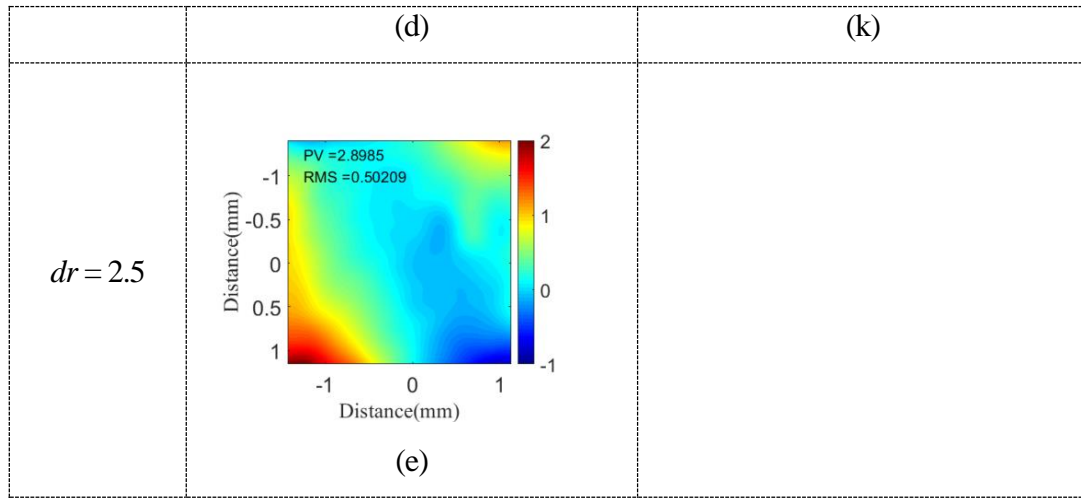


Figure 4.7 (a), (b), (c), (d) and (e) shows the wavefront deviations when collimating lens moves in forward direction. Figure (f), (g), (h), (i) and (j) shows the wavefront deviations when collimating lens moves in backward direction.

Experimental results of calculated wavefronts at different positions of collimating lens are compared with MATLAB simulated results and the error images are shown in Fig. 4.6 (a)-(k). The colour bar in images shows the value in term of wavelength (λ). For each wavefront Peak to Valley (PV) and root mean square (RMS) values are calculated and these values are shown in Table 4.1.

Position of collimating lens L (mm)	When lens moved forward along z-direction		When lens brought back to initial position	
	PV(λ)	RMS (λ)	PV (λ)	RMS (λ)
0.0	---	---	0.2432	0.1362
0.5	0.8250	0.3534	0.6772	0.2069
1.0	0.9074	0.2339	0.8564	0.1298
1.5	1.1697	0.3047	1.1986	0.1851
2.0	1.5926	0.2635	1.8844	0.3310

2.5	2.8985	0.5021	---	---
-----	--------	--------	-----	-----

Table 4.1 Shows PV and RMS values of calculated wavefront at different position of collimating lens L.

The laser beam was collimated when lens L positioned at distance $f=100\text{mm}$ from the pin hole of spatial filter assembly ($dr=0$). This condition was considered as reference for above experiment. When lens L is moved, the change in wavefront should match with simulated wavefront. But as table 4.1 shows PV and RMS values are increasing as the lens L is moved in forward direction. It is also observed that when lens L is moved back towards collimation position, PV and RMS values are not matching with that of forward direction at same position. This error may be result of inline mechanical moment of lens which might introduce tip and tilt to wavefront. Even when lens L reaches the initial collimation position, there is error present in calculated wavefront. Thus these types of wavefront errors can also be detected with Vectorial sheared cascaded Sagnac wavefront sensor.

4.5 Summary

The principle and experimental results of a wavefront sensor using Vectorial shearing interferometer (common path interferometer) and a telecentric lens system has been demonstrated. The amount of spatial carrier frequency for multiplexing the shearing interferogram can be fixed by introducing controlled mirror alignments of cascaded Sagnac interferometer. The lateral shear can be varied by moving the detector plane alone along z direction. Wavefront gradient along two perpendicular directions are computed simultaneously. By changing the position of collimation lens it is shown that mechanical errors inducing wavefront deviations of the order of fraction of wavelength can be detected using the proposed scheme. The near common-path geometry makes it stable in vibration sensitive environment allowing one to choose only the wavefront deviations of an aberrated light beam.

Chapter 5

Features of cascaded Sagnac based vectorial shearing interferometer for wavefront sensing

5.1 Introduction

Wavefront sensor is very important device in adaptive optics system as it gives the phase information and aberration introduced due to atmospheric turbulence. There are various types of wavefront techniques available but most commonly used techniques involve the transport of phase information in the intensity recorded using diffraction, refraction and interferometry. The wavefront sensors that work on the principle of intensity transport such as micro-lens (refraction) and grating (diffraction) seemed to be easily designed and handled as compared to the interferometric wavefront sensors where the phase gradients are detected from the resulting intensity redistribution. In this sense, it is important to bring out the features of the proposed interferometric wavefront sensor that sets it apart from the rest of the sensors. Shack Hartmann wavefront sensor is an example of refraction based wavefront sensor. Its working principle is explained in Appendix-B. The input wavefront is sampled into small sub-aperture regions using micro-lenslet arrays. The slope or tilt in sub-aperture region is calculated from shift in the centroid point as shown in Appendix-B. This device is simple and portable.

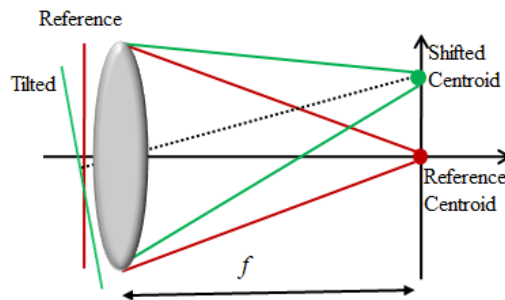


Figure 5.1 Shift in centroid from lens of SHWFS.

Optical shearing interferometer based WFS, is an example of interferometric wavefront sensor which has an inherent advantage that it does not require separate reference optical field. They are good choices for wave front sensing. The quantity that can be measured using Shearing interferometers is the phase gradients of the optical field. The scalar interferometers like lateral, radial and rotational shear interferometers are normally used to measure the phase gradients. Fig. 5.2 (a) and (b) explains the lateral and radial shearing techniques. The information measured using either of them can give gradients along only single coordinate direction (x/y/radial/azimuthal).

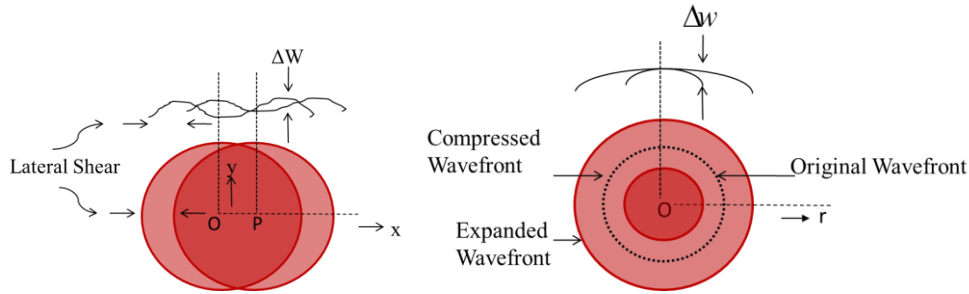


Figure 5.2 shows (a) lateral shearing beams, (b) radial y shearing beams.

For the complete 2-D wavefront reconstruction, especially for wavefronts lacking symmetry in Cartesian/polar coordinates, the gradients along both orthogonal coordinates (x and y or radial and azimuthal) has to be measured. So if the beams are sheared along two orthogonal directions as shown in Fig. 5.3, the gradients along x and y directions can be measured.

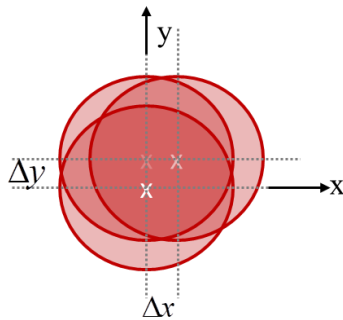


Figure 5.3 shows three beam shearing along x and y directions.

The shearing along two orthogonal directions can be done using Michelson or Mach-Zehnder interferometer but it will be two-step process. Such interferometers cannot be used for adaptive optics corrections for telescopic imaging under strong atmospheric turbulence, or for microscopic imaging under scattering media because conditions can change for two recorded interferograms. Hence, three wave lateral shearing interferometer is very important. It uses a predesigned diffractive optical element (DoE) or cascaded Sagnac Interferometer for generating 3 copies of the incoming wavefront to encode the vector gradients in the interference pattern in a single shot. Though there are many wavefront sensing schemes are available However most commonly used are Shack Hartmann Wave Front Sensor(SHWFS) and diffractive optics based wavefronts sensors. The work in this chapter will include a comparison of cascaded Sagnac Vectorial shearing interferometer (VSI)based wavefront sensing and Shack Hartmann Wave Front Sensing.

5.2 Experimental comparison of VSI and SHWFS

An experiment is performed in which the wavefront detection is carried out using a Shack-Hartmann Wavefront Sensor (SHWFS) and cascaded Sagnac Vectorial Shearing Interferometer simultaneously. The experimental set-up is shown in Fig. 5.4

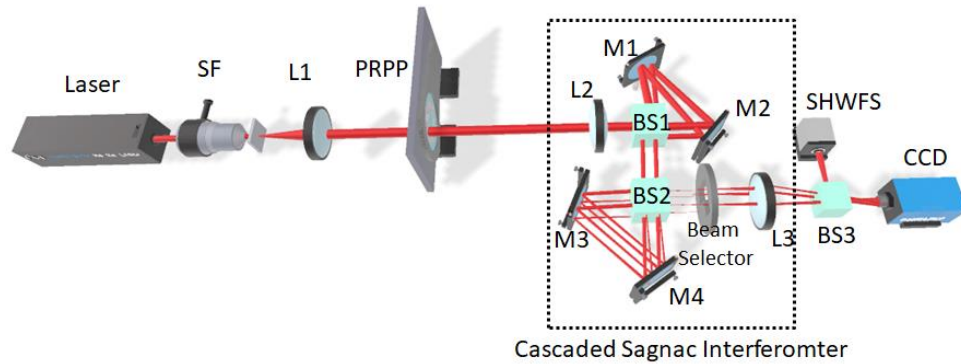


Figure 5.4 shows experimental set-up for wavefront sensing using SHWFS and cascaded sagnac VSI

A He-Ne laser of wavelength of 633nm is used as a source. The output of laser is spatially filtered and collimated using spatial filtering assembly (Microscopic objective and pin hole) and using a collimating lens (L).

The experiment is divided into two parts:

1. Measurement of curvature introduced due to motion of collimating lens.
2. Measurement of turbulence impacted wavefront.

5.2.1 Measurement of curvature

The collimated beam is fed to cascaded sagnac VSI as shown in Fig. 5.4. It consists of telecentric geometry (lens L1 and L2) and two sagnac interferometers (Mirrors M1, M2, M3 and M4, Beam splitters BS1 and BS2). Two sagnac interferometers are used to make four copies of input beam. By using beam selector three out of four beams are selected. Telecentric geometry is used to image the input on CCD and SHWFS simultaneously. The SHWFS used in this experimental set up consists of 31x31micro lens array, with 150 μm pitch of micro lens array and each microlens having an effective focal length of 3.5mm. The sensor in SHWFS is having 1024x1024 pixels, with each pixel is of size 4.6 μm . The CCD sensor used in Vectorial Shearing Interferometer is having 1040x1392 pixels, with each pixel is of size 6.4 μm .

First, in this experiment the collimating lens L is moved along z-direction with each step size of 0.25mm. The intensity recorded using SHWFS is shown in Fig. 5.5 (a), and the centroid shifts along x and y directions respectively. The gradient along x and y directions can be calculated from centroid shift data as shown in Fig. 5.5(b) and (c).

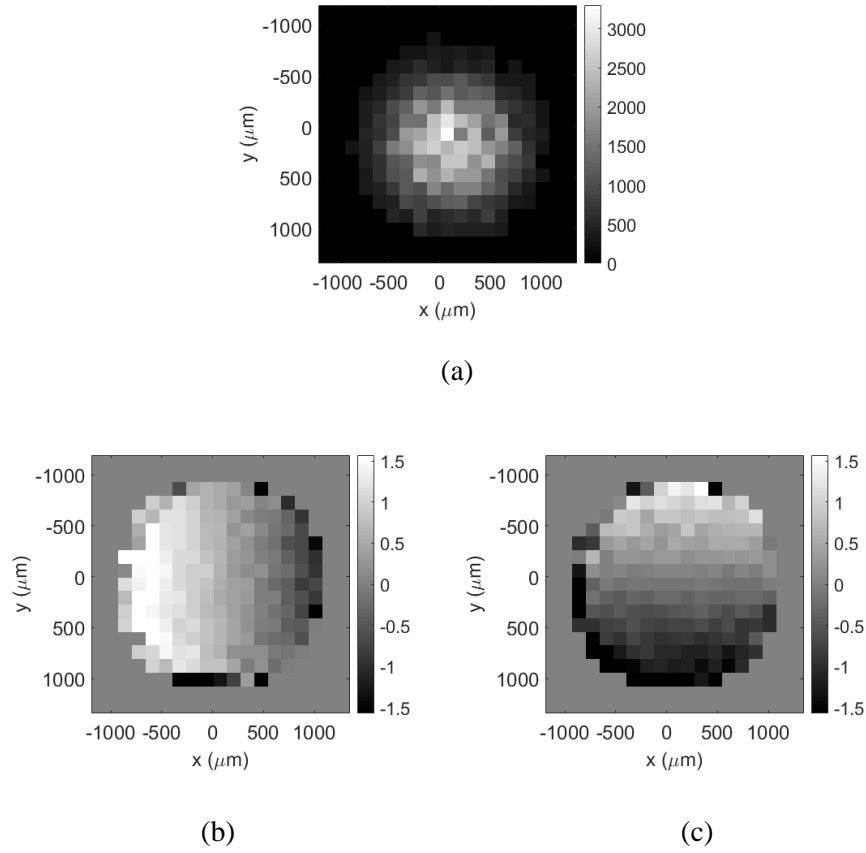
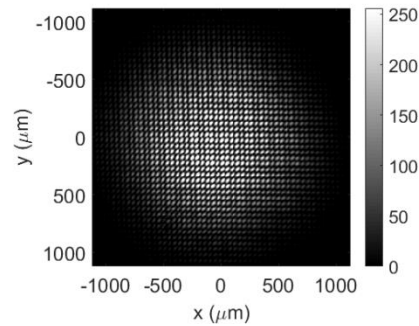


Figure 5.5 shows (a) Intensity recorded using SHWFS, (b) Gradient along x-direction, and (c) Gradient along y-direction.

The two dimensional sheared beam interferogram (three wave shearing) recorded using VSI is shown in Fig. 5.6(a). After applying Fourier transform fringe analysis process, the wavefront gradients along x and y directions are obtained and the results are shown in Fig. 5.6 (b) and (c) respectively.



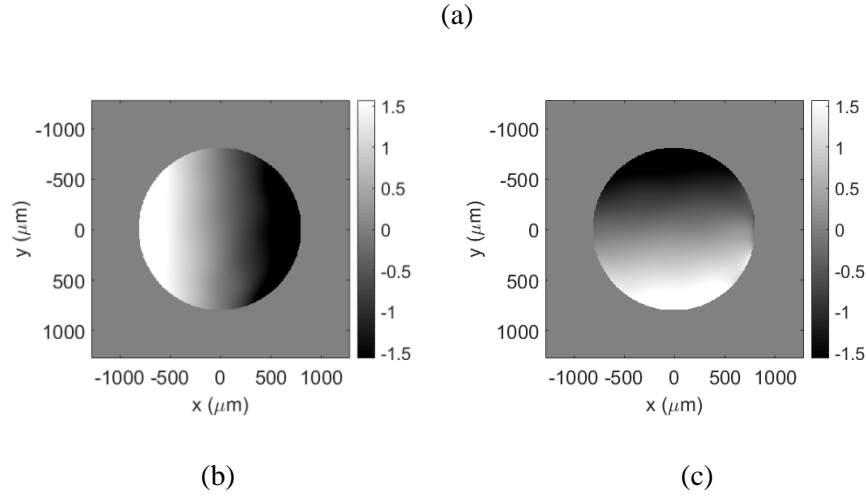


Figure 5.6 shows (a) Recorded interferogram using VSI, (b) gradient along x direction and (c) gradient along y direction.

The wavefronts are reconstructed from gradients information retrieved from SHWFS and cascaded Sagnac VSI by applying two dimensional numerical integration methods. The reconstructed wavefront at different positions of collimating lens ($dz=0\text{mm}$, 0.25mm , 0.5mm , 0.75mm , 1.00mm and 1.25mm) for SHWFS data are shown in Fig. 5.7.

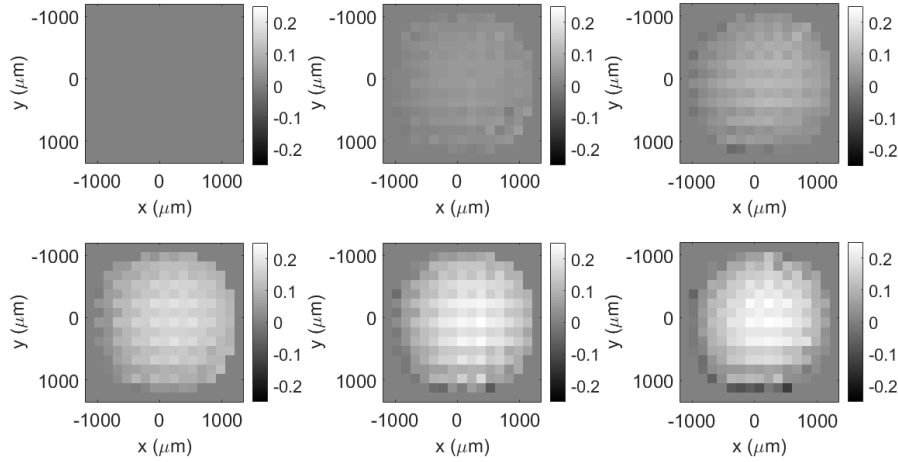


Figure 5.7 shows reconstructed wavefront for SHWFS data at different position of collimating lens L .

The reconstructed wavefront at different positions of collimating lens ($dz=0\text{mm}$, 0.25mm , 0.5mm , 0.75mm , 1.00mm and 1.25mm) for cascaded Sagnac VSI data are shown in Fig. 5.8.

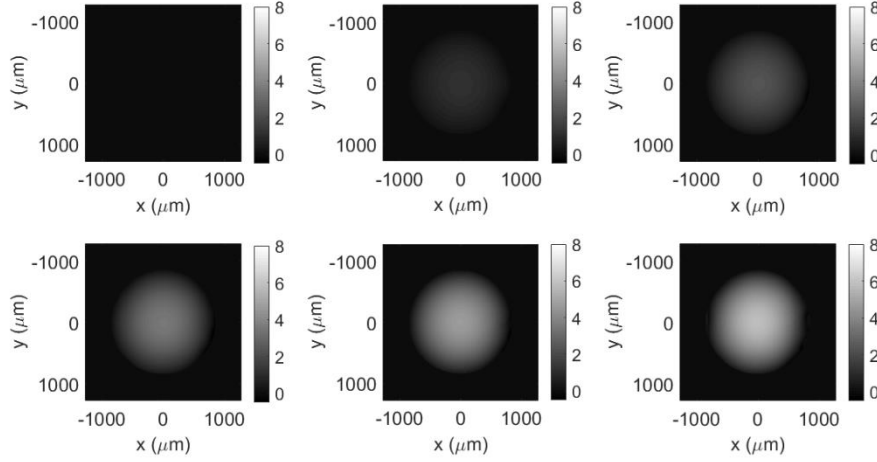


Figure 5.8 shows reconstructed wavefront for cascaded sagnac data at different position of collimating lens L.

The curvatures introduced due to motion of collimating lens are detected from both SHWFS and VSI. The results show that the reconstructed wavefront is sharper in Sganac Vectorial Shearing Interferometer compared to SHWFS. The least square algorithm, southwell and other curve fitting algorithms are used to get back the reconstructed wavefront from the SHWFS data However in case of Sagnac Vectorial Shearing Interferometer, no such algorithms are required.

5.2.2 Measurement of turbulence affected wavefront

Using same experimental set up shown in Fig. 5.4, the pseudo random phase plate (PRPP) mimicking atmospheric turbulence is introduced after collimating lens. The PRPP is positioned in such a way that it is imaged on to CCD of VSI and SHWFS. The details of PRPP is given in Appendix-I. The beam diameter used is about 5mm but due to telecentric geometry ($f_1=500\text{mm}$ and $f_2=200\text{mm}$) it reduces to about 2mm. The r_0 (Fried parameter) value for the PRPP is $640\text{ }\mu\text{m}$ and if the beam size is bigger than r_0 , then higher order aberration will be present in the beam. The images obtained are captured on sensor of SHWFS with and without introducing PRPP and they are

shown in Fig. 5.9. When PRPP is inserted, the intensity variations obtained using Shack Hartmann Wavefront Sensor before and after inserting PRPP are shown in Fig. 5.9(a) and 5.9(b) respectively. But, it can be seen that the spot shifts obtained after inserting PRPP shown in Fig.5.9(b) is very difficult to detect. Now, the data is recorded for different spatial positions on PRPP and processed.

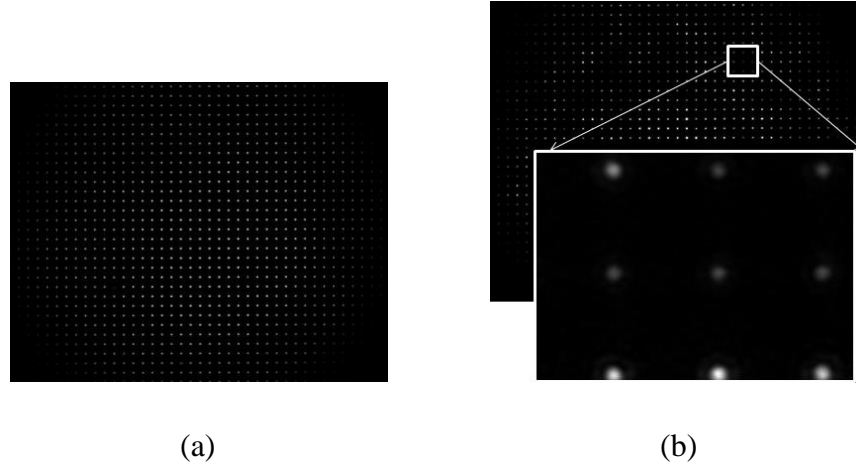


Figure 5.9 shows (a) Image on sensor of SHWFS with plane wave(Without PRPP) as input, (b) image on sensor of SHWFS after inserting PRPP.

The reconstructed wavefront results for SHWFS data is shown in Fig. 5.10. It can be seen that the resolution of the reconstructed wavefront is very poor.

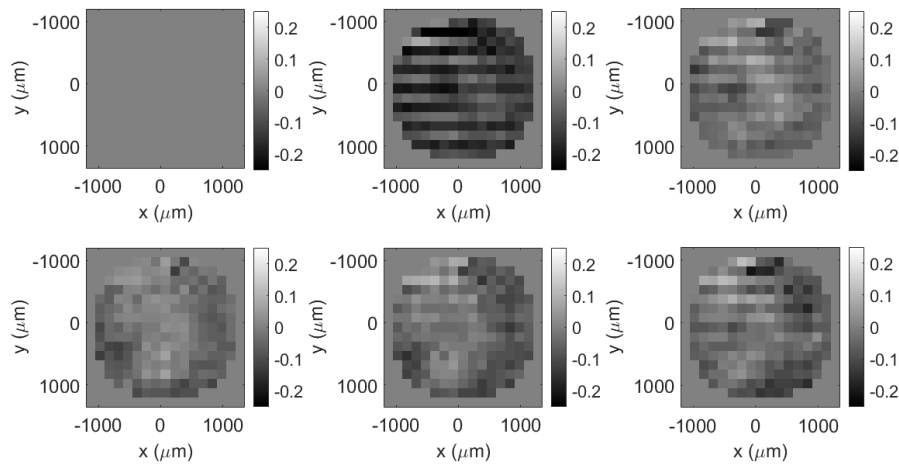


Figure 5.10 The reconstructed wavefront results for SHWFS data after inserting PRPP.

The experiment is repeated in Sagnac Vectorial Shearing Interferometer and the results are shown in Fig. 5.11. Fig.5.11 shows the reconstructed wavefront results for cascaded sagnac VSI with and without inserting PRPP. It can be seen that the resolution obtained for the reconstructed wavefront is far better than that of SHWFS. This shows that under severe turbulent conditions the cascaded Sagnac Vectorial Shearing Interferometer can give better results compared to SHWFS.

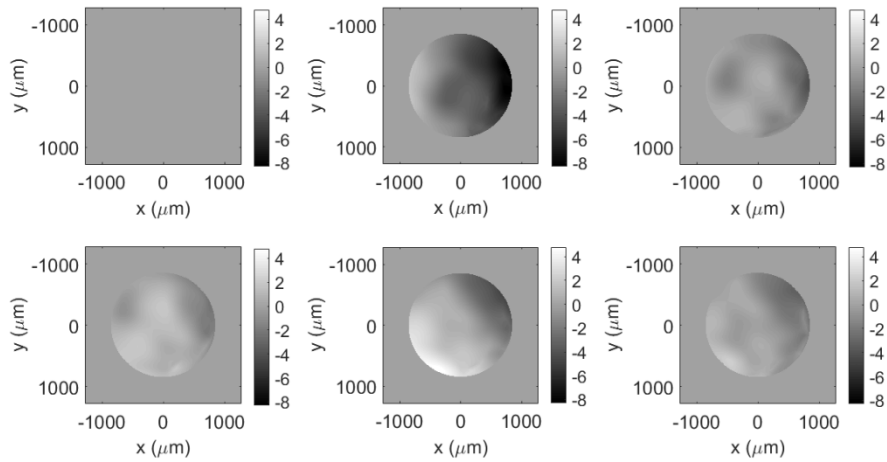


Figure 5.11 The reconstructed wavefront results for cascaded Sagnac VSI data after inserting PRPP.

5.3 Merits of cascaded Sagnac vectorial shearing interferometer

1) The design of cascaded Sagnac VSI is such that all the three wavefronts nearly pass through the common path, encountering every element of the system, so that the system induced error does not reflect in the relative phase measurement. Moreover, the common-path geometry will ensure that no dynamically varying phase difference gets introduced between the interfering copies of wavefront.

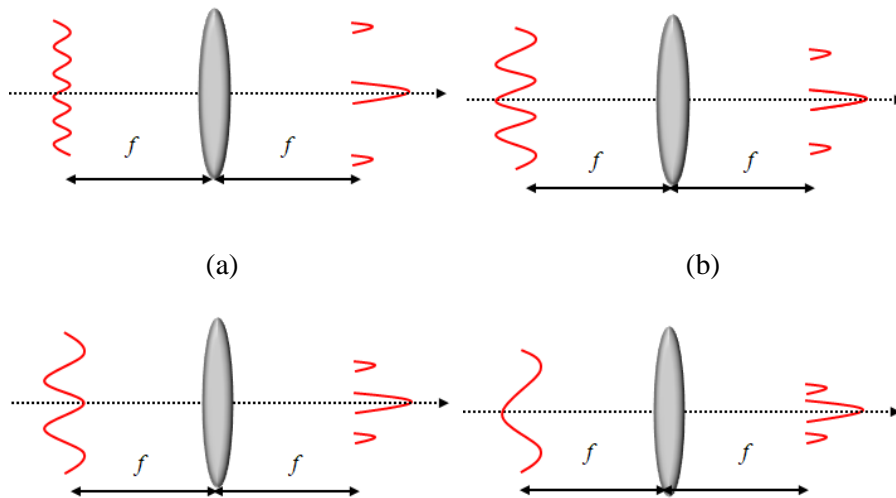
2) In VSI, using a pair of cascaded Sagnac interferometer allows spatial frequency multiplexing in the interferogram in order to detect the vector gradients simultaneously and independently. The spatial carrier frequencies can be increased or

decreased by controlling tilt from mirrors of Sagnac interferometers. On the other hand, in all other wavefront sensing techniques, the spatial carrier frequency is fixed as there is no option for controlling the tilt.

3) The SHFWS samples the wavefront using sub aperture regions equal to the size of a micro lens. So the information recorded is limited by size of sub aperture lens. In cascaded Sagnac VSI, the interferogram is recorded upto pixel size of sensor. As fringe width can be controlled, minimum two pixels will be required to resolve one fringe.

4) In cascaded Sagnac wavefront sensor the phase information is calculated independent of intensity. Any amplitude variation for the optical field will only result in reduction in fringe visibility for the recorded interferogram. The fringe modulation depends only on the phase distribution of the optical field. As long as there exists a detectable amount of fringe visibility, the phase gradient can be measured. In case of SHWFS the centroid of the spot focused by the lenes in a micro;lens array is dependent not only on the phase distribution, but also on the intensity distribution across the sub-aperture.

5) In high turbulence condition, the phase variation will be much higher to be detected by single micro lens.



(c)

(d)

Figure 5.12 when different modes are input to a lens.

This is because, the lens act as a Fourier transforming element. It can be seen from Fig. 5.12 (a-d), that even the smaller amplitude modulation in the input will result in spread of the focal spot in Fourier plane, the detector plane in SHWFS.

5.4 Limitation of cascaded Sagnac VSI

- 1) Every device has some limitations so as cascaded Sagnac VSI. It has low efficiency as it uses only ~19 % of the input light. In this case SHWFS is highly efficient as it uses maximum input light. In three wave shearing based on grating also has low efficiency as it uses three first order copies of diffracted beam.
- 2) Cascaded Sagnac VSI wavefront sensor looks little complicated compared to SHWFS and grating based three wave SI. However it can be made compact with proper designing technique.

5.5 Summary

In this chapter, a comparative analysis of SHWFS and cascaded Sagnac VSI is carried out. Experimentally it is observed that SHWFS resolution is limited by sub-aperture size of micro lens array whereas cascaded Sagnac VSI resolution depends on the minimum pixels of sensor required to solve one fringe. Wavefront reconstruction for VSI is better than SHWFS as no special curve fitting algorithms are required in VSI. The experimental results of wavefront reconstruction for a turbulent impacted (when beam passes through PRPP) beam shows that under high turbulence condition cascaded Sagnac VSI senses the wavefront better than SHWFS.

Chapter 6

Wavefront sensing using low-coherent sources through spatial coherence revival

6.1 Introduction

An interferometry based wavefront sensing scheme applicable to low-coherent light sources like LED (Light Emitting Diode) is demonstrated in this chapter. In adaptive optics, it requires a guided star (laser beacon) in the vicinity of the object being imaged to correct the turbulence induced aberrations. A guide star used in adaptive optics need not be always a coherent light source. Keeping this aspect in mind, we test the potential of cascaded Sagnac Vectorial shearing interferometer in sensing the wavefront aberrations in optical field originating from a light source with limited spatial and temporal coherence. To simulate this situation, a light emitting diode as the source of light is chosen. The generation of copies of wavefront using simple reflection instead of diffraction is implemented. The distortions in the wavefront of this light source, acquired when passing through the turbulent medium, is sensed to correct the imaging optics.

Using a pair of cascaded Sagnac interferometers, spatial frequency multiplexed interference of three sheared copies of the wavefront is recorded and the independent vector gradients obtained from this, are used to reconstruct the wavefront as done in chapter 4. The problem for detection of LED like sources wavefront with interferometry is its low spatial and temporal coherence. J. Primot et al has shown detection of low coherent front using diffractive optical techniques [36]. In this work three challenges were:

i) If three copies of a wavefront are made using simple reflections rather than diffraction, the shear becomes independent of the wavelength [Appendix C]. However, this implies that the phase gradients will become wavelength sensitive.

ii) In addition, the spatial carrier fringe introduced in the interference between the wavefront copies in this case, becomes wavelength dependent leading to possible degradation in the fringe contrast at the periphery of the interference pattern.

iii) Finally, the requirement of a finite amount of lateral shear demands the light source to be spatially coherent so that the interference fringes can be visualized.

To overcome the first two challenges without resolving the spectrum, we take a leaf out of white light interferometry. For a light source with a Gaussian spectrum, it has been shown that the phase can be calculated for the central wavelength [95]. With sufficient amount of temporal coherence length and the use of high dynamic range for the intensity detector allows introduction of high spatial carrier fringe with sufficient visibility at the periphery of the interferogram. The wavefront sensing using low-coherent/extended light sources is challenging as the spatial coherence of the propagating optical field is modulated by the structure of the light source. Deriving a point-like light source from an extended source is not recommended considering the light through-put requirements. By suitably modulating the light source intensity distribution using Multi Incoherent Source Talbot Interferometer (MISTI), it has been shown that the wavefront can be sensed in the case of extreme UV low brightness source [40]. For a field propagated from an extended incoherent source, the spatial coherence dies out as a function of increasing correlation length (lateral shear). To overcome the limitation of spatial coherence introduced by a finite spatial extension of an incoherent light source, we propose to utilize the diffraction effect of spatial coherence. Using, Van Cittert Zernike theorem, it can be shown that by spatially modulating the incoherent source distribution, the spatial coherence function can be revived for specific values of lateral shear [96-97]. In the literature, the term coherence revival is generally used to describe the enhancement of temporal coherence through modulation of temporal frequency spectrum [97]. In this experiment, we adopt it to describe the partial enhancement of spatial coherence and demonstrate it by introducing a hard aperture at the source plane that leads to spatial coherence having Bessel distribution with extended side lobes. By setting the lateral

shear corresponding to one of the maxima of these side lobes, fringe visibility in the interferogram is maintained at the detectable level. In this way the coherence limitations in the interference of copies of the wavefront derived merely through reflections are resolved. The meaning of the term ‘revival’ is betterment.

6.2 Principle behind low coherence wavefront sensing

Low coherence wavefront sensing needs stability against external vibrations and that we could avoid due to design of a cascaded Sagnac interferometer. The Sagnac interferometer generates three copies of wavefront and allows spatial frequency multiplexing in the interferogram in order to detect the vector gradients simultaneously and independently. By simultaneous extraction of vector gradients using Fourier transform method of fringe analysis followed by a two-dimensional numerical integration method, the complete wavefront $W(x,y)$ is reconstructed. The conceptual diagram for common-path vectorial shearing wavefront sensor using low coherent LED is shown in Fig.6.1. The system is a combination of a pair of cascaded Sagnac interferometers (shown in Fig.6.2) and a 4-f telescopic system with two lenses of focal length f_1 and f_2 respectively. O is the object plane which is at z_1 distance from plane A i.e. focal plane of lens L_1 . The combination of lens L_1 and vectorial shearing interferometer will generate four copies of the input wavefront at plane F which will be equally separated along X and Y directions as shown in Fig.6.1. Plane B is the back focal plane of the lens L_2 where all four wavefront copies will overlap on each other. Plane I is the shearing plane at which wavefront can be sheared along two perpendicular directions simultaneously. Plane I is at z_2 distance from back focal plane of lens L_2 .

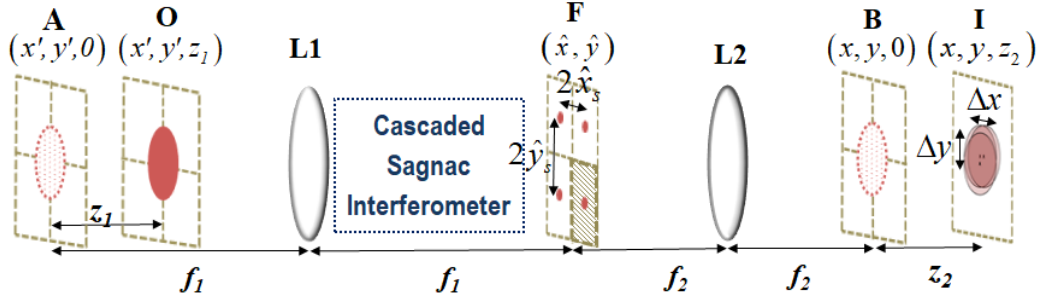


Figure 6.1. Conceptual diagram for common-path VSI

Let $u_o(x', y', \nu)$ be the field at object plane O corresponding to a monochromatic light component having frequency $\nu = c/\lambda$, where c is the velocity of the light and λ is the wavelength. The field at plane I can be written as:

$$\begin{aligned}
 u_{I,n}(x, y, \nu) = & -\exp\left(i \frac{2\pi z_2}{\lambda} \left(1 - \frac{f_1^2}{f_2^2} + \frac{\hat{x}_s^2 + \hat{y}_s^2}{2f_2^2}\right)\right) \\
 & \times \exp\left(-i \frac{2\pi}{\lambda f_2} (x\hat{x}_s + y\hat{y}_s)\right) \\
 & \times u_o\left(\frac{-1}{m} \left(x + \frac{\hat{x}_s z_2}{f_2}\right), \frac{-1}{m} \left(y + \frac{\hat{y}_s z_2}{f_2}\right), \nu\right)
 \end{aligned} \tag{6.1}$$

The above equation representing field can be divided into three parts.

- The first part shows a constant phase depending on the focal lengths of lenses L_1 and L_2 respectively at a shearing plane distance z_2 from plane B (the back focal plane of lens L_2).
- Second part shows the presence of a linear phase which is a function of focal length of lens L_2 , with the separation introduced at the output of the cascaded Sagnac interferometer along \hat{x} and \hat{y} directions having magnitude \hat{x}_s and \hat{y}_s respectively.

- The third part of Equation shows the complex field of wavefront at plane O which is inverted and scaled by factor of $m = f_2/f_1$ and shifted by $\Delta x = \hat{x}_s z_2/f_2$ along x -direction and by $\Delta y = \hat{y}_s z_2/f_2$ along y -direction respectively with $n = 1, 2$ and 3 representing the three copies of the wavefront. It should be noted here that the shift introduced is independent of the wavelength.

Let us consider a two-beam interference of $u_{I,1}(x, y, \nu)$ and $u_{I,2}(x, y, \nu)$ shifted by an amount $(\Delta x, \Delta y) = (\hat{x}_s z_2/f_2, \hat{y}_s z_2/f_2)$ and $(\Delta x, \Delta y) = (-\hat{x}_s z_2/f_2, \hat{y}_s z_2/f_2)$ respectively.

$$I_{1,2}(x, y, \nu) = |u_{I,1}(x, y, \nu)|^2 + |u_{I,2}(x, y, \nu)|^2 + \langle u_{I,1}^*(x, y, \nu) u_{I,2}(x, y, \nu) \rangle + \langle u_{I,1}(x, y, \nu) u_{I,2}^*(x, y, \nu) \rangle \quad (6.2)$$

From equation 6.1,

$$\begin{aligned} \langle u_{I,1}^*(x, y, \nu) u_{I,2}(x, y, \nu) \rangle &= \exp \left[\frac{2\pi i}{\lambda f_2} (2x \hat{x}_s) \right] \left\langle u_o^* \left(\frac{-1}{m} (x + \Delta x), \frac{-1}{m} (y + \Delta y), \nu \right) \right. \\ &\quad \left. \times u_o \left(\frac{-1}{m} (x + \Delta x), \frac{-1}{m} (y - \Delta y), \nu \right) \right\rangle \end{aligned} \quad (6.3)$$

For a polychromatic light having a Gaussian spectral distribution given by

$$|S(\nu)|^2 = G \exp \left[- \left(\frac{\nu - \bar{\nu}}{\Delta \nu} \right)^2 \right], \quad (6.4)$$

Where G is a constant depending on the mean power, $\bar{\nu}$ is the central frequency and $\Delta \nu$ is the spectral width.

The total field can be written as [95]:

$$u_o(x, y, \nu) = S(\nu) u_o(x, y)$$

(6.5)

Considering that the spatial distribution of the field components are independent of the spectrum $u_o(x, y, \nu)$

$$\begin{aligned} \langle u_{I,1}^*(x, y) u_{I,2}(x, y) \rangle &= \left\langle u_o^* \left(\frac{-1}{m}(x + \Delta x), \frac{-1}{m}(y + \Delta y) \right) u_o \left(\frac{-1}{m}(x + \Delta x), \frac{-1}{m}(y - \Delta y) \right) \right\rangle \\ &\quad \times \int |S(\nu)|^2 \exp \left[\frac{2\pi i}{\lambda f_2} (2y \hat{y}_s) \right] d\nu \end{aligned} \quad (6.6)$$

Substituting the value of $|S(\nu)|^2$ in Eqn.6.6 and solving it.

$$\begin{aligned} \langle u_{I,1}^*(x, y) u_{I,2}(x, y) \rangle &= G\pi\Delta\nu \times \left\langle u_o^* \left(\frac{-1}{m}(x + \Delta x), \frac{-1}{m}(y + \Delta y) \right) u_o \left(\frac{-1}{m}(x + \Delta x), \frac{-1}{m}(y - \Delta y) \right) \right\rangle \\ &\quad \times \exp \left(- \left(\frac{2\pi \hat{y}_s}{l_c f_2} y \right)^2 \right) \exp \left(-i \frac{4\pi \hat{y}_s}{\bar{\lambda}_c f_2} y \right) \end{aligned} \quad (6.7)$$

The term $\left\langle u_o^* \left(\frac{-1}{m}(x + \Delta x), \frac{-1}{m}(y + \Delta y) \right) u_o \left(\frac{-1}{m}(x + \Delta x), \frac{-1}{m}(y - \Delta y) \right) \right\rangle$ provides the phase gradient along y direction. $l_c = \bar{\lambda}_c^2 / \Delta\lambda$ denotes the temporal coherence length, $\bar{\lambda}$ denotes the central wavelength and $\Delta\lambda$ is the spectral bandwidth. The term $\exp \left(-i \frac{4\pi \hat{y}_s}{\bar{\lambda}_c f_2} y \right)$ introduces the linear phase corresponding to the spatial carrier frequency $\hat{y}_s / \bar{\lambda}_c f_2$.

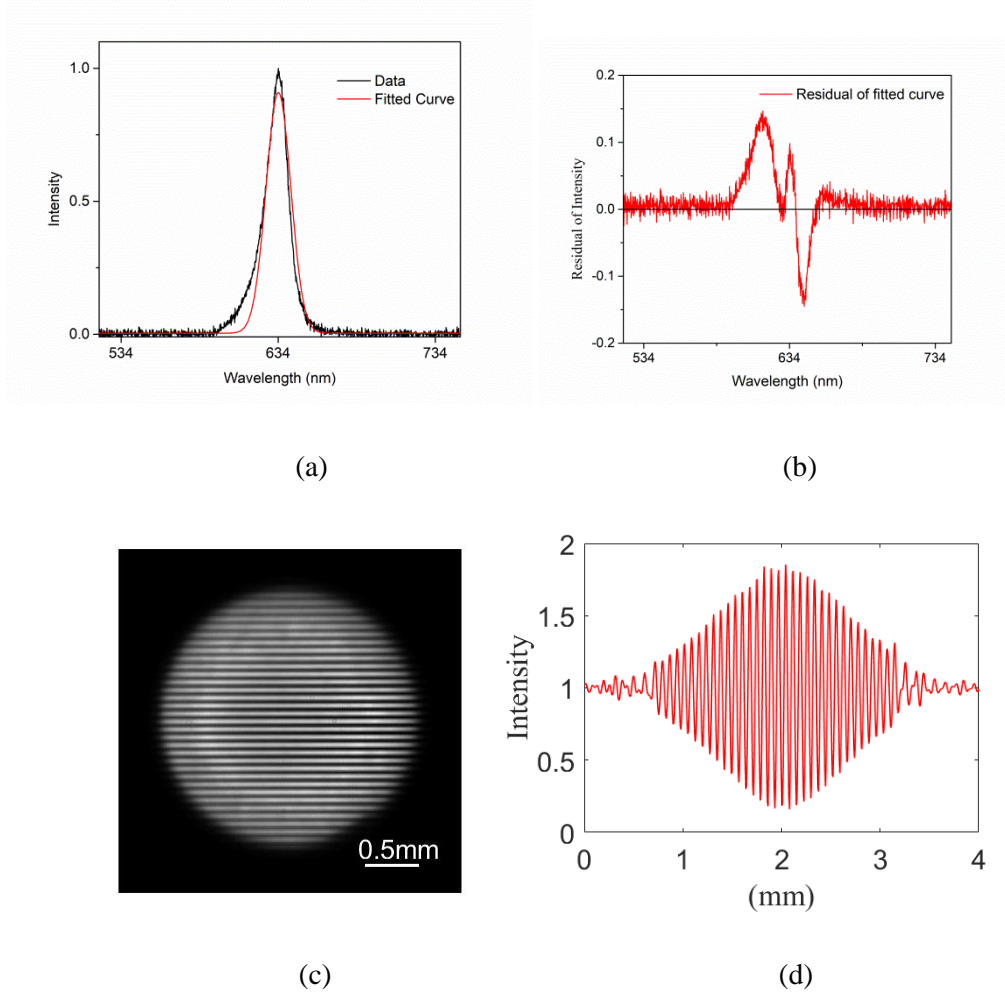


Figure 6.2 (a) Spectra of LED source. (b) Residual of intensity plot after curve fitting of LED spectra. (c) Fall of contrast for the spatial carrier fringes along y direction as explained by equation 6.14, (d) The intensity variation along the y direction after normalizing with the intensity distribution of the interfering beams.

The contrast of the fringes in the interferogram, decided by the strength of $\langle u_{I,1}^*(x, y) u_{I,2}(x, y) \rangle$, falls as a Gaussian along y. Spectra of the LED source used in experiment after curve fitting is shown in Fig.6.2 (a). Residual of intensity plot after curve fitting is shown in Fig. 6.2 (b). It is a nearly symmetric Gaussian distribution having central wavelength of $\sim 634 \text{ nm}$. Interferogram resulting from the superposition of $u_{I,1}(x, y)$ and $u_{I,2}(x, y)$ under complete overlapping condition ($z_2 =$

0) and with spatial carrier frequency introduced along y direction, is shown in Fig.6.2(c). The contrast of the fringes exhibits a Gaussian decay along y -direction. A detectable contrast at the periphery of the field of view can be maintained by suitable choice of the spatial carrier frequency. The intensity variation in the interferogram along the y direction after normalizing with the intensity distribution of the interfering beams is shown in Fig.6.2(d).

To understand the influence of limited spatial coherence provided by the light source, consider an extended, but quasi-monochromatic, incoherent source. At that source plane with (\tilde{x}, \tilde{y}) as the coordinates, we assume a delta function for the field correlation, as follows.

$$\langle u^*(\tilde{x}_1, \tilde{y}_1) u(\tilde{x}_2, \tilde{y}_2) \rangle = I(\tilde{x}_1, \tilde{y}_1) \delta(\tilde{x}_2 - \tilde{x}_1, \tilde{y}_2 - \tilde{y}_1) \quad (6.8)$$

The field correlation at its Fourier plane can be described using Van Cittert Zernike theorem:

$$\langle u_o^*(x_1, y_1) u_o(x_2, y_2) \rangle = \iint I(\tilde{x}, \tilde{y}) \exp \left[i \frac{2\pi}{\lambda f_1} ((x_2 - x_1)\tilde{x} + (y_2 - y_1)\tilde{y}) \right] d\tilde{x} d\tilde{y} \quad (6.9)$$

$$\begin{aligned} & \left\langle u_o^* \left(\frac{-1}{m}(x + \Delta x), \frac{-1}{m}(y + \Delta y) \right) u_o \left(\frac{-1}{m}(x + \Delta x), \frac{-1}{m}(y - \Delta y) \right) \right\rangle = \\ & \iint I(\tilde{x}, \tilde{y}) \exp \left[-i \frac{2\pi}{\lambda m f_1} (2\Delta y \tilde{y}) \right] d\tilde{x} d\tilde{y} \end{aligned} \quad (6.10)$$

By suitably choosing the source intensity distribution $I(\tilde{x}, \tilde{y})$, it is possible to maintain high correlation/coherence value corresponding to a particular value of the shear. This phenomena, generally termed as diffraction effect of spatial coherence function can be effectively utilized to revive the fringe contrast for certain specific

values of lateral shear. We choose a hard circular aperture for $I(\tilde{x}, \tilde{y})$ so that its Fourier Transform results in a Bessel function as described in Fig.6.3. The red curve describes the experimentally measured fringe contrast as a function of lateral shear whereas the blue curve describes the theoretical fit generated based on the experimental parameters. Had the field at the detector plane propagated from a single point source, the spatial coherence would have been high for any value of lateral shear. The contributions from other point sources due to finite spatial extent of the source results in the spatial coherence falling to zero within $100\mu m$ of lateral shear; effectively making it impossible to define a wavefront. We set the lateral shear value of $152\mu m$ matching with the maxima of the 1st side-lobe.

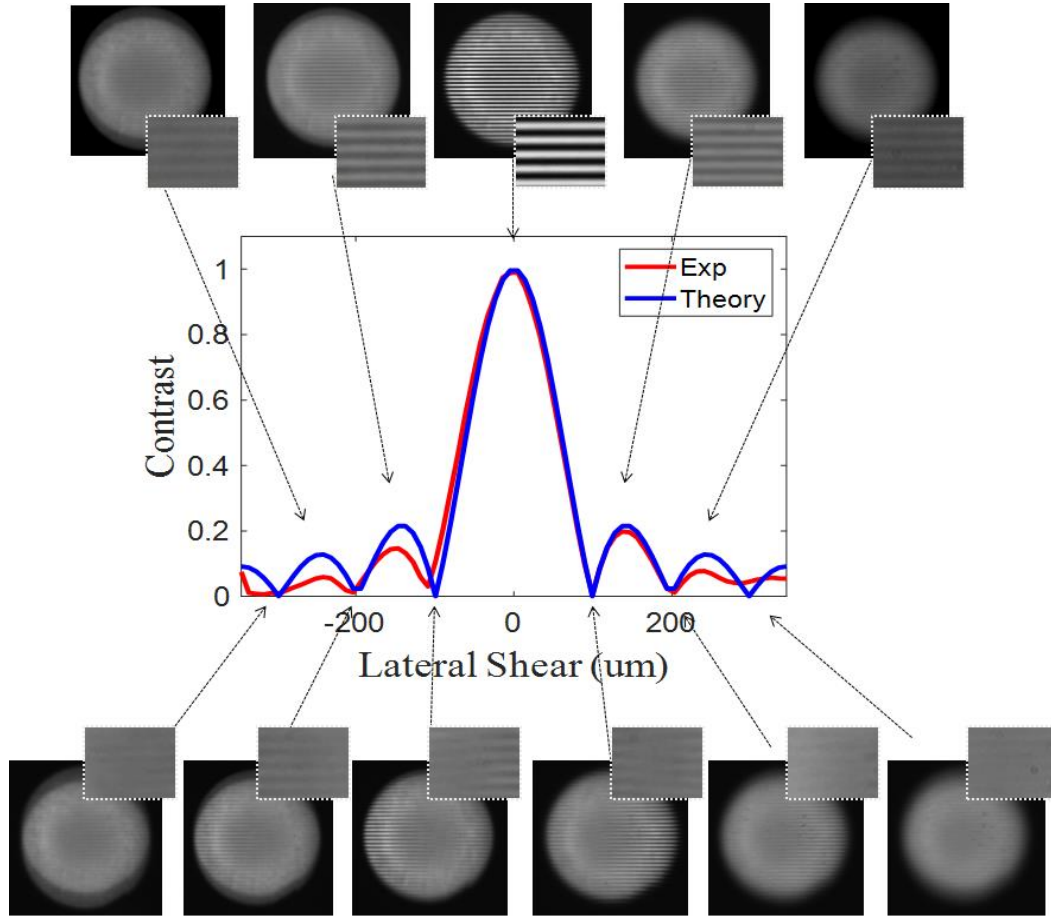


Figure 6.3 The diffraction effect in spatial coherence function, introduced by hard aperture, measured at the interferogram plane. Interferograms recorded at specific values of lateral shear are provided at the top and bottom rows. The central region of the interferogram is cropped and shown in the inset for better visualization of fringe contrast variations.

In a similar way, we can tune the spatial coherence to be high for the lateral shear provided along x direction as well.

The three orthogonally sheared wavefronts interfere at plane I and the resulting intensity is recorded by a CCD equal to,

$$I_I(x, y) = \left| u_{I,1}(x, y) + u_{I,2}(x, y) + u_{I,3}(x, y) \right|^2 \quad (6.11)$$

The terms representing the orthogonal shearing interference $\langle u_{I,1}^*(x, y)u_{I,2}(x, y) \rangle$ and $\langle u_{I,1}^*(x, y)u_{I,3}(x, y) \rangle$ are retrieved through Fourier transform method of fringe analysis [95][96]. The resulting phase gradients are used to reconstruct the wavefront.

6.3. Experimental Results and discussion

6.3.1 Validation of the scheme sensing quadratic wavefronts

The experimental set-up to validate the proposed vectorial shearing cascaded Sagnac interferometric wavefront sensor is shown in Fig. 6.4. In this set-up, a LED (Light Emitting Diode) having central wavelength $\sim 634 \text{ nm}$ and spectral bandwidth of $\sim 18 \text{ nm}$ as shown in Fig.2(a) is used as the low-coherent source. To revive the spatial coherence corresponding to the lateral shear introduced, a $50 \mu\text{m}$ diameter circular aperture is introduced at the LED plane and imaged using a 10x microscope objective (MO) at the front focal plane of lens L resulting in an equivalent hard aperture of 0.6 mm diameter, is introduced as shown in Fig. 6.4.

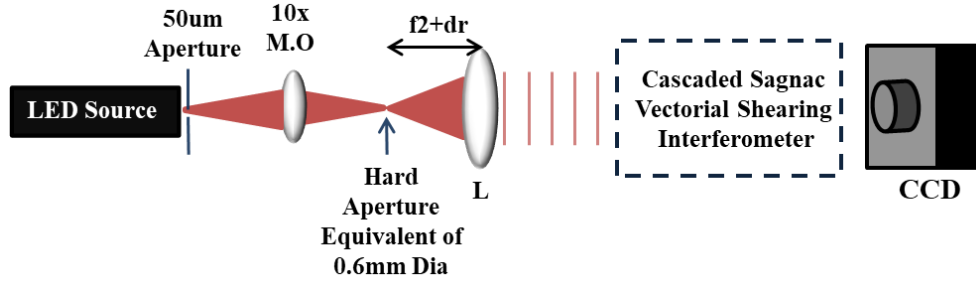


Figure 6.4 Wavefront sensing using vectorial shearing interferometer

The light collimated by lens L is fed as input to the vectorial shearing wavefront sensor. The beam coming out of vectorial shearing sensor is then falls on a CCD (Pixelfly, 1392x1040, pixel size $6.4 \mu\text{m}$). As the position of the collimating lens changes, the shape of the beam also changes. Depending upon the direction in which the lens is moved the beam output may be converging or diverging. First the collimating lens was moved in direction towards the VSWFS with increasing steps of

0.25 mm. Corresponding to each position of lens the interferogram is recorded. The interference of three sheared wavefronts is recorded as a single interferogram using spatial frequency multiplexing technique [96]. Demultiplexed phase gradients are obtained using Fourier transform method of fringe analysis [98-99]. Figure 6.5(a) shows the recorded interferogram showing the vectorially sheared fringe pattern and Fig.6.5(b) shows the 2D Fourier spectrum of the recorded interferogram with spatial frequencies f_x and f_y represented as $\hat{x}/\lambda f_2$ and $\hat{y}/\lambda f_2$. There are seven spots shown in Fig.6.5(b) in which the center one is the zeroth order term representing the dc-part in the recorded interferogram. The upper three spots show the mutual superposition of sheared wavefronts. They get separated due to the spatial carrier frequency $2\hat{x}_s/\lambda f_2$ and $2\hat{y}_s/\lambda f_2$ with $2\hat{x}_s = 3.037\text{mm}$ and $2\hat{y}_s = 2.90\text{ mm}$ introduced. The conjugate spots of upper three appear at the lower side. The circular regions with radius $230\mu\text{m}$ around $(\hat{x} = 2\hat{x}_s, \hat{y} = 0)$ and $(\hat{x} = 0, \hat{y} = 2\hat{y}_s)$ are individually selected and inverse Fourier transformed. From the inverse Fourier transform of the selected regions, phase gradient along x and y direction of the complex field can be separately calculated provided the precise amount of the spatial carrier frequency introduced is known. The wrapped phase gradients along y and x direction are shown in Fig.6.5(c) and 6.5(d) respectively. In addition, it should be noted here that during the alignment of the cascaded Sagnac interferometers and the accompanying lenses, there can be optical system which can introduce aberrations and they have to be cancelled. Therefore, the phase of the complex field obtained for a particular case is always compared to that obtained for the initial condition of a well collimated beam; thereby automatically cancelling the phase introduced by the spatial carrier frequency and the system induced aberrations.

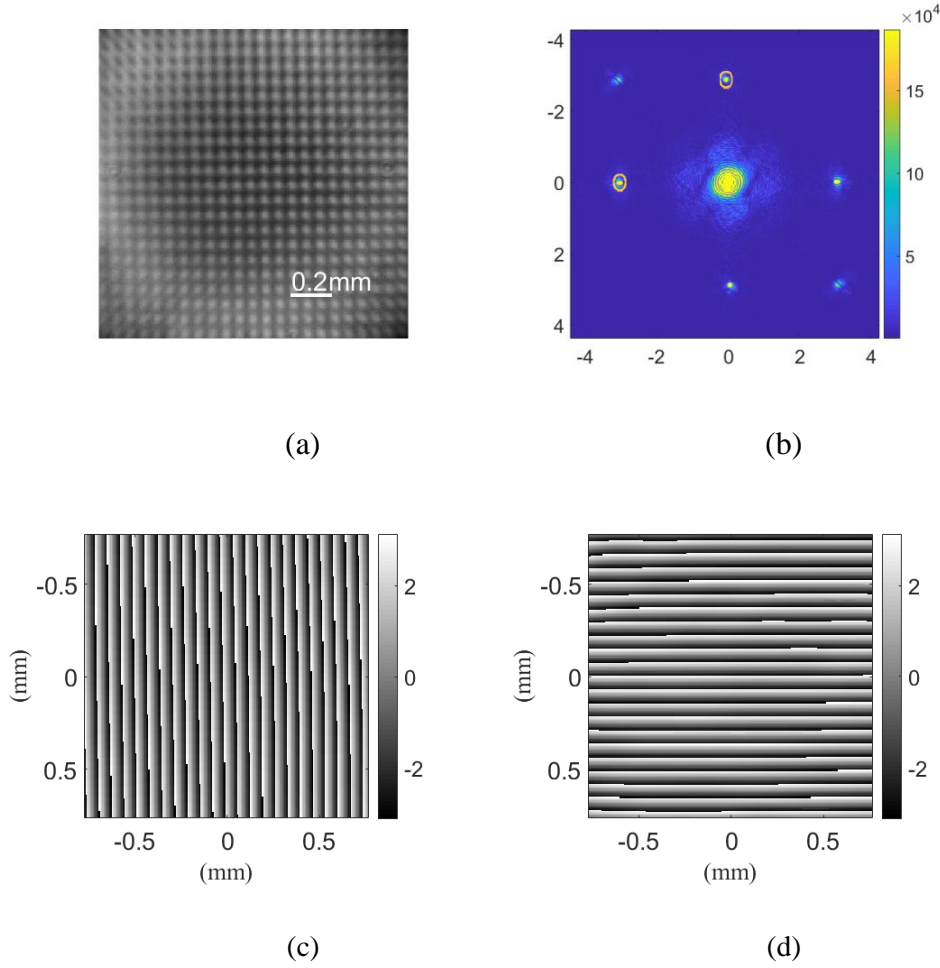


Figure 6.5 (a) Interferogram, (b) Fourier transform of fringe pattern, (c) Wrapped phase gradient along y-direction and (d) Wrapped phase gradient along x-direction.

Further, proper phase unwrapping algorithm is performed to get the phase gradient information without 2π jumps in the wrapped phase. Figure 6.6(a) and 6.6(b) show the calculated phase gradient information along x and y directions respectively when the collimating lens is shifted by an amount of 1.25 mm from the initial position. We use two-dimensional trapezoidal numerical integration method to integrate these x and y gradient that will reconstruct the complete wavefront $W(x,y)$. In case that the gradients are not exactly orthogonal due to alignment limitations in the experiment, an orthonormalization process is followed before integration. Figure 6.6(c) shows the reconstructed wavefront from obtained phase gradients. The same process is repeated

for recorded interferogram at different positions of collimating lens (0 mm, 0.25 mm, 0.5 mm, 0.75 mm, 1.0 mm and 1.25 mm) from the initial position as shown in Fig.6.7.

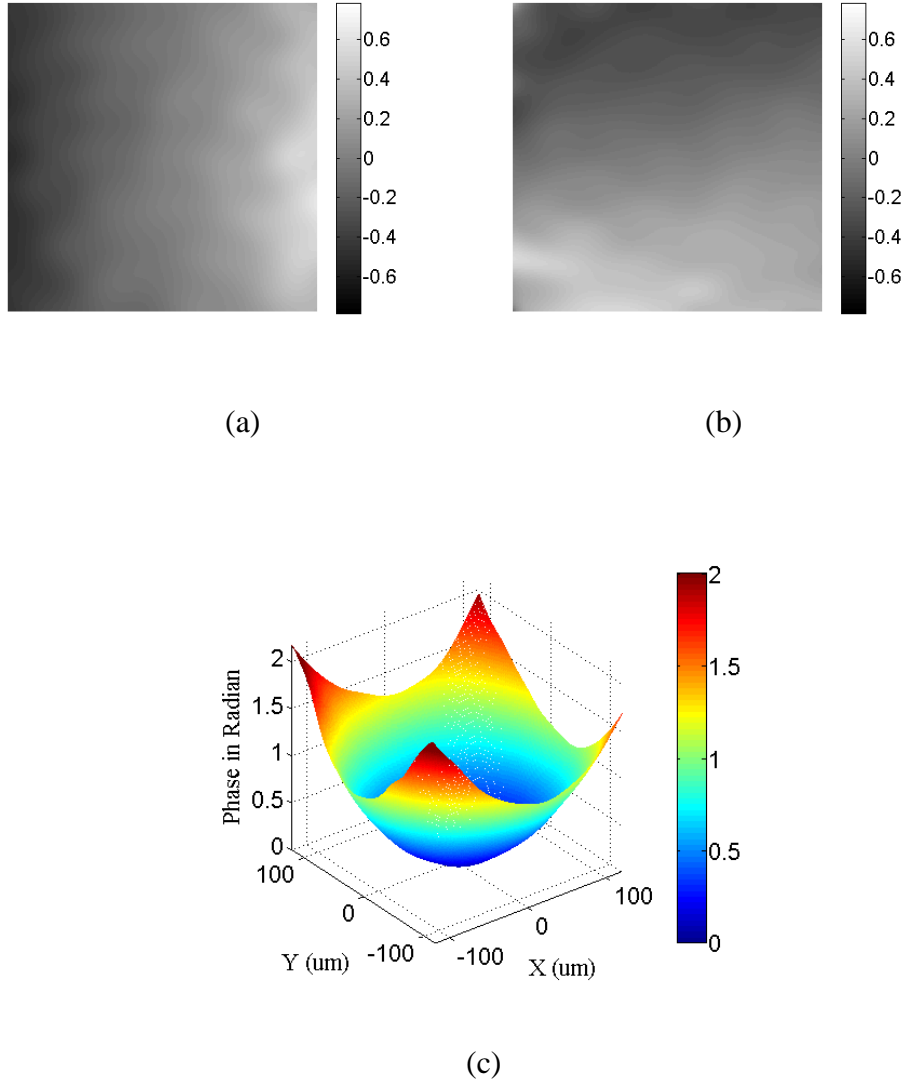


Figure 6.6 (a) & (b) Unwrapped phase gradient along x and y-direction respectively and (c) Reconstructed phase.

Using the parameters used for the experiment, a numerical simulation was performed using MATLAB software for wavefront reconstruction by using phase gradients obtained by orthogonal shearing of wavefront with different position of collimating lens as done in experiment. Figure 6.7 shows the 3D view and the line profile of

reconstructed wavefront where Red dashed line represents experimental and Blue line represents simulation results. For each wavefront Peak to Valley (PV) and root mean square (RMS) values are calculated. The matching results confirm the accurate and stable wavefront reconstruction achieved using the scheme. As it is observed from the results shown in Fig.6.7, there is tilt in experimental results. This can be attributed to the in-plane mechanical movement of lens mount when the collimating lens is shifted along z -direction.

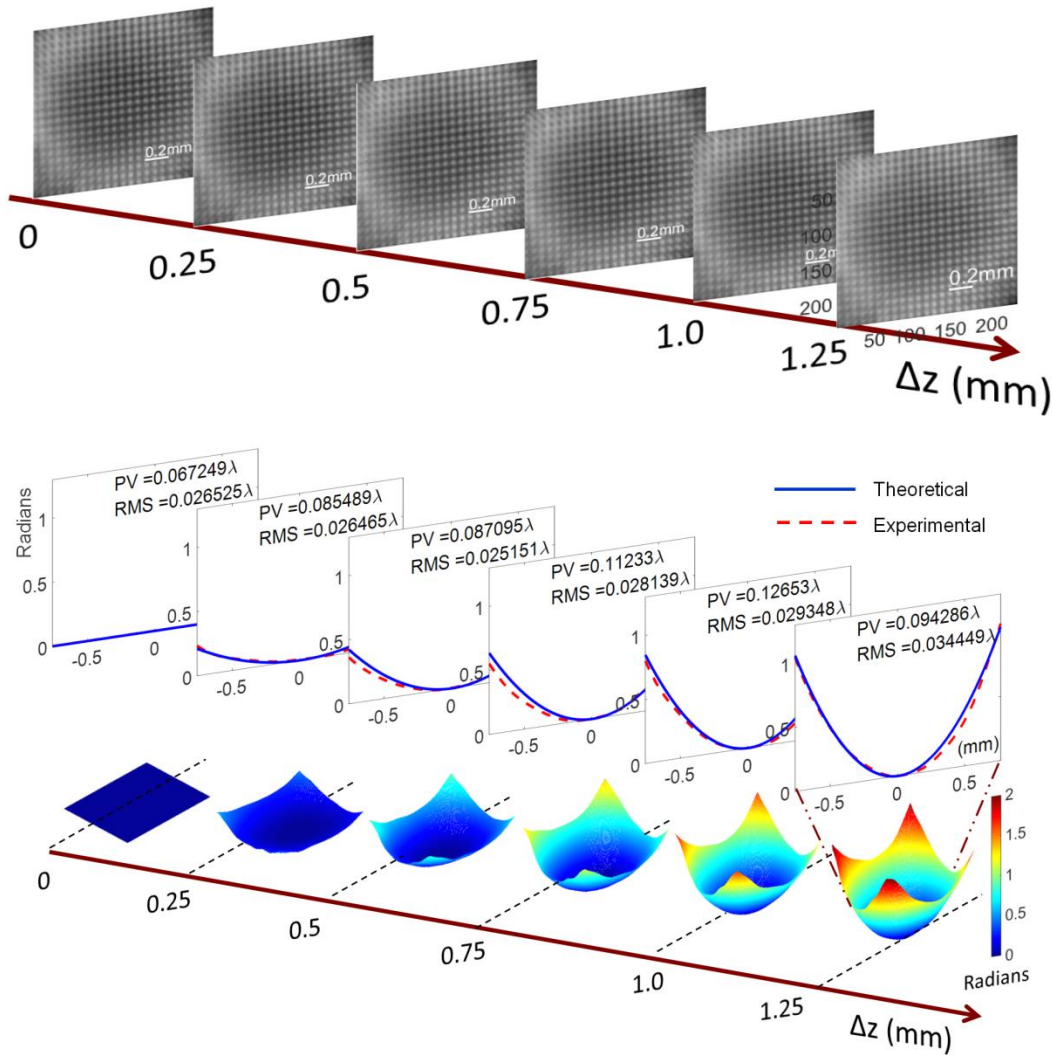


Figure 6.7 Recorded interferogram, line profile and 3D plot of reconstructed phase at different position of collimation lens.

6.3.2 Sensing of wavefront distortion by atmospheric turbulence simulator

The cascaded Sagnac vectorial shearing interferometry based wavefront sensor is validated in last experiment. Now the sensing of wavefront distortion is done when Pseudo Random Phase Plate (an atmospheric turbulence mimic) is introduced in the path of collimated beam as shown in Fig.6.8. The details of PRPP is given in Appendix A.

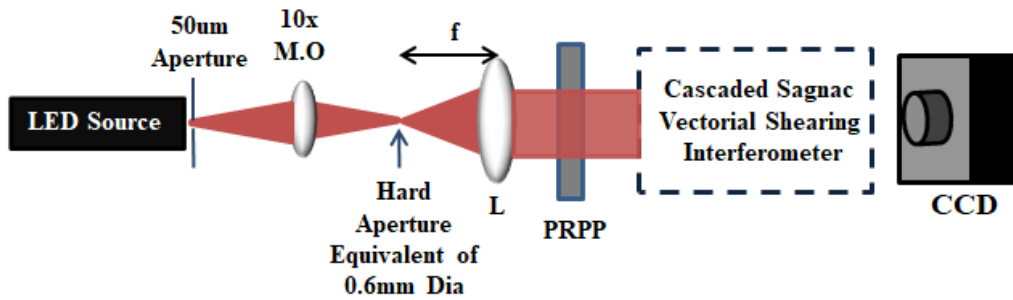


Figure 6.8 Wavefront sensing of aberrated wavefront by PRPP using vectorial shearing interferometer.

The recorded Interferograms at different position of PRPP and corresponding reconstructed Wavefronts are shown in Fig.6.9. First interferogram is recorded in the absence of PRPP which is considered as reference wavefront. The other five interferograms recorded when PRPP was rotating i.e. when beam was passing through different points on annular region of PRPP. Due to possible dust and stains on the PRPP, the intensity varies across the field of view due to transmission losses. However, a careful look at the fringes reveals spatial modulation of its spacing. These recorded interferogram are then digitally processed as mentioned earlier. The lower half of Fig.6.9 shows the distortions in wavefront as PV and RMS values with respected to reference wavefront.

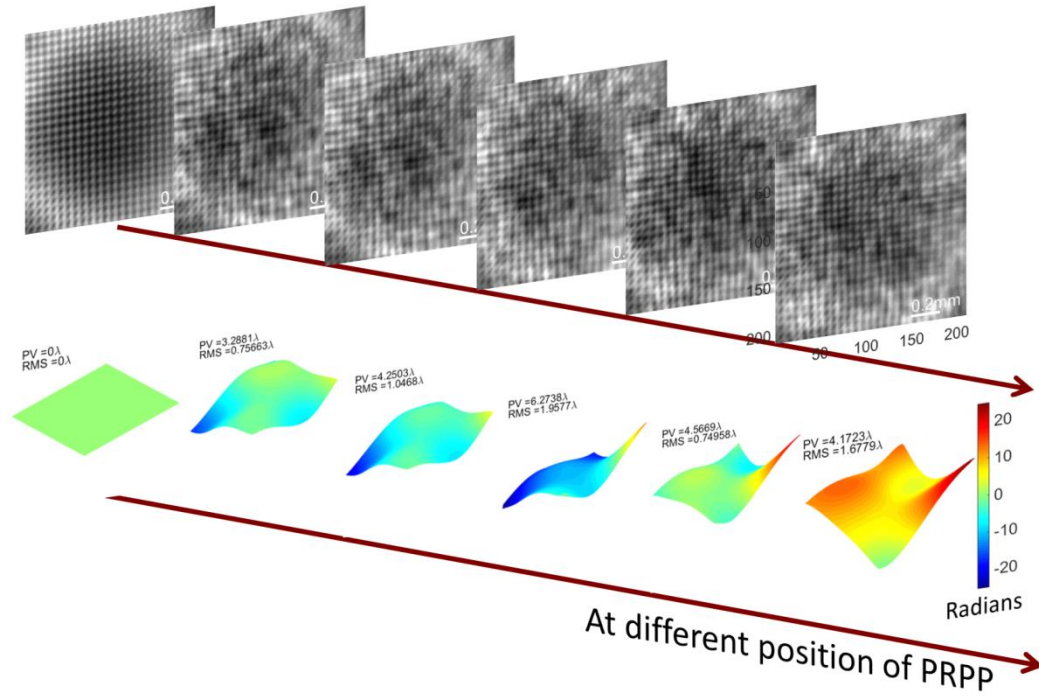


Figure 6.9 Interferograms at different position of PRPP and corresponding reconstructed Wavefronts

6.4 Discussion

When diffractive optical elements are used to generate the copies of the wavefront [36-39], the shear becomes wavelength dependent [Appendix D]. As a consequence, the phase difference/gradient becomes independent of wavelength. This property rendered those schemes achromatic. This condition is valid only if one assumes linearity in phase variation between the two points on the wavefront that are brought together and interfered through lateral shear. This condition is generally satisfied as the amount of lateral shear is chosen depending on the phase gradient being measured. The spatial carrier fringe introduced in the interference between the wavefront copies also retains the same periodicity irrespective of the wavelength. In short, the use of diffractive optics to generate the necessary wavefront copies seems to be the best option. However, fabrication of such dedicated element can be challenging. On the contrary, our technique will not have this problem as we use

simple reflections to generate the wavefront copies. However, in this case, the lateral shear being independent of the wavelength, the conditions of achromaticity discussed above will not be met. This is one of the reasons that set our scheme different from that of grating based schemes. We show that the wavelength dependence of the phase gradient does not influence the measurement as long as the spectral distribution is Gaussian. This can be explained with the example of white light interferometry where the phase difference corresponding to the central wavelength is accurately measured [95]. The periodicity of the spatial carrier fringe depends on wavelength. This can lead to reduction in contrast of the fringes at the periphery of the interferogram. However, with LED having a spectral band width of 16 nm used in our experiment, the contrast of the carrier fringes were detectable using an 8 bit CCD sensor.

Practically, it is difficult to derive a light source having high spatial coherence and sufficient intensity from a spatially incoherent extended source. For the field propagated from an extended incoherent source, the spatial coherence dies out as a function of increasing correlation length (lateral shear). We overcome this issue by choosing a hard-edged circular disk at the extended source plane and introduced the side lobes for the spatial coherence function. It can be thought of as reviving a decaying or dying function. The introduction of the hard aperture was an easier option for the spatial coherence revival. Alternatively, a two dimensional amplitude grating as the mask for the extended source can synthesize high spatial coherence at a particular correlation length (lateral shear) decided by the pitch of the grating. As a practical application of the proposed experimental scheme, we reconstructed the wavefront of a low coherent source when passed through Pseudo Random Phase Plate (PRPP), an atmospheric turbulence simulator.

6.5 Summary

We overcame the limitations introduced by temporal and spatial coherence through the choice of Gaussian spectra for the light source and using hard aperture at the source respectively for sensing aberrated wavefronts using low coherent source like

Light Emitting Diode(LED). The proposed scheme has immense potential in astronomical and biomedical sensing applications with low-coherent light sources.

Chapter 7

Conclusion and Future Scope

The initial focus of the thesis is to reveal the impact of atmospheric turbulence mimicking PRPP on Gaussian and Laguerre Gaussian beam when passing through it. There were challenges in sensing of highly turbulent impacted wavefront using SHWFS. This paved the way to work on cascaded Sagnac VSI. This wavefront sensing techniques is extended to the detection of wavefront of low coherent sources.

- This thesis begins with an experimental analysis of double passage Gaussian beam through a dynamic (rotating) pseudo random phase plate (PRPP) mimicking atmospheric turbulence and single passage topologically charged Laguerre Gaussian beams of odd and even charges. Intensities and beam centroid data at different plane from PRPP is captured by SHWFS for calculating Variance matrix elements. The physical parameters of Variance matrix are calculated and compared for double pass Gaussian beam and topologically charged beams. It is found that there is enhancement in fluctuation for all these parameters after insertion of PRPP. Asymmetry for double pass Gaussian beam found higher than LG beam.
- Further, intensities and centroid values captured from SHWFS are used to measure scintillation and beam wander. It is observed that the topologically charged beams show less scintillation and beam wander compared to Laser Gaussian beams. It is observed that when Laguerre Gaussian beam passed through dynamic turbulence the charge of higher order beam retains. Zernike coefficients for turbulence impacted beams have been calculated using SHWFS. Higher order aberration values with and without PRPP are difficult to distinguish due to poor spatial resolution. To measure aberrated phase information accurately, wavefront sensor with more spatial resolution would be required.

- This thesis also presents the principle and experimental results of a wavefront sensor using Vectorial shearing interferometer (common path interferometer) and a telecentric lens system. In this sensor the amount of spatial carrier frequency for multiplexing the shearing interferogram can be fixed by introducing controlled mirror alignments of cascaded Sagnac interferometer. The lateral shear can be varied by moving the detector plane along z direction and the wavefront gradient along two perpendicular directions are computed simultaneously. Wavefront curvature induced due to motion of collimation is measured. It is shown that mechanical errors inducing wavefront deviations of the order of fraction of wavelength can be detected using the cascaded sagnac VSI wavefront sensor.
- Further comparative analysis of SHWFS and cascaded Sagnac VSI is carried out. It is observed that SHWFS resolution is limited by sub-aperture size of micro lens array whereas cascaded Sagnac VSI resolution depends on the minimum pixels of sensor required to solve one fringe. Wavefront reconstruction for VSI is better than SHWFS as no special curve fitting algorithms are required in VSI and under high atmospheric turbulence condition cascaded Sagnac VSI measurement of measures the wavefront better than SHWFS.
- Finally the detection of low coherent source wavefront like Light Emitting Diode (LED) is performed using cascaded VSI. The limitations introduced by temporal is overcome through the choice of Gaussian spectra for the light source. The spatial coherence can be revived using hard aperture at the extended source.

The future scope for the research work in the thesis is as follows:

- Since the cascaded Sagnac is used to generate four copies of input wavefront it makes VSI little complicated. The efficiency also reduced to ~19% as two beam splitters are used. So if VSI can be designed with single Sagnac

interferometer then the efficiency can be increased and complexity of the system can be reduced.

- Since VSI will give gradients along two directions and intensity information simultaneously it can be used for analysing the Optical beams propagating through atmospheric turbulence.
- The study on phase detection and reconstruction of optical singularity can be done using VSI.
- The cascaded Sagnac VSI can be made into a product by proper designing using Zemax or CodeV optical designing tools.

REFERENCES

1. R. K. Tyson, "Principles of Adaptive Optics," 3rd ed. CRC Press, Boca Raton, FL, 2011.
2. V.I. Tatarskii, "Wave propagation in a turbulent medium," New York, McGraw Hill, 1961.
3. A. Ishimaru, "Wave propagation and scattering in random media", New York, Academic Press, 1977.
4. D. G. Marangon, G. Vallone and P. Villoresi, "Random bits, true and unbiased, from atmospheric turbulence," scientific report 4 (2014);
5. M. D. Drake, C. F. Bas, D. Gervais, P. F. Renda, D. Townsend, J. J. Rushanan, J. Francoer, N. Donnangelo and M. D. Stenner, "Optical key distribution system using atmospheric turbulence as the randomness generating function; classical optical protocol for information assurance," Optical engineering, 52, 055008-055008 (2013);
6. N. C. Donnangelo, M. D. Drake, C. F. Bas, P. F. Renda, J. J. Rushanan, , and D. Gervais, "Generating identical numerical sequence utilizing a physical property and secure communication using using such sequence" U S Patent 8,189,785 (2012).
7. J. Strohbehn ed., "Laser beam propagation in the atmosphere", New York, Springer Verlag, 1978.
8. R. L. Fante, "Electromagnetic beam propagation in turbulent media: An update," Proc. IEEE **68**, 1434, (1980).
9. B. C. Platt and R. Shack, "History and Principles of Shack-Hartmann Wavefront Sensing," Journal of Refractive Surgery **17**, 573-577 (2001)
10. D. R. Neal, J. Copland, D. A. Neal, "Shack-Hartmann wavefront sensor precision and accuracy," Proc. SPIE 4779, Advanced Characterization Techniques for Optical, Semiconductor, and Data Storage Components, (11 November 2002).

11. P. M. Blanchard, D. J. Fisher, S. C. Woods, and A. H. Greenaway, "Phase-diversity wave-front sensing with a distorted diffraction grating," *Appl. Opt.* **39**, 6649-6655 (2000).
12. J. Primot, "Three-wave lateral shearing interferometer", *Appl. Opt.* **32**, 6242-6249, (1993).
13. K. L. Baker, "Least-squares wave-front reconstruction of Shack-Hartmann sensors and shearing interferometers using multigrid techniques," *Review of Scientific Instruments* **76**, 053502 (2005).
14. J. R. Fienup, "Phase retrieval algorithms: a comparison," *Appl. Opt.* **21**, 2758-2769 (1982).
15. M. N. Malakhov, and B. V. Prilepskii, "Method of determining the wavefront profile from information using a detector of the Hartmann type." *Opt Spectrosc (USSR)* **58** 271(1985).
16. J. R. Fienup, "Reconstruction of an object from the modulus of its Fourier transform," *Opt. Lett.* **3**, 27-29 (1978).
17. J. R. Fienup, "Lensless coherent imaging by phase retrieval with an illumination pattern constraint," *Opt. Express* **14**, 498-508 (2006).
18. R. A. Gonsalves, "Fundamentals of wavefront sensing by phase retrieval," *Proc. SPIE* **351**, 56 (1982).
19. R. A. Gonsalves "Phase retrieval by differential intensity measurements," *J Opt Soc Am A* **4**, 166 (1987).
20. J. T. Foley, and M. A. Abdul Jalil. "Role of diffraction in phase retrieval from intensity measurements." *Proc. SPIE* **351**, 80(1982).
21. M. L. Teague, "Image formation in terms of the transport equation." *J Opt Soc Am A* **2**, 2019-26 (1985).
22. Southwell, W. H. "Wavefront analyzer using a maximum likelihood algorithm." *J Opt Soc Am* **67**, 396 (1977).
23. S. K. Gautam, R. K. Singh, C S Narayanamurthy and D. N Naik, "Reconstruction of complex-object using edge point referencing," *J. Opt.* **22**, 055601 (2020).

24. Robinson, S. R. "On the problem of phase from intensity measurements." J Opt Soc Am **68**, 87 (1978).
25. J. Mocci, F. Busato, N. Bombieri, S. Bonora, and R. Muradore, "Efficient implementation of the Shack–Hartmann centroid extraction for edge computing," J. Opt. Soc. Am. A **37**, 1548-1556 (2020).
26. J. V. Sheldakova, A. V. Kudryashov, V. Y. Zavalova, and T. Y. Cherezova "Beam quality measurements with Shack-Hartmann wavefront sensor and M2-sensor: comparison of two methods", Proc. SPIE 6452, Laser Resonators and Beam Control IX, 645207 (14 February 2007).
27. Kudryashov, V. Samarkin, A. Alexandrov, J. Sheldakova and V. Zavalova, "Shack-Hartmann wavefront sensor - advantages and disadvantages," 2010 International Conference on Advanced Optoelectronics and Lasers, Sevastopol, 2010, pp. 76-77.
28. N. Gu, L. Huang, Z. Yang and C. Rao, "A single-shot common-path phase-stepping radial shearing interferometer for wavefront measurements", Opt. Express **19**, 4703-4713 (2011).
29. C. Roddier, F. Roddier, and J. Demarcq. "Compact rotational shearing interferometer for astronomical applications." Opt Eng 28, 66 (1989).
30. F. Roddier, "Curvature sensing and compensation: A new concept in adaptive optics." Appl Opt **27**, 1223 (1988).
31. D. G. Sandler, L. Cuellar, M. Lefebvre, T. Barrett, R. Arnold, P. Johnson, A. Rego, G. Smith, G. Taylor, and B. Spivey. "Shearing interferometry for laser-guide-star atmospheric correction at large D/r_0 ." J Opt Soc Am A **11**, 858 (1994).
32. G. Paez, M. Strojnik, and G. G. Torales, "Vectorial shearing interferometer", Appl. Opt. **39**, 5172-5178 (2000).
33. C. Elster and I. Weingärtner, "Exact wave-front reconstruction from two lateral shearing interferograms," J. Opt. Soc. Am. A **16**, 2281-2285 (1999).
34. M. Servin, D. Malacara, and J. L. Marroquin, "Wave-front recovery from two orthogonal sheared interferograms," Appl. Opt. **35**, 4343-4348 (1996).

35. S. Wang, J. Dong, F. Poller, X. Dong, M. Lu, L. M. Bilgeri, M. Jakobi, F. Salazar-Bloise, and A. W. Koch, "Dual-directional shearography based on a modified common-path configuration using spatial phase shift," *Appl. Opt.* **58**, 593-603 (2019).
36. J. Primot and L. Sogno, "Achromatic three-wave (or more) lateral shearing interferometer", *J. Opt. Soc. Am. A* **12**, 2679-2685 (1995).
37. S. Velghe, J. Primot, N. Guérineau, M. Cohen, and B. Wattellier, "Wave-front reconstruction from multidirectional phase derivatives generated by multilateral shearing interferometers," *Opt. Lett.* **30**, 245–247 (2005).
38. J. C. Chanteloup, "Multiple-wave lateral shearing interferometry for wave-front sensing", *Appl. Opt.* **44**, (2005).
39. J. C. Chanteloup, F. Druon, M. Nantel, A. Maksimchuk, and G. Mourou, "Single-shot wave-front measurements of high-intensity ultrashort laser pulses with a three-wave interferometer," *Opt. Lett.* **23**, 621-623 (1998).
40. K. Otaki, N. Kohara, K. Sugisaki, Y. Ichikawa, Y. Zhu, K. Murakami, C. Ouchi, S. Kato, M. Hasegawa, T. Honda and M. Takeda, "Ultra High-Precision Wavefront Metrology Using EUV Low Brightness Source," In: Osten W. (eds) *Fringe 2013*. Springer, Berlin, Heidelberg.
41. R. Simon and N. Mukunda, "Optical phase space, Wigner representation, and invariant quality parameters," *J. Opt. Soc. Am. A* **17**, 2440–2463 (2000).
42. R.F. O'Connell, "The Wigner distribution function—50th birthday", *Found Phys* **13**, 83–92 (1983).
43. R. Simon and N. Mukunda, "Moments of the Wigner distribution and a generalized uncertainty principle," *arXiv: quant-ph/ 9708037* (1997).
44. R. Simon, E. C. G. Sudarshan, and N. Mukunda, "Generalized rays in first order optics: transformation properties of Gaussian Schell-model fields," *Phys. Rev. A* **29**, 3273–3279 (1984).
45. R. Simon, E. C. G. Sudarshan, and N. Mukunda, "Anisotropic Gaussian Schell-model beams: passage through optical systems and associated invariants," *Phys. Rev. A* **31**, 2419–2434 (1985).

46. R. Simon, E. C. G. Sudarshan, and N. Mukunda, "Gaussian Wigner distributions in quantum mechanics and optics," *Phys. Rev. A* **36**, 3868–3880 (1987).
47. W. Schempp, J. S. Mondragon and K. B. Wolf, "Analog radar signal design and digital signal processing—a Heisenberg nilpotent Lie group approach," in *Lie Methods in Optics*, Vol. **250** of *Lecture Notes in Physics* (Springer-Verlag, Berlin), 1–27 (1986).
48. M. J. Bastiaans, "The Wigner distribution function applied to optical signals and systems," *Opt. Comm.* **25**, 26–30 (1978).
49. M. J. Bastiaans, "Wigner distribution function and its application to first-order optics," *J. Opt. Soc. Am.* **69**, 1710–1716 (1979).
50. R. Simon, N. Mukunda and B. Dutta, "Quantum-noise matrix for multimode systems: $U(n)$ invariance, squeezing, and normal forms," *Physical Review A*, **49**, 1567 (1994);
51. R. Simon and N. Mukunda, "Optical phase space, Wigner representation, and invariant quality parameters," *J. Opt. Soc. Am. A* **17**, 2440–2463 (2000).
52. D. R. Neal, W. Alford, J. K. Greutzner and M. E. Warren, "Amplitude and phase beam characterization using two dimensional wavefront sensors". In *Third international workshop on Laser Beams and Optics characterization* (pp. 72–82) International society for Optics and Photonics (1996).
53. D. R. Neal, W. Alford and J. K. Greutzner, "Beam characterization by wavefront sensor". US patent 5,936,720 (1999).
54. D. R. Neal, R. R. Rammage, D. J. Armstrong and W.T. Turner, "Apparatus and method characterizing pulsed light beams" US patent 6,052,180 (2000).
55. B. Schäfer and K. Mann, "Investigation of the propagation characteristics of excimer lasers using a Hartmann–Shack sensor," *Review of Scientific Instruments* **71**, 2663 (2000).
56. Bernd Schäfer and Klaus Mann, "Determination of beam parameters and coherence properties of laser radiation by use of an extended Hartmann-Shack wave-front sensor," *Appl. Opt.* **41**, 2809–2817 (2002)

57. B. Schäfer, M. Lübbecke, and K. Mann, "Hartmann-Shack wave front measurements for real time determination of laser beam propagation parameters," *Review of Scientific Instruments* **77**, 053103 (2006).
58. R. Lane and M. Tallon, "Wavefront reconstruction using Shack Hartmann sensor," *Appl. Optics* **31**, 6902-6908 (1992).
59. R. H. Hudgin "Wavefront reconstruction for compensated imaging," *JOSA* **67**, 375-378(1977).
60. D. L. Fried, "Least square fitting a wavefront distortion estimate to an array of phase difference measurements," *JOSA* **67**, 370-375 (1977)
61. W. H. Southwell "Wavefront estimation from wavefront slope measurements" *JOSA* **70**, 998-1006 (1980);
62. J. Herrmann "Least square wavefront errors of minimum norm" *JOSA* **70**, 28-35 (1980).
63. M. A. van Dam, R. G. Lane et. Al., "Wavefront sensing from defocused images by use of wavefront slopes," *Appl. Optics* **41**, 5497-5502 (2002).
64. A. Talmi and E. M. Ribak, "Wavefront reconstruction from its gradients," *JOSA A* **23**, 288-297 (2006).
65. R. J. Noll, "Zernike polynomials and atmospheric turbulence, *J. Opt. soc. Am* **66**, 207 (1976).
66. L. Allen, M. W. Beijersbergen, R. Spreeuw and J. Woerdman, "Orbital angular momentum of light and transformation of Laguerre Gaussian laser modes," *Physical review A* **45**, 8185 (1992).
67. M. W. Beijersbergen, L. Allen, H. Van der Veen and J. Woerdman, "Astigmatic laser modes convertors and transfer of orbital angular momentum," *optical angular momentum* **96**, 123-132 (2003).
68. C. Paterson, "Atmospheric Turbulence and Orbital Angular Momentum of Single Photons for Optical Communication," *Phys. Rev. Lett.* **94**, 153901 (2005).
69. G. Gbur and R. K. Tyson, "Vortex beam propagation through atmospheric turbulence and topological charge conservation," *J. Opt. Soc. Am. A* **25**, 225-230 (2008).

70. Y. Zhang, M. Tang, and C. Tao, "Partially coherent vortex beam propagation in a turbulent atmosphere," *Chin. Opt. Lett.* **3**, 559–561 (2005)
71. L. Andrews and R. Phillips, *Laser beam propagation in turbulent atmosphere*. SPIE press; 2005.
72. A. Saito, A. Tanabe, M. Kurihara, N. Hashimoto and K. Ogawa, "Propagation characteristics for quantized Laguerre-Gauss beams using liquid crystal optical devices," *Technical Digest of the 20th Micro optics, Conference (MOC'15)*, 98-99 (2015).
73. R. Mahon, C. Moore, M. Ferraro, W. Rabinovich and M. Suite, "Atmospheric turbulence effects measured along horizontal-path optical retro-reflector links," *Appl. Opt.* **51**, 6147–58 (2012).
74. Y. Huang, Y. Yuan, X. Liu, J. Zeng, F. Wang, J. Yu, L. Liu and Y. Cai, "Propagation of optical coherence vortex lattices in turbulent atmosphere" *Appl. Sci.* **8**, 2476 (2018).
75. G. Berman, V. Gorshkov and S. Torous, "Scintillation Reduction for Laser Beams Propagating Through Turbulent Atmosphere" *Journal of Physics B: Atomic, Molecular and Optical Physics* **44** (2010).
76. Avner Peleg and Jerome V. Moloney, "Scintillation index for two Gaussian laser beams with different wavelengths in weak atmospheric turbulence," *J. Opt. Soc. Am. A* **23**, 3114-3122 (2006).
77. X. Liu, Y. Shen, L. Liu, F. Wang and Y. Cai, "Experimental demonstration of vortex phase-induced reduction in scintillation of a partially coherent beam," *Optics Letters* **38-24**, 5323-26 (2013).
78. A. Peleg and J. V. Moloney, "Scintillation index for two Gaussian laser beams with different wavelengths in weak atmospheric turbulence," *J. Opt. Soc. Am. A* **23**, 3114-3122 (2006).
79. Madhu V. and J. S. Ivan, "Robustness of the twist parameter of Laguerre-Gaussian mode superpositions against atmospheric turbulence," *Phys. Rev. A* **95**, 043836 (2017).

80. Y. Barabanenkov, Y. Kravtsov, V. Ozrin and A. Saichev, "Enhanced backscattering in optics," *Prog. Opt* **29**, 65–197 (1991).
81. E. Jakeman, "Enhanced backscattering through a deep random phase screen," *J Opt Soc. Am A* **5**, 1638–1648 (1988)
82. L. Andrews, R Phillips and W. Miller, "Mutual coherence function for a double-passage retro reflected optical wave in atmospheric turbulence," *Appl. Opt* **36**, 698–708 (1997).
83. B. Agrovskii, A. Bogaturov, A. Gurvich, S. Kireev and V. Myakinin, "Enhanced backscattering from a plane mirror viewed through a turbulent phase screen," *J Opt Soc. Am A* **8**, 1142–1147 (1991).
84. J. Churnside, and J. Wilson, "Enhanced backscatter of a reflected beam in atmospheric turbulence," *Appl. Opt* **32** (15), 2651–2655 (1993)
85. J. Yu, Y. Huang, G. Gbur, F. Wang, Y. Cai, "Enhanced backscatter of vortex beams in double-pass optical links with atmospheric turbulence," *Journal of Quantitative Spectroscopy and Radiative Transfer*, **228**, 1–10 (2019).
86. R. Sharma, J. S. Ivan, and C. S. Narayanamurthy, "Wave propagation analysis using the variance matrix," *J. Opt. Soc. Am. A* **31**, 2185–2191 (2014).
87. R. Sharma, "Investigation on wave propagation through pseudo random phase plate using He-Ne laser at 633nm," Ph.D Thesis, Indian institute of space science and technology, Thiruvananthapuram Kerala India (2015).
88. S. V. Mantravadi, T. A. Rhoadarmer and R. S. Glas, "Simple laboratory system for generating well-controlled atmospheric like turbulence, in: *Optical Science and Technology*," The SPIE 49th Annual Meeting, International Society for Optics and Photonics, 290–300 (2004).
89. E. M. Steven, "Pseudo-random phase plates." *International Symposium on Optical Science and Technology. International Society for Optics and Photonics*, (2002).
90. A. T. O'Neil, I. MacVicar, L. Allen, and M. J. Padgett, "Intrinsic and Extrinsic Nature of the Orbital Angular Momentum of a Light Beam" *Phys. Rev. A* **88**, 053601 (2002).
91. J. Goodman, *Introduction to Fourier Optics*, 3rd ed. (Roberts & Company, 2005).

92. K. Ichikawa, A. Lohmann, and M. Takeda, "Phase retrieval based on the irradiance transport equation and the Fourier transform method: experiments," *Appl. Opt.* **27**, 3433-3436 (1988).
93. L. A. Poyneer, D. T. Gavel, and J. M. Brase, "Fast wave-front reconstruction in large adaptive optics systems with use of the Fourier transform," *J. Opt. Soc. Am. A* **19**, 2100-2111 (2002).
94. Dubra, C. Paterson, and C. Dainty, "Wave-front reconstruction from shear phase maps by use of the discrete Fourier transform," *Appl. Opt.* **43**, 1108-1113 (2004).
95. P. Sandoz and G. Tribillon, "Profilometry by zero-order interference fringe identification," *J. Mod. Opt.*, **40**, 1691-1700 (1993).
96. M. Takeda, W. Wang, Z. Duan, and Y. Miyamoto, "Coherence holography," *Opt. Express* **13**, 9629-9635 (2005).
97. D. Nankivil, A. Dhalla, N. Gahm, K. Shia, S. Farsiu, and J. Izatt, "Coherence revival multiplexed, buffered swept source optical coherence tomography: 400 kHz imaging with a 100 kHz source," *Opt. Lett.* **39**, 3740-3743 (2014).
98. M. Takeda, H. Ina, and S. Kobayashi, "Fourier-transform method of fringe-pattern analysis for computer-based topography and interferometry," *J. Opt. Soc. Am.* **72**, 156-160 (1982).
99. M. Takeda, Q. Gu, M. Kinoshita, H. Takai, and Y. Takahashi, "Frequency-multiplex Fourier-transform profilometry: a single-shot three-dimensional shape measurement of objects with large height discontinuities and/or surface isolations," *Appl. Opt.* **36**, 5347-5354 (1997).

Appendix- A

Pseudo random phase plate

There are several methods by which one can simulate atmospheric turbulence in laboratory [88-89]. The Pseudo Random Phase Plate (PRPP) used in the experiments for mimicking atmospheric turbulence, is a five layered transparent packed system consists of two outer layers made of BK-7 glass and the two inner layers of near index matching (NIM) polymer[88]. The middle one is an acrylic layer in which a turbulence profile is written onto one of its sides. The phase plate allows varying levels of turbulence which leads to aberrated wavefront. The phase screens that are machined on PRPP are generated using Fourier transform technique. Each phase screen has 4096 sample phase points across a side. The turbulence profile is mapped on a 3.28" acrylic annulus with a 1.35" diameter obscuration at the centre so that the spacing at each plate is $20\text{ }\mu\text{m}$ [7].

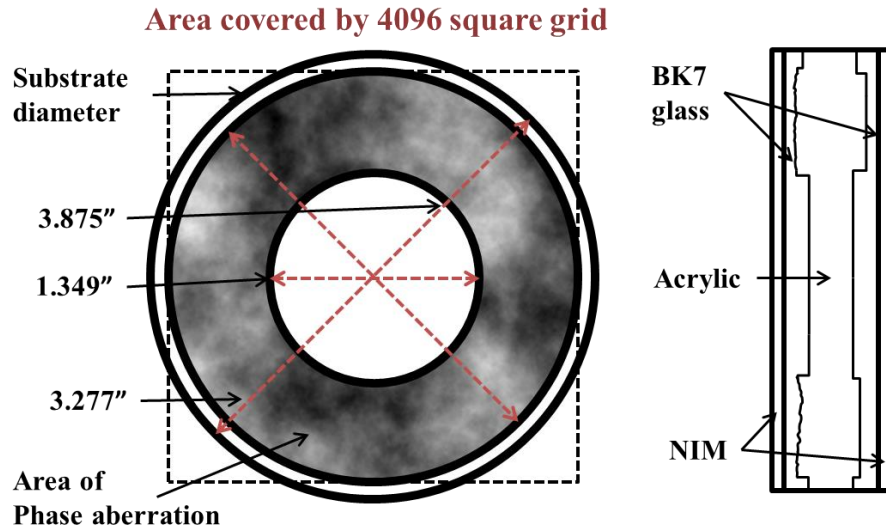




Figure A.1 Diagram of static Pseudo random phase plate [88]

The PRPP can be rotated in various velocities with the help of a computer controlled stepper motor with a single driver, so that the time varying phase profile can be achieved. The PRPP is fabricated using a technique called Near-Index-Match (NIM) optics. The principle of NIM is illustrated in Fig.4.4. Two different materials of refractive indices n_1 and n_2 with an interfacial surface profile $h(x)$ provides an optical path difference (OPD) on an incident plane wave which is given by

$$\begin{aligned} OPD(x) &= h(x)(n_1(\lambda) - n_2(\lambda)) \\ &= h(x)\Delta n(\lambda) \end{aligned}$$

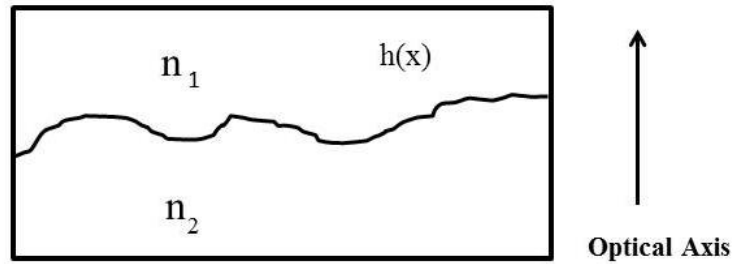


Figure A.2 Diagram of Near-Index-Match concept [89]

To produce an OPD of 1λ , a relief height of $\sim 50\lambda$ is required for an index difference (Δn) of ~ 0.02 [89]. While designing such combinations, for very small Δn , the required surface relief should be very high for adequate OPD. If Δn is very high, the accuracy of OPD will get affected due to precision of the machine tool. Practically, the index difference in the range 0.02-0.06 works well for wavelength range 0.5-1.5 μm with maximum machine tool accuracy [89].

Limitations

Even for well characterized materials, only a limited range of refractive index differences is available. Since the refractive index depends on wavelength and temperature, thermal and mechanical stresses affect the optical figure of a rigidly mounted optic. Mechanical stresses due to temperature changes leads to separation of sandwich. These stresses are greater for dissimilar materials like glass and polymers. The combination of acrylic and a castable optical element have similar thermal and mechanical properties, so this combination will be less affected by temperature [89].

Appendix B

Shack-Hartmann Wavefront Sensor

Shack-Hartmann Wavefront Sensor (SHWFS) is a widely used device for wavefront measurement. A SHWFS consists of micro lenslet array followed by CCD sensor. The CCD sensor is placed at focal point of the micro lenslet array. Each micro lens generates a spot in the sensor whenever a light beam is incident on it. The centroid of the spot depends on the slope of the wavefront in front of the lens.

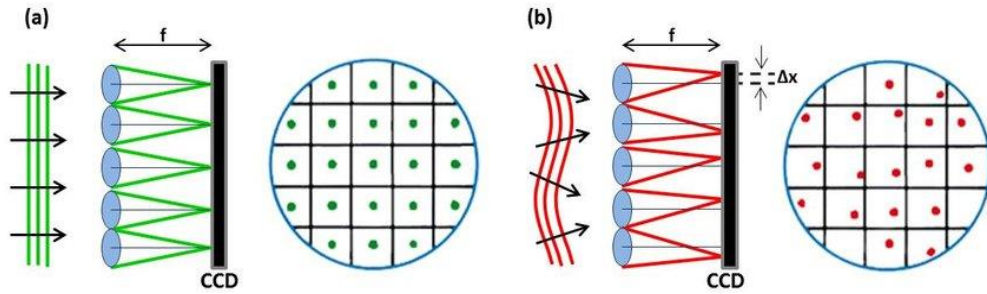


Figure B.1 (a) Plane wavefront incident on lenslet array and its spot diagram (b) Aberrated wavefront incident to micro lenslet array and its spot diagram.

Figure B.1. shows spot diagram detected using SHWFS for an incoming plane wavefront. The incoming wavefront is sampled on to small wavefronts equal to a small micro lens of lenslet array. As this incoming wavefront is normal to the optical axis of lens, it gets focused at focal point on optic axis and this is called reference spot position. Figure B.1 (a) shows spot diagram when a plane wave front (collimated beam) is incident on to a SHWFS. If this beam is aberrated then there will be shift in focal points of each lenslet array and that is shown in Fig.B.1 (b).

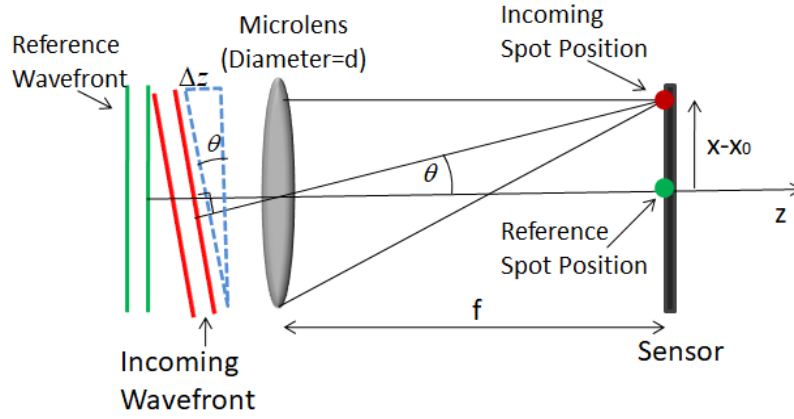


Figure B.2 Centroid shift for Single Lens

Fig.B.2 demonstrates about the response of one of single lenses in the lens-let array to an incoming wavefront. The slope of incoming wavefront is calculated from the Shack Hartmann wavefront sensor data using following equation:

$$\frac{x_{ij} - x_{0ij}}{f} = \tilde{\lambda} \frac{\partial \phi(x, y)}{\partial x} \quad (B.1)$$

$$\frac{y_{ij} - y_{0ij}}{f} = \tilde{\lambda} \frac{\partial \phi(x, y)}{\partial y}$$

Where, $\tilde{\lambda}$ is $\frac{2\pi}{\lambda}$ with $\lambda = 633nm$. Where, $\phi(x, y)$ is the shape of the wavefront. Its partial derivative along x and y direction can be calculated by spot shift $x_{ij} - x_{0ij}$ and $y_{ij} - y_{0ij}$ respectively and by focal length of the micro lens.

In this thesis, a Thorlabs Shack-Hartmann Wavefront Sensor WFS 150-5C has been used. Each lenslet is of $150\mu m$ diameter and pixels in that domain are 31×31 where each pixel size is $4.6\mu m$. The spot intensity measurement in each domain is done by calculating the summation of intensity over all pixels present in that domain. If each domain is labeled by indices i,j, then pixels in that domain can be labeled by k. The spot intensity in ij^{th} domain can be calculated as:

$$\sum_k N_{i,j}^k = I_{i,j} \quad (\text{B.2})$$

Where, k is the pixel index of $(i,j)^{\text{th}}$ domain and N is the intensity value stored at k^{th} pixel in $(i,j)^{\text{th}}$ domain. Shift in the centroid is calculated from the reference centroid spots.

Appendix C

Derivation for shearing copies generated by two cascaded Sagnac interferometer is wavelength independent.

To show that image is shifted and has a linear phase:

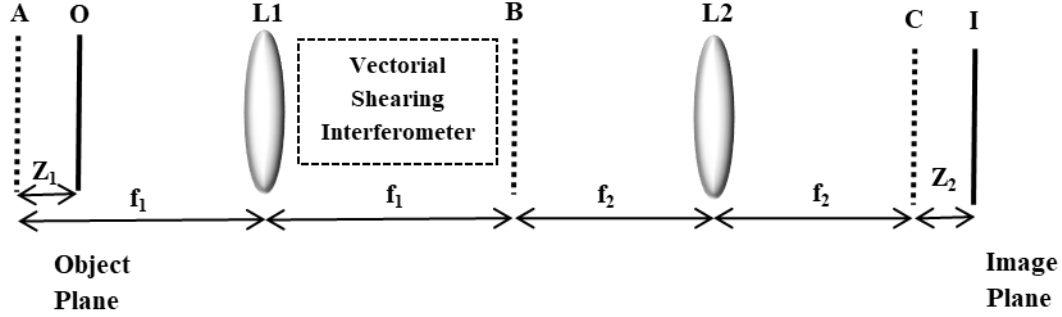


Figure C.1 Conceptual diagram for common-path VSI

Let, $u_O(x', y')$ be object field:

$$U_B(f_{x_b}, f_{y_b}) = F\{u_A(x', y')\} \quad (C.1)$$

$$u_A(x', y') = F^{-1} \left\{ F[u_O(x', y')] \times \exp \left(-i \frac{2\pi z_1}{\lambda} \sqrt{1 - \frac{\hat{x}^2}{f_1^2} - \frac{\hat{y}^2}{f_1^2}} \right) \right\} \quad (C.2)$$

$$u_B \left(\frac{\hat{x}}{\lambda f_1}, \frac{\hat{y}}{\lambda f_1} \right) = F[u_O(x', y')] \times \exp \left(-i \frac{2\pi z_1}{\lambda} \sqrt{1 - \frac{\hat{x}^2}{f_1^2} - \frac{\hat{y}^2}{f_1^2}} \right) \quad (C.3)$$

$$u_C(x, y) = F_{(f_2)} \left[F_{(f_1)} \{u_o(x', y')\} \times \exp \left(-i \frac{2\pi z_1}{\lambda} \sqrt{1 - \frac{\hat{x}^2}{f_1^2} - \frac{\hat{y}^2}{f_1^2}} \right) \right] \quad (C.4)$$

$$U_{BS}\left(\frac{\hat{x}}{\lambda f_1}, \frac{\hat{y}}{\lambda f_1}\right) = U_O\left(\frac{\hat{x} - \hat{x}_s}{\lambda f_1}, \frac{\hat{y} - \hat{y}_s}{\lambda f_1}\right) \times \exp\left(-i \frac{2\pi z_1}{\lambda} \sqrt{1 - \frac{(\hat{x} - \hat{x}_s)^2}{f_1^2} - \frac{(\hat{y} - \hat{y}_s)^2}{f_1^2}}\right)$$

(C.5)

$$U_C(x, y) = F_{(f_2)} \left\{ U_{BS}\left(\frac{\hat{x}}{\lambda f_1}, \frac{\hat{y}}{\lambda f_1}\right) \right\}$$

$$U_I(x, y) = F_{(f_2)}^{-1} \left\{ F_{(f_2)} [U_C(x, y)] \times \exp\left(i \frac{2\pi z_2}{\lambda} \sqrt{1 - \frac{\hat{x}^2}{f_2^2} - \frac{\hat{y}^2}{f_2^2}}\right) \right\}$$

$$U_I(x, y) = F_{(f_2)}^{-1} \left[F_{(f_2)} \left[F_{(f_2)} \left\{ U_{BS}\left(\frac{\hat{x}}{\lambda f_1}, \frac{\hat{y}}{\lambda f_1}\right) \right\} \right] \times \exp\left(i \frac{2\pi z_2}{\lambda} \sqrt{1 - \frac{\hat{x}^2}{f_2^2} - \frac{\hat{y}^2}{f_2^2}}\right) \right]$$

$$U_I(x, y) = F_{(f_2)}^{-1} \left[\begin{aligned} & U_O\left(\frac{-\hat{x} - \hat{x}_s}{\lambda f_1}, \frac{-\hat{y} - \hat{y}_s}{\lambda f_1}\right) \\ & \times \exp\left(-i \frac{2\pi z_1}{\lambda} \sqrt{1 - \frac{(\hat{x} + \hat{x}_s)^2}{f_1^2} - \frac{(\hat{y} - \hat{y}_s)^2}{f_1^2}}\right) \times \\ & \exp\left(i \frac{2\pi z_2}{\lambda} \sqrt{1 - \frac{\hat{x}^2}{f_2^2} - \frac{\hat{y}^2}{f_2^2}}\right) \end{aligned} \right]$$

$$z_1 = \frac{z_2}{m^2}, \quad m = \frac{f_1}{f_2}, \quad z_1 = z_2 \times \frac{f_2^2}{f_1^2}$$

$$U_I(x, y) = F_{(f_2)}^{-1} \left[\begin{aligned} & U_O\left(\frac{-\hat{x} - \hat{x}_s}{\lambda f_1}, \frac{-\hat{y} - \hat{y}_s}{\lambda f_1}\right) \\ & \times \exp\left(-i \frac{2\pi z_2}{\lambda} \frac{f_1^2}{f_2^2} \sqrt{1 - \frac{(\hat{x} + \hat{x}_s)^2}{f_1^2} - \frac{(\hat{y} - \hat{y}_s)^2}{f_1^2}}\right) \times \\ & \exp\left(i \frac{2\pi z_2}{\lambda} \sqrt{1 - \frac{\hat{x}^2}{f_2^2} - \frac{\hat{y}^2}{f_2^2}}\right) \end{aligned} \right]$$

(C.6)

Expanding exponential part.....

$$\begin{aligned}
& \exp\left(-i\frac{2\pi z_2}{\lambda}\frac{f_1^2}{f_2^2}\sqrt{1-\frac{(\hat{x}+\hat{x}_s)^2}{f_1^2}-\frac{(\hat{y}+\hat{y}_s)^2}{f_1^2}}\right)\times\exp\left(i\frac{2\pi z_2}{\lambda}\sqrt{1-\frac{\hat{x}^2}{f_2^2}-\frac{\hat{y}^2}{f_2^2}}\right) \\
& \exp\left(-i\frac{2\pi z_2}{\lambda}\frac{f_1^2}{f_2^2}\left(1-\frac{(\hat{x}+\hat{x}_s)^2}{2f_1^2}-\frac{(\hat{y}+\hat{y}_s)^2}{2f_1^2}\right)\right)\times\exp\left(i\frac{2\pi z_2}{\lambda}\left(1-\frac{\hat{x}^2}{2f_2^2}-\frac{\hat{y}^2}{2f_2^2}\right)\right) \\
& \exp\left(i\frac{2\pi z_2}{\lambda}\left(-\frac{f_1^2}{f_2^2}+\frac{(\hat{x}+\hat{x}_s)^2}{2f_1^2}+\frac{(\hat{y}+\hat{y}_s)^2}{2f_1^2}+1-\frac{\hat{x}^2}{2f_2^2}-\frac{\hat{y}^2}{2f_2^2}\right)\right) \\
& \exp\left(-i\frac{2\pi z_2}{\lambda}\left(-\frac{f_1^2}{f_2^2}+\frac{\hat{x}^2}{2f_2^2}+\frac{\hat{x}_s^2}{2f_2^2}+\frac{\hat{x}\hat{x}_s}{2f_2^2}+\frac{\hat{y}^2}{2f_2^2}+\frac{\hat{y}_s^2}{2f_2^2}+\frac{\hat{y}\hat{y}_s}{2f_2^2}+1-\frac{\hat{x}^2}{2f_2^2}-\frac{\hat{y}^2}{2f_2^2}\right)\right) \\
& \exp\left(i\frac{2\pi z_2}{\lambda}\left(1-\frac{f_1^2}{f_2^2}+\frac{\hat{x}_s^2+\hat{y}_s^2}{2f_2^2}\right)\right)\times\exp\left(i\frac{2\pi z_2}{\lambda f_2^2}(\hat{x}\hat{x}_s+\hat{y}\hat{y}_s)\right)
\end{aligned}$$

Now,

$$U_I(x, y) = F_{(f_2)}^{-1} \left[U_O\left(\frac{-(\hat{x}+\hat{x}_s)}{\lambda f_1}, \frac{-(\hat{y}+\hat{y}_s)}{\lambda f_1}\right) \times \exp\left(i\frac{2\pi z_2}{\lambda}\left(1-\frac{f_1^2}{f_2^2}+\frac{\hat{x}_s^2+\hat{y}_s^2}{2f_2^2}\right)\right) \right. \\
\left. \times \exp\left(i\frac{2\pi z_2}{\lambda f_2^2}(\hat{x}\hat{x}_s+\hat{y}\hat{y}_s)\right) \right] \quad (C.7)$$

$$f_1 = \frac{f_2}{m}$$

$$\begin{aligned}
U_I(x, y) = & \exp\left(i\frac{2\pi z_2}{\lambda}\left(1-\frac{f_1^2}{f_2^2}+\frac{\hat{x}_s^2+\hat{y}_s^2}{2f_2^2}\right)\right) \\
& \times F_{(f_2)}^{-1} \left[U_O\left(\frac{-(\hat{x}+\hat{x}_s)}{\lambda f_1}, \frac{-(\hat{y}+\hat{y}_s)}{\lambda f_1}\right) \times \exp\left(i\frac{2\pi z_2}{\lambda f_2^2}(\hat{x}\hat{x}_s+\hat{y}\hat{y}_s)\right) \right]
\end{aligned}$$

$$U_I(x, y) \propto \iint U_o \left(\frac{-m(\hat{x} + \hat{x}_s)}{\lambda f_2}, \frac{-m(\hat{y} + \hat{y}_s)}{\lambda f_2} \right) \times \exp \left(i \frac{2\pi}{\lambda f_2} \left(\left(\frac{\hat{x}_s z_2}{f_2} \right) \hat{x} + \left(\frac{\hat{y}_s z_2}{f_2} \right) \hat{y} \right) \right) \\ \times \exp \left(i \frac{2\pi}{\lambda f_2} (x\hat{x} + y\hat{y}) \right) d\hat{x}d\hat{y}$$

$$U_I(x, y) \propto \iint U_o \left(\frac{-(\hat{x} + \hat{x}_s)}{\lambda f_1}, \frac{-(\hat{y} + \hat{y}_s)}{\lambda f_1} \right) \\ \times \exp \left(i \frac{2\pi}{\lambda f_2} \left(\left(x + \frac{\hat{x}_s z_2}{f_2} \right) \hat{x} + \left(y + \frac{\hat{y}_s z_2}{f_2} \right) \hat{y} \right) \right) d\hat{x}d\hat{y}$$

$$\hat{x}' = \hat{x} + \hat{x}_s, d\hat{x}' = d\hat{x}, \hat{x} = \hat{x}' - \hat{x}_s$$

$$\hat{y}' = \hat{y} + \hat{y}_s, d\hat{y}' = d\hat{y}, \hat{y} = \hat{y}' - \hat{y}_s$$

$$U_I(x, y) \propto \iint \left[U_o \left(\frac{-\hat{x}'}{\lambda f_1}, \frac{-\hat{y}'}{\lambda f_1} \right) \right. \\ \left. \times \exp \left(i \frac{2\pi}{\lambda f_2} \left(\left(x + \frac{\hat{x}_s z_2}{f_2} \right) (\hat{x}' - \hat{x}_s) + \left(y + \frac{\hat{y}_s z_2}{f_2} \right) (\hat{y}' - \hat{y}_s) \right) \right) \right] d\hat{x}'d\hat{y}'$$

$$U_I(x, y) = \exp \left(i \frac{2\pi z_2}{\lambda} \left(1 - \frac{f_1^2}{f_2^2} + \frac{\hat{x}_s^2 + \hat{y}_s^2}{2f_2^2} \right) \right) \\ \times \exp \left(-i \frac{2\pi}{\lambda f_2} \left(\left(x + \frac{\hat{x}_s z_2}{f_2} \right) \hat{x}_s + \left(y + \frac{\hat{y}_s z_2}{f_2} \right) \hat{y}_s \right) \right) \\ \times \iint U_o \left(\frac{-\hat{x}'}{\lambda f_1}, \frac{-\hat{y}'}{\lambda f_1} \right) \times \exp \left(i \frac{2\pi}{\lambda f_1} \left(\frac{1}{m} \left(x + \frac{\hat{x}_s z_2}{f_2} \right) \hat{x}' + \frac{1}{m} \left(y + \frac{\hat{y}_s z_2}{f_2} \right) \hat{y}' \right) \right) d\hat{x}'d\hat{y}'$$

$$-\hat{x}' = \hat{x}''$$

$$-\hat{y}' = \hat{y}''$$

$$\begin{aligned}
U_I(x, y) = & -\exp\left(i \frac{2\pi z_2}{\lambda} \left(1 - \frac{f_1^2}{f_2^2} + \frac{\hat{x}_s^2 + \hat{y}_s^2}{2f_2^2}\right)\right) \\
& \times \exp\left(-i \frac{2\pi}{\lambda f_2} \left(\left(x + \frac{\hat{x}_s z_2}{f_2}\right) \hat{x}_s + \left(y + \frac{\hat{y}_s z_2}{f_2}\right) \hat{y}_s\right)\right) \\
& \times \iint U_O\left(\frac{\hat{x}''}{\lambda f_1}, \frac{\hat{y}''}{\lambda f_1}\right) \times \exp\left(-i \frac{2\pi}{\lambda f_1} \left(\frac{1}{m} \left(x + \frac{\hat{x}_s z_2}{f_2}\right) \hat{x}'' + \frac{1}{m} \left(y + \frac{\hat{y}_s z_2}{f_2}\right) \hat{y}''\right)\right) d\hat{x}'' d\hat{y}'' \\
\\
U_I(x, y) = & -\exp\left(i \frac{2\pi z_2}{\lambda} \left(1 - \frac{f_1^2}{f_2^2} + \frac{\hat{x}_s^2 + \hat{y}_s^2}{2f_2^2}\right)\right) \\
& \times \exp\left(-i \frac{2\pi}{\lambda f_2} (x\hat{x}_s + y\hat{y}_s)\right) \\
& \times u_O\left(\frac{-1}{m} \left(x + \frac{\hat{x}_s z_2}{f_2}\right), \frac{-1}{m} \left(y + \frac{\hat{y}_s z_2}{f_2}\right)\right)
\end{aligned} \tag{C.8}$$

The field at plane-I given in Eqn. C.8 can be divided into three parts. The first shows a constant phase depending on the focal lengths of lenses L1 and L2. Second part shows the presence of a linear phase. Part three shows the complex field of wavefront at plane O which is inverted, scaled by factor of $m = f_2/f_1$ and shifted by $\hat{x}_{s,n} z_2/f_2$ along x-direction and by $\hat{y}_{s,n} z_2/f_2$ along y-direction. The complex field of shearing wavefront is independent of wavelength.

Appendix D

Derivation of copies generated by grating

Derivation for shearing wavefront copies generated by grating based wavefront sensor is wavelength dependent.

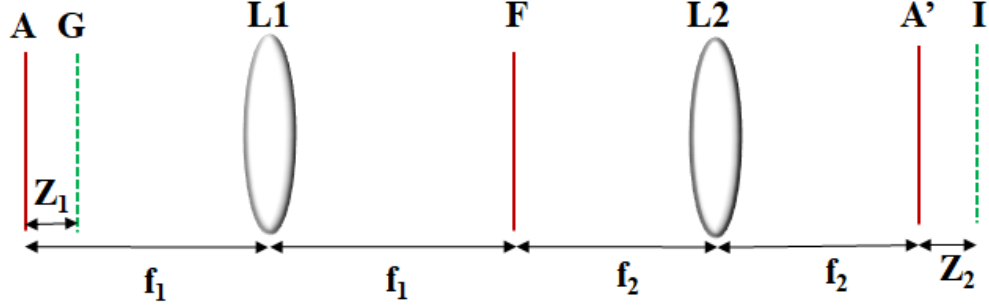


Figure D.1 Conceptual diagram for Grating based wavefront sensor

Let $u_O(x, y)$ be the object field at plane G (object plane) which has to be sheared at image plane I.

Field at plane A can be expressed as:

$$u_A(x, y) = F_1^{-1} \left[F_1(u_G(x, y)) \times \exp \left(i \frac{2\pi}{\lambda} z_1 \sqrt{1 - (\lambda f_x)^2 - (\lambda f_y)^2} \right) \right] \times \exp(i 2\pi (f_0 x + f_0 y)) \quad (\text{D.1})$$

Now, field at Fourier plane F will be

$$\begin{aligned} U_F(f_{x1}, f_{y1}) &= F_1 \{ u_A(x, y) \} \\ &= U_0(f_{x1} - 2f_{0x}, f_{y1} - 2f_{0y}) \\ &\quad \times \exp \left(i \frac{2\pi}{\lambda} z_1 \sqrt{1 - (f_{x1} - 2f_{0x})^2 - (f_{y1} - 2f_{0y})^2} \right) \end{aligned} \quad (\text{D.2})$$

{Because $F\left\{\exp\left[i\pi\left(ax+by\right)\right]\right\}=\frac{1}{|ab|}\delta\left(f_x-\frac{a}{2},f_y-\frac{b}{2}\right)$ and

$$F\left(f_x\right)\otimes\delta\left(f_x-f_0\right)=F\left(f_x-f_0\right)\}$$

Field at plane A' will be

$$u_{A'}(x,y)=F_2\left\{U_F\left(f_{x1},f_{y1}\right)\right\} \quad (D.3)$$

Field at plane I will be

$$U_I(x,y)=F_2^{-1}\left\{F_2\left[F_2\left(U_F\left(f_{x1},f_{y1}\right)\right)\right]\times\exp\left(-i\frac{2\pi}{\lambda}z_2\sqrt{1-\left(\lambda f_{x2}\right)^2-\left(\lambda f_{y2}\right)^2}\right)\right\}$$

$$U_I(x,y)=F_2^{-1}\left\{U_F\left(f_{x1},f_{y1}\right)\times\exp\left(-i\frac{2\pi}{\lambda}z_2\sqrt{1-\left(\lambda f_{x2}\right)^2-\left(\lambda f_{y2}\right)^2}\right)\right\} \quad (D.4)$$

$$=F_2^{-1}\left[\begin{array}{l} U_G\left(f_{x1}-2f_{x0},f_{y1}-2f_{y0}\right) \\ \times\exp\left(-i\frac{2\pi}{\lambda}z_1\sqrt{1-\left(\lambda\left(f_{x1}-2f_{x0}\right)\right)^2-\left(\lambda\left(f_{y1}-2f_{y0}\right)\right)^2}\right) \\ \times\exp\left(-i\frac{2\pi}{\lambda}z_2\sqrt{1-\left(\lambda f_{x2}\right)^2-\left(\lambda f_{y2}\right)^2}\right) \end{array}\right] \quad (D.5)$$

$$\text{Now, } f_{x1}=\frac{\hat{x}}{\lambda f_1}, f_{y1}=\frac{\hat{y}}{\lambda f_1}, f_{x1}=mf_{x2}, f_{y1}=mf_{y2}, m^2=\frac{z_2}{z_1}, m=\frac{f_2}{f_1}, z_1=z_2\left(\frac{f_1}{f_2}\right)^2$$

Substituting z_1f_{x1} and f_{y1} in Eqn. (D.5)

$$= F_2^{-1} \left[\begin{aligned} & U_G \left(mf_{x_2} - 2f_{x_0}, mf_{y_2} - 2f_{y_0} \right) \\ & \times \exp \left(-i \frac{2\pi}{\lambda} \frac{z_2}{m^2} \sqrt{1 - \left(\lambda \left(mf_{x_2} - 2f_{0x} \right) \right)^2 - \left(\lambda \left(mf_{y_2} - 2f_{0y} \right) \right)^2} \right) \\ & \times \exp \left(-i \frac{2\pi}{\lambda} z_2 \sqrt{1 - \left(\lambda f_{x_2} \right)^2 - \left(\lambda f_{y_2} \right)^2} \right) \end{aligned} \right] \quad (\text{D.6})$$

Expanding exponential terms using binomial theorem

$$\begin{aligned} & \exp \left(-i \frac{2\pi}{\lambda} \frac{z_2}{m^2} \left(1 - \left(\frac{\lambda^2 m^2}{2} \left(f_{x_2} - \frac{2f_{0x}}{m} \right) \right)^2 - \left(\frac{\lambda^2 m^2}{2} \left(f_{y_2} - \frac{2f_{0y}}{m} \right) \right)^2 \right) \right) \\ & \times \exp \left(-i \frac{2\pi}{\lambda} z_2 \left(1 - \frac{(\lambda f_{x_2})^2}{2} - \frac{(\lambda f_{y_2})^2}{2} \right) \right) \end{aligned}$$

After simplifying above term and substituting in Eqn. D.6

$$\begin{aligned} U_I(x, y) &= F_2^{-1} \left[\begin{aligned} & U_O \left\{ m \left(f_{x_2} - \frac{2f_{0x}}{m}, f_{y_2} - \frac{2f_{0y}}{m} \right) \right\} \times \exp \left(i \frac{2\pi}{\lambda} z_2 \frac{\lambda^2}{m} (f_{x_2} f_{0x} + f_{y_2} f_{0y}) \right) \\ & \times \exp \left(-i \frac{2\pi}{\lambda} z_2 \left(1 - \frac{1}{m^2} + \frac{1}{2} \left(\frac{\lambda}{m} \right)^2 (f_{0x}^2 + f_{0y}^2) \right) \right) \end{aligned} \right] \\ U_I(x, y) &= \exp \left(-i \frac{2\pi}{\lambda} z_2 \left(1 - \frac{1}{m^2} + \frac{1}{2} \left(\frac{\lambda}{m} \right)^2 (f_{0x}^2 + f_{0y}^2) \right) \right) \times \\ & F_2^{-1} \left[U_O \left\{ m \left(f_{x_2} - \frac{2f_{0x}}{m}, f_{y_2} - \frac{2f_{0y}}{m} \right) \right\} \times \exp \left(i \frac{2\pi}{\lambda} z_2 \frac{\lambda^2}{m} (f_{x_2} f_{0x} + f_{y_2} f_{0y}) \right) \right] \end{aligned}$$

$$\begin{aligned}
U_I(x, y) = & \exp \left(-i \frac{2\pi}{\lambda} z_2 \left(1 - \frac{1}{m^2} + 2 \left(\frac{\lambda}{m} \right)^2 (f_{0x}^2 + f_{0y}^2) \right) \right) \\
& \times \frac{1}{m} u_O \left\{ \left(x - \left(\frac{2z_2 \lambda f_{0x}}{m} \right), y - \left(\frac{2z_2 \lambda f_{0y}}{m} \right) \right) \right\} \\
& \times \exp \left(i \frac{2\pi}{m} (f_{0x} x + f_{0y} y) \right)
\end{aligned}
\tag{D.7}$$

The field at shearing plane-I given in Eqn. D.7 can be divided into three parts. The first shows a constant phase and third part shows the presence of a linear phase. Part second shows the complex field of wavefront at plane O which is inverted, scaled by factor of $m = f_2/f_1$ and shifted by $2z_2\lambda f_{0x}/m$ along x-direction and by $2z_2\lambda f_{0y}/m$ along y-direction. The complex field of shearing wavefront is dependent on wavelength.

List of Publications

Journal:

- Pramod Panchal, Dinesh N Naik, and C. S. Narayanamurthy, "Vectorial shearing cascaded Sagnac interferometric wavefront sensor," OSA Continuum 2, 2658-2666 (2019).
- Pramod Panchal, Dinesh N Naik and C S Narayanamurthy, "Wavefront sensing for low-coherent sources through spatial coherence revival", IOP-Eng. Res. Express 1 025011 (2019).
- Pramod Panchal, Dinesh N Naik and C S Narayanamurthy, "Insensitivity of higher order topologically charged Laguerre Gaussian beams to dynamic turbulence impact", Optics Comm. 495 127023 (2021).

Papers communicated/To be communicated

- Wave propagation analysis of laser Gaussian and Laguerre Gaussian beams through dynamic atmospheric turbulence mimicking pseudo random phase plate (PRPP) (Communicated to JI. Opt. Soc. Am A)
- Atmospheric turbulent impacted wavefront sensing using cascaded vectorial shearing interferometer (To be communicated to Applied Optics)

Conference:

- C. Jose, P. Panchal, and C. S. Narayanamurthy, "Wavefront analysis of Aberrated Laguerre-Gaussian Beam using Shack-Hartmann Wavefront Sensor," in Frontiers in Optics 2017, OSA Technical Digest (online) (Optical Society of America, 2017), paper JTU2A.43.
- P. Panchal, D. N. Naik, and C. S. Narayanamurthy, "Single shot vectorial shearing interferometry technique for wavefront reconstruction and aberration calculation," in Frontiers in Optics / Laser Science, OSA Technical Digest (Optical Society of America, 2018), paper JTU2A.21.

- P. Panchal, Rekshma. J, R. Sharma, and C. S. Narayanamurthy, "Wave propagation analysis of Laguerre–Gaussian beam through Pseudo Random Phase Plate (PRPP)," in *Frontiers in Optics + Laser Science APS/DLS*, The Optical Society (Optical Society of America, 2019), paper JW4A.62.